THE UNIVERSITY OF CHICAGO

MULTI-MODAL IMAGING OF TUMOR HYPOXIA TO IMPROVE RADIATION THERAPY

A DISSERTATION SUBMITTED TO
THE FACULTY OF THE DIVISION OF THE BIOLOGICAL SCIENCES
AND THE PRITZKER SCHOOL OF MEDICINE
IN CANDIDACY FOR THE DEGREE OF
DOCTOR OF PHILOSOPHY

COMMITTEE ON MEDICAL PHYSICS

BY
INNA HAVA GERTSENSHTEYN

CHICAGO, ILLINOIS
AUGUST 2022

TABLE OF CONTENTS

LIST OF FIGURES

LIST OF TABLES

ACKNOWLEDGMENTS

There is a long list of people who played important roles in the completion of this dissertation, both in my professional and personal life. I would first like to thank my co-advisors Howard Halpern and Chin-Tu Chen for their guidance in the past five years. I feel very fortunate to have had the experience of working with such inspiring scientists, who always found time be great mentors. I would also like to thank my committee members Maryellen Giger and Brian Roman for their valuable feedback and suggestions during our meetings.

I would especially like to thank everyone involved in the planning and execution of these complex imaging experiments. Starting with EPROI, Boris Epel developed the ArbuzGUI software at the Halpern Lab that I used extensively, as well as ran the EPR portion of all our imaging experiments. Subraman Sundramoorthy also played a large role in developing the EPR imagers we used in this work as well as portable anesthesia machines with Boris to help our experiments run more smoothly. Eugene Barth, John Lukens, Kayla Hall, Jenipher Flores Martinez, and Mellissa Grana were always helpful and flexible in running and troubleshooting experiment protocols and growing the tumor cells. Mihai Giurcanu used his biostatistics expertise to help write R code for the statistical analysis in Chapter 3.

PET imaging would not have been possible without the cyclotron team: Richard Freifelder, Anna Kucharski, and Mohammed Bhuiyan. I'd like to thank Aaron Tsai for always prepping the FMISO dose on time, as well as running the early imaging experiments with Lara Leoni (who also helped coordinate early experiments), Hannah Zhang, Andrew McVea, Nathanial Holderman, and Sam Mitchell. A special thanks to Heejong Kim for running his custom-built PET machine. Chien-Min Kao was also integral to my learning about PET imaging and kinetic modeling; he is the PI (with Boris Epel) on the project that led to the development of the hybrid PET/EPR imager that was so important to the success of this work.

For MRI, Erica Markiewicz, Marta Zamora, and Xiaobing Fan collected and processed all the T2-weighted and DCE MRI data, and over the years Brian Roman has worked on

perfecting the CEST MRI protocol that will be used in the near future. Chats with Greg Karczmar solidified my understanding of DCE MRI.

Marta Zamora and Hannah Zhang taught me about prepping a tumor sample for histology. Terri Li and Can Gong helped me develop the right methodology for IHC staining, and Christine Labno and Shirley Bond digitized the slides. Dr. Nicole Cipriani took time out of her busy schedule as a pathologist to validate (and just as often invalidate) our findings from H&E and IHC staining.

I'd also like to thank the undergraduate and high school students who I mentored over the past few years who made some contributions while learning about medical imaging and coding: Amandeep Ahluwalia, Meghan Xiang, Chloe Burns-Krul, and Ethan Richardson.

Clearly a huge number of people were involved in these imaging studies, though I must also thank all the mice that sacrificed their lives for us to learn about a horrific disease and how to better image and treat it.

I would like to thank Elena Rizzo, Julie Hlavaty, Ruth Magaña, Hoang Ngo, Maya Suraj, and Lili González for their administrative assistance and refreshing chats, and Fauzia Arif for helping me get my F31 through the complex NIH system. I would also like to thank all the professors in the GPMP who gave me such a strong foundation in medical physics and imaging, and to Tim Carroll, Sam Armato, and Hania Al-Hallaq for mentoring me during first year research rotations.

My classmates Brittany Broder, Jordan Furhman, and Isabelle Qu were always wonderful. I would like to especially thank the three of them as well as all other current and former members of the GPMP. I will always look back fondly on the lunch/coffee breaks, walks to the duck pond, journal clubs, and complaining sessions we all shared. I would *NOT* like to thank the ankle I fractured and dislocated in 2019, or the pandemic, but I know that those events would have been much worse experiences without the collective friendship and support of my fellow students.

Of course I must mention the lasting friendships I've made with Scott Trinkle, Talon Chandler, and Andrew McVea, who by now have already moved on to the next chapter of their careers. We are all still part of Quarantine Movie Club, which started at the beginning of the pandemic in 2020. We just watched our hundredth movie.

However, the biggest thanks goes to Zion Rodman, my partner since 2015. Zion is always a loving comfort after a long day. When I walk up the stairs to our apartment and hear his music, and open the door to see our cats Obie and Poosh, I know that the rest of the day will be filled with warmth and positivity. I could not have completed this PhD in one piece without his presence, and him moving to Chicago with me has meant the world.

Finally, I want to thank my parents Bella and Michael, and my sister Rachel, for always supporting me and offering refuge at home. Along with my grandparents, aunts, uncles, and cousins, my whole family has always encouraged me to pursue a life in science. This work would not have been possible without their upbringing.

This work was supported by funds from the National Institutes of Health under grants R01CA098575, R01CA 236385, P30CA014599, P41EB002034, S10OD025265, R01EB029948, R44CA224840, T32EB002103, and F31CA254223.

ABSTRACT

Hypoxic tumors are associated with poor patient prognosis because hypoxia leads to angiogenesis, metastasis, and resistance to chemotherapy and radiation therapy. This dissertation explores imaging modalities to accurately measure and locate tumor hypoxia to improve radiation therapy.

We used three tumor murine models of squamous cell carcinomas (SCC7), mammary adenocarcinomas (MCa-4), and fibrosarcomas (FSa) for electron paramagnetic resonance oxygen imaging (EPROI), ^{18}F-Fluoromisonidazole positron emission tomography (FMISO PET), dynamic contrast-enhanced magnetic resonance imaging (DCE MRI), and histological imaging.

The theme of this dissertation is using EPROI as an *in vivo* validation of absolute pO_2, which is traditionally an invasive and discretely measured task. For now, EPROI is generally a preclinical imaging tool that is rarely available in the clinic. However, we can compare measurements from EPROI to the more clinically available modalities, like FMISO PET and DCE MRI, to develop tools to improve their accuracy. This was accomplished in four parts.

First, we used EPROI to demonstrate the effectiveness of delivering a radiation boost to more resistant hypoxic tumor regions, while minimizing radiation dose to oxygenated tumor regions and surrounding healthy tissue. Local tumor control probability improved by at least a factor of two when comparing hypoxic versus oxygenated boost treatment groups. These experiments in oxygen-guided radiation therapy show immense promise in minimizing dose while improving radiation therapy outcomes.

While EPROI has a clear threshold to define *in vivo* hypoxia ($pO_2 \leq 10$ mmHg), there is presently no unifying threshold to define hypoxia with FMISO PET. Here we identified optimal FMISO uptake thresholds to define hypoxia with a custom-built hybrid PET/EPR machine for near-simultaneous hypoxia imaging, using EPROI as ground truth to define tumor hypoxia. The optimal thresholds varied by tumor type, and on average had a 68-73%

similarity between hypoxic volumes defined by FMISO PET and EPROI.

DCE MRI identified features of tumor vasculature and extracellular-extravascular space that may pinpoint where and why FMISO PET was not as accurate as EPROI in locating tumor hypoxia. EPROI determined where FMISO PET correctly classified or misclassified voxels as normoxic or hypoxic. Additionally, histological images of axial tumor slices stained with H&E validated tumor boundaries and necrosis, and IHC stains of the hypoxia inducible factor 1α (HIF-1α) and vasculature with CD31 were compared to registered *in vivo* slices.

Tying all *in vivo* imaging modalities together, different methods of modeling and correcting FMISO PET with pO_2 and DCE MRI were evaluated. A newly developed logistic model was implemented in a correction algorithm that combines FMISO PET with optimally-weighted DCE MRI parametric images to improve the accuracy of hypoxia location. This work sets up future experiments that may use corrected FMISO PET images to locate tumor hypoxia for oxygen image-guided radiation therapy originally done with EPROI.

The presented research is a step toward improving radiation therapy methods and outcomes for patients with hypoxic tumors. Throughout, we demonstrate tumor-type dependence of the accuracy of FMISO PET and highlight the effectiveness of oxygen-guided radiation therapy in improving local tumor control.

CHAPTER 1

INTRODUCTION

Hypoxia is an inadequate supply of oxygen, which causes resistance to chemo- and radiation therapy in solid tumors and lead to angiogenesis, metastasis, and aggressiveness of the cancer [1]. Therefore, hypoxic tumors are generally associated with poor patient prognosis [2]. The prognostic value of tumor hypoxia has been demonstrated in cervical cancers [3–7], head and neck cancers [8, 9], lung cancers [10, 11] and soft tissue sarcomas [12, 13]. Because hypoxic status is independent of a tumor's histology, size, grade, or stage, functional imaging is necessary to quantify and locate the extent of hypoxia. The ability to accurately measure and locate tumor hypoxia with non-invasive imaging — the topic of this dissertation — has the potential to improve radiation therapy. Yet even though the topic of low oxygenation and radiation sensitivity has been identified since the early 1900s [14–16], and the 2019 Nobel Prize in Physiology or Medicine was awarded to three hypoxia researchers, there is still no widely accepted method that is clinically available for accurate *in vivo* hypoxia imaging.

Accurately locating tumor hypoxia would provide the opportunity to deliver a radiation boost to more resistant hypoxic tumor regions, while minimizing radiation dose to oxygenated tumor regions and surrounding healthy tissues that are more sensitive to radiation [17, 18]. Recent clinical trials observed no difference in toxicities between patients who received a boost dose to hypoxic tumor subregions identified by high FMISO uptake and patients who received standard radiation therapy [10, 19]. This indicates that such boosts may be safely administered if organs at risk are identified and their maximum radiation dose tolerances are observed. Therefore, dose escalation to hypoxic subregions has the potential to reduce harmful side effects to the patient by lowering the overall dose deposited (e.g. by delivering a low dose to the whole tumor and a high dose to a subset of the tumor instead of the high dose to the whole tumor, shown in Figure 1.1).

Correctly identifying thresholds of hypoxia with different imaging modalities, tracers, and

tumor models remains a challenge today. This work is an exploration of imaging and treating tumor hypoxia in several preclinical models and modalities to work towards improved oxygen image-guided radiation therapy.

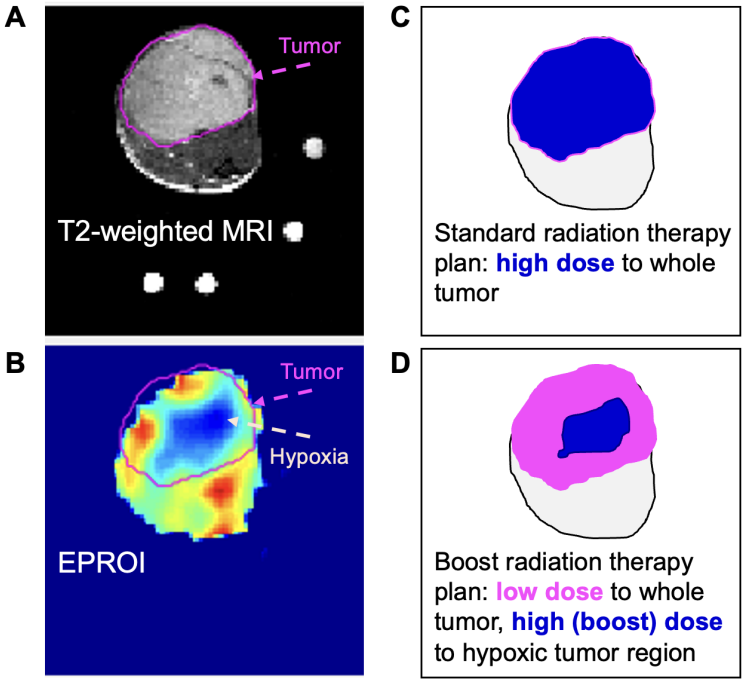

Figure 1.1: (A) T2-weighted MRI axial slice of a tumor, and (B) the same slice of pO_2 EPROI, with the tumor contoured in magenta. (C) Example of standard radiation, delivering a high dose to the whole tumor, and (D) boost radiation therapy guided by oxygen images, with a low dose delivered to oxygenated tumor regions and a high dose to hypoxic tumor regions.

1.1 Overview of Oxygen Imaging and Hypoxia Thresholds

The enormous complexity of living systems can confound measurements of oxygen since they depend on the intrinsic accuracy (i.e. oxygen resolution) of the measurements, the volume to which individual measurements are sensitive (spatial resolution), and the sources of confounding physiological variation that affect the measurement of the molecular oxygen concentrations. Imaging molecular oxygen content further complicates the process.

The partial pressure of oxygen (pO_2) is an absolute measurement, with some uncertainty,

of oxygen *in vivo*. As oxygen moves from the blood plasma (a source) to the mitochondria (a sink) by diffusion, a gradient is formed, with pressure lower at the sink than at the source [20]. The difference in pO_2, and therefore the gradient, increases with the rate of oxygen consumption within a cell. While *in vitro* cellular measurements describe the 50% onset of radiation resistance to radiation at ∼2.5 Torr (= mmHg), *in vivo* tissue and tumor measurements have clustered about 10 mmHg [21, 22]. *In vivo*, malignant well-oxygenated cells have pO_2 values between 10 and 60 mmHg.

As the field progresses from *in vitro* cell studies to preclinical *in vivo* experiments across animal models and modalities before applying novel imaging and treatment techniques in humans, it is important not to assign a universal threshold of hypoxia to any tissues, cells, microvessels, etc. Relevant thresholds and their onsets vary depending on the physiological process being studied and how those measurements are taken. For example, *in vivo* experiments of tissue determine that critical pO_2 is between 8 and 10 mmHg, while in vitro experiments on cytochromes determine 0.02–0.07 mmHg as the critical threshold. We must keep these differences in mind as we progress towards applying our newfound knowledge to the clinic to improve patient care and outcome.

1.2 Dissertation Objectives

This dissertation focuses on two modalities for directly and indirectly imaging oxygen: electron paramagnetic resonance oxygen imaging (EPROI) and ^{18}F-Fluoromisonidazole positron emission tomography (FMISO PET). While EPROI is a faster and more accurate method of imaging absolute pO_2, where hypoxia is defined by $pO_2 \leq 10$ mmHg, it is not yet widely available in the clinic. FMISO PET is clinically available, and the most affordable and commonly used hypoxia radiotracer to date [23], though with limited accuracy.

Additional imaging in this work includes T2-weighted magnetic resonance imaging (MRI) to delineate malignant tumor from healthy tissue, and dynamic contrast-enhanced (DCE)

MRI to model parametric images of K^{trans} (vascular perfusion and permeability) and v_e (the fractional extracellular-extravascular space) throughout the tumor. Supplementary histological imaging with hematoxylin and eosin (H&E) and immunohistochemical (IHC) staining was done to investigate the tumor microenvironment on a microscopic scale.

Though the presented research uses preclinical tumor models, the end goal is to show the effectiveness of dose escalation to hypoxic tumor regions. This has been achieved in three mouse tumor models with four specific objectives:

1. Demonstrate improved local tumor control using oxygen image-guided radiation therapy with EPROI.

2. Identify the optimal threshold to define hypoxia with FMISO PET, using EPROI to establish ground truth.

3. Compare relationships between tumor vasculature and hypoxia across tumor types with DCE MRI, FMISO PET/EPROI, and IHC staining.

4. Model and correct FMISO PET with EPROI and DCE MRI to improve the accuracy of locating tumor hypoxia.

The novelty of this dissertation is in the use of EPROI as an *in vivo* validation of true hypoxia. Traditionally, validating hypoxia is done invasively with Eppendorf needles or *ex vivo* with pimonidazole, which introduces several confounding factors. Because different tumor types also play a potential confounding role, three syngeneic tumor models are evaluated: SCC7 squamous cell carcinomas, MCa-4 mammary adenocarcinomas, and FSa fibrosarcomas.

1.3 Dissertation Organization

Chapter 2 gives a technical overview of the modalities used in this dissertation: EPROI, FMISO PET, DCE MRI, and histological imaging. While this chapter offers a brief intro-

duction of each modality, the curious reader is encouraged to read the curated references for further details.

Chapter 3 gives an overview of oxygen image-guided radiation therapy with EPROI in three tumor types and two EPR imagers. These experiments were carried out between 2015-2022, and demonstrate the benefit of directing a radiation boost to hypoxic tumor regions. Using Kaplan-Meier survival analysis, we show increased local control for tumors in the Hypoxic Boost treatment group compared to the Oxygenated Boost treatment group. We also identified tumor properties for which a Hypoxic Boost treatment may not be appropriate.

Chapter 4 addresses inconsistencies in the literature in defining tumor hypoxia with FMISO PET among research groups, which may affect dose planning and treatment outcome. A custom-built hybrid PET/EPR machine was used to image and calculate the optimal FMISO thresholds to define hypoxia for each tumor type, using EPROI to define the ground truth of hypoxia. These thresholds serve as the basis to define hypoxia using FMISO PET throughout the dissertation.

Chapter 5 quantifies the relationships between tumor vascular properties modeled with parametric images from DCE MRI with hypoxia images from EPROI and FMISO PET. *In vivo* images were validated by histological imaging, using H&E staining to identify necrotic regions, and IHC staining for hypoxia inducible factor 1α (HIF-1α) expression, and cluster of differentiation 31 (CD31), which stains endothelial cells of blood vessels.

Chapter 6 compares two models to model FMISO with pO_2, and describes the development of a correction algorithm that combines FMISO PET and DCE MRI to make FMISO-defined hypoxia images more accurate in locating tumor hypoxia, again using EPROI to define the ground truth of hypoxia. Ideally, this model can potentially be utilized in the clinic with PET/MR imaging to improve patient prognosis.

To close, Chapter 7 offers a summary of the dissertation and concluding remarks, and suggestions on future work that can strengthen our understanding of tumor hypoxia imaging.

CHAPTER 2

OVERVIEW OF IMAGING MODALITIES

Here we describe the basic principles of EPROI and PET, a more clinically-relevant imaging modality with hypoxia radiotracers. The fundamentals of other imaging modalities utilized in this dissertation, including T2-weighted and DCE MRI and histological staining, will also be discussed in this chapter.

2.1 Electron Paramagnetic Resonance Oxygen Imaging

Previous hypoxia measurement techniques include the use of an Eppendorf electrode to measure partial pressure of oxygen, pO_2 [24]. Studies using the Eppendorf probe to provide dozens of samples from several human cancers determined that the hypoxia and low pO_2 can be used as a predictor of the success or failure of radiation treatment [3, 25, 26]. However, the Eppendorf probe is an invasive method of blindly measuring pO_2. EPROI is a relatively new imaging modality that accurately measures pO_2, and has shown promising results for oxygen image-guided radiation therapy in preclinical studies.

The relationships between energy, the magnetic moment, and the magnetic field are similar in EPR and nuclear magnetic resonance (NMR) in their dependence on the particle mass. Because the mass of an electron is approximately three orders of magnitude smaller than the mass of a proton, the magnetic field strength of an EPR imager is reduced to 9–40 mTesla, rather than the 1.5–9.4 Tesla field strength used in MRI. Therefore, EPR imagers are significantly lighter, more affordable to build and maintain, and have no possibility for harmful or even fatal accidents compared to MRI [27]. Nevertheless, EPROI is accompanied by T2-weighted MRI, which provides high resolution anatomical contrast to define the boundaries of tumours, or other structures of interest, registered with EPROI.

In MRI, the main magnetic field aligns the abundant water hydrogen nuclear spins in

one direction as a net magnetization. Without this main magnetic field, the proton spins are randomly oriented. A second magnetic field disturbs the proton spins by a pulse of electromagnetic energy, which induces transitions between energy levels. Because the lower energy level is more populated, there is a net absorption of energy creating a population excitation [28]. A pulse response imager measures the time it takes for those disturbed spins to relax to their undisturbed orientations (also called the relaxation rate) over microsecond time intervals with 10's of kilohertz repetitions [29]. The excitations take place in a series of magnetic field gradients, which causes the absorption to occur at different, identifiable locations and transforms that information into an image [30, 31].

Unlike MRI, EPR imaging measures *unpaired electron spins* of dissolved and diffusible molecules [32]. These are scarce in biological systems since free metals like iron and copper catalyse chemical reactions. These transition metal unpaired electron spins are bound in carrying proteins or enzymes, and are not measurable at low EPR frequencies at biologically relevant temperatures [33]. The exception is molecular oxygen (O_2), which is free to diffuse in living tissues. O_2 bears two unpaired, rapidly relaxing electrons. The relaxation is too fast to directly measure; therefore, an oxygen spin probe must be introduced into the system in question [32, 34].

Each spin probe (e.g. OX063-d24 in Figure 2.1A) contains a relatively stable unpaired electron that interacts with the two unpaired electrons of oxygen molecules [36]. The EPR imager can detect the relaxation rates of the spin probes, and how their relaxation rates change in the presence or absence of oxygen [37, 38]. There is a linear relationship between the relaxation rate of the spin probe and pO_2, where surrounding low pO_2 corresponds to a low relaxation rate, and high pO_2 corresponds to a high relaxation rate (Figure 2.1B). The spin-lattice relaxation rate is independent of spin probe concentration. Therefore, regardless of how well or poorly perfused a tumor region is — which may affect spin probe concentration — the relaxation rate would not confound measurements by interacting with itself [33].

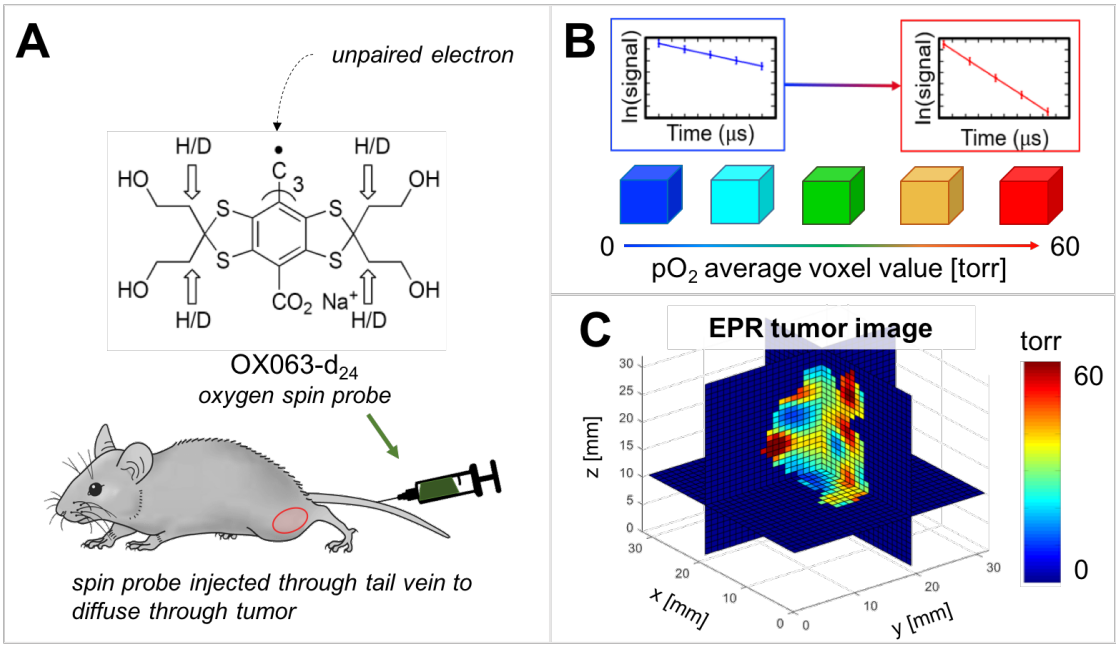

Figure 2.1: (A) Chemical structure of oxygen spin probe OX063-d24, which is infused into the mouse via tail vein. (B) The relaxation rate of the spin probe is higher for high pO_2 and lower for low pO_2. (C) Tomographic reconstruction shows a 3D quantitative distribution of pO_2 in the tumor, where pO_2 voxels $\leq$ 10 torr (=mmHg) show hypoxia (blue). This figure originally appeared in Gertsenshteyn *et al.* [35]

.

Overall, the signal-to-noise ratio (SNR) of the system varies with the number of spins in that voxel, and higher SNR leads to a higher spatial resolution of the image. Currently, the range of spatial resolution in EPR is 1–5mm with the higher resolution at lower pO_2.

In a 250-MHz (a low frequency) pulse EPR imager, a trityl spin probe (OX063-d24) as shown in Figure 2.1A is useful for oxygen imaging *in vivo* because of its strong signal and low toxicity [39, 40]. Once injected into the mouse tail vein, the probes diffuse in the extracellular fluid compartment of the tumour, where the clearance half-life is 20–30 min, while the clearance half-life in the blood stream is 2–5 min [41] due to enhanced permeability and retention [42]. The original *in vivo* pulse EPR pO_2 imaging technique is due to the group of Murali Krisha at the National Cancer Institute [43].

Multiple projections of the spin probes' relaxation rates are acquired in the EPR imager

to generate a three-dimensional image (Figure 2.1C), where each voxel corresponds to an average pO_2 value. The heterogeneity of hypoxia within the tumour shows the importance of imaging the entire volume, rather than just one- or two-dimensional measurements [44]. Fiducial-based registration of the EPR image to an anatomical CT or MR images is necessary to define anatomical boundaries.

In general, EPR imaging has the advantage of a high quantitative accuracy, with uncertainty less than 1 Torr in the range of 1–10 Torr [37, 39]. This makes EPROI ideal in differentiating hypoxic vs. well-oxygenated regions. EPR imagers also have different penetration depth abilities depending on their frequency, which ranges from 0.2 to 1 GHz. Imaging at a lower frequency, such as 250 MHz, has an 8 cm penetration depth [45], which is advantageous to quantitative imaging of larger animals [41, 46]. High frequency EPR oximetry at 1.2 GHz has a penetration depth at 5–10mm, which is limited to small animal imaging or peripheral anatomy. The tradeoff, however, is that the sensitivity of an EPR instrument increases with increasing frequency (ν) as $\nu^{0.8}$ [46, 47], so the SNR is sacrificed for a higher penetration depth.

2.2 Positron Emission Tomography and ^{18}F-Fluoromisonidazole

Positron emission tomography (PET) is used for functional imaging. The most common PET radiotracer is ^{18}F-Fluorodeoxyglucose (FDG), which binds to cells with metabolic activity and is used for diagnosing, staging, and treating cancer, among other diseases. PET imaging utilizes a positron-emitting radionuclide as a tracer with an intravenous or intraperitoneal injection.

As the PET radioisotope decays, it emits a positron, which travels some millimeters (depending on the radioisotope) through tissue. Once the positron loses enough energy to local ionizations, it undergoes mutual annihilation with an electron, which leads to a pair of 511 keV photons emitted 180° from each other [48]. The coincidence photons are

detected within a specified energy range and timing window. However, in addition to true coincidence events, there can be scatter and random coincidence events that can result in incorrect positional information and contribute to a loss of contrast [48]. Figure 2.2 shows an example of each event.

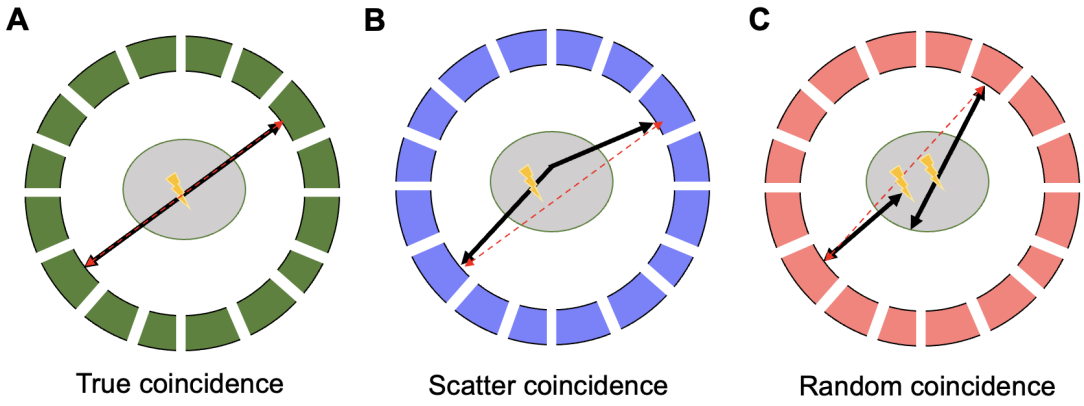

Figure 2.2: Example of a PET scanner with a gray phantom in the center, and the origin of a (A) true coincidence event, (B) scatter coincidence event, and (C) random coincidence event.

Image resolution is fundamentally limited by different factors, primarily the detector crystal size and the positron range of the random path it travels before annihilation [49]. The smaller the individual detectors, which typically comprise of a scintillator coupled to a photodetector, the better the intrinsic resolution of the PET scanner. However, the monetary cost increases with the number of detectors arranged into a ring around the subject, and the number of rings. Due to the small size of preclinical scanners, PET image resolution can be on the order of 1-2 mm. Typical clinical scanners generally have resolution of about 4-5 mm, which is suboptimal for detecting small tumors. The main advantage to using ^{18}F as the radiolabel is that it has the lowest positron range (mean range = 0.6 mm) compared to other radiotracers (mean ranges for ^{11}C, ^{13}N, ^{15}O, ^{68}Ga are 1.1, 1.5, 2.5, and 2.9 mm, respectively) [50].

Several radiotracers are available to image with PET to assess hypoxia, though the most widely used radiotracers for clinical cancer studies is FMISO, a nitroimidazole compound

radiolabeled with ^{18}F. The ^{18}F radionuclide has a 110-minute half-life, and the misonidazole biological half-life is 50 minutes [51]. Misonidazole can be reduced to a radical anion by cellular electron donors and enzymes in either oxygenated or hypoxic cells [52]. In the absence of oxygen, once the nitroimidazole enters a hypoxic cell the radical anion can undergo further reduction and local molecular binding. This binds the nitroimidazole inside the cell. In the presence of oxygen, the reduced nitro group can be oxidized back into the original substance by O_2 and diffuse away [53]. There is also evidence that increased production and decreased excretion of the glutathione conjugate of reduced FMISO contributes to FMISO accumulation in tumor cells under hypoxic conditions [54].

Within 2–4 hours, FMISO accumulates in hypoxic cells and the radionuclide can be detected by PET imaging systems. However, there is still ongoing work to identify the dependence on tumor type, which may be a confounding variable [55, 56]. There is also minimal research on the utility of FMISO PET imaging in pediatric patients, who would significantly benefit from dose painting and sparing nearby organs at risk. There is also controversy between whether the pharmacokinetics and distribution of FMISO are affected by the immature and disorganized tumour microvasculature, which could also prevent the tracer from reaching hypoxic regions far from capillaries.

2.3 Dynamic Contrast Enhanced Magnetic Resonance Imaging

DCE MRI is generally used for non-invasive characterization of tumor vasculature structure and function, treatment response, and more recently for drug development [57]. In the absence of clinically-available high-resolution *in vivo* modalities to image hypoxia, several studies have attempted to use DCE MRI as a surrogate to characterize tumor hypoxia [58, 59]. However, using DCE MRI to assess hypoxia has had variable results, likely contributed by the cyclical nature of acute hypoxia and the positive feedback loop of hypoxia-induced angiogenesis.

A T1-weighted sequence is used for DCE MRI to model K^{trans} and v_e, which are derived from the Tofts model [60]. The transfer constant K^{trans} characterizes the diffusive transport of low-molecular weight contrast agent (CA) chelates across the capillary endothelium [60] and is related to capillary permeability, surface area, and perfusion. The CA is some form of gadolinium, in this case gadodiamide (Omniscan, GE Healthcare). The fractional volume v_e of the extravascular extracellular space (EES) is also measured [61]. In animal studies, high v_e can indicate necrosis [58]. Dividing K^{trans} by v_e results in k_{ep}, the rate constant for the reflux of the CA from the EES back into the vascular system.

In the 9.4 Tesla small animal imager, these images have submillimeter resolution. 128 frames of T1-weighted images are acquired every 5 seconds before and after a bolus injection of the CA. The spin-lattice relaxation time is reduced by the presence of the CA, which creates a contrast between voxels over time. Over each voxel, these intensity curves are fit for each voxel to calculate K^{trans} and v_e.

Figure 2.3 shows an example of central axial slices of all three tumor types in all modalities: T2-weighted (T2W) MRI, FMISO PET, EPROI, K^{trans}, and v_e. In the MCa-4 tumor (left), the white arrow points to a necrotic region where EPROI shows hypoxia with low pO_2, but no FMISO uptake. The DCE MRI regions that overlap with FMISO PET are low K^{trans} and high v_e. However, the area that EPROI confirms is hypoxic has a very high k_{ep} ($k_{ep} = K^{trans}/\ v_e$). The FSa tumor (center) is well perfused with low FMISO uptake and high pO_2 2. The SCC7 tumor (right) again shows a white arrow pointing to a region of mismatched hypoxia identification in FMISO and PET, though without any apparent necrosis shown in T2W MRI. This shows the inconsistencies across tumor types in features of FMISO PET/EPR/MRI.

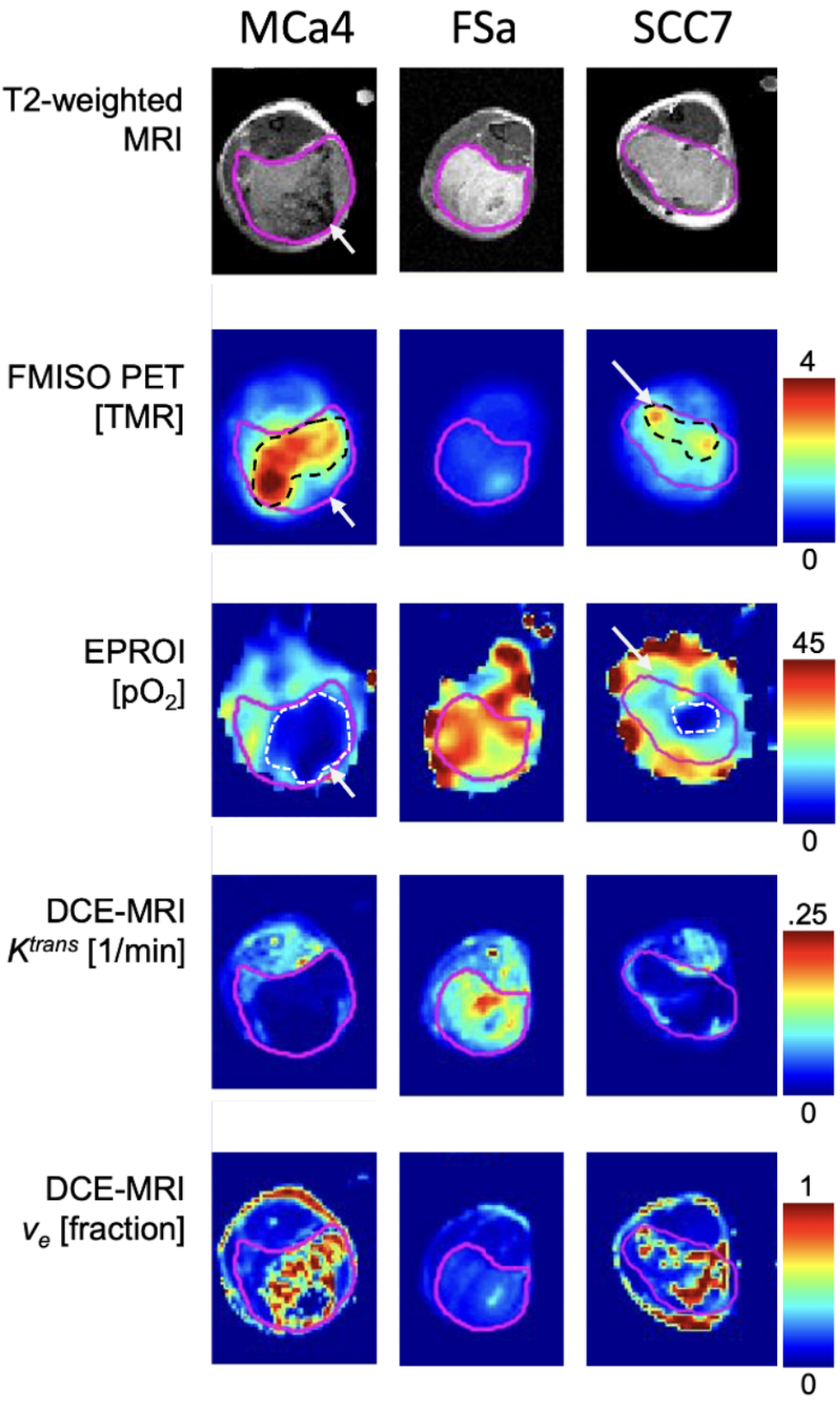

Figure 2.3: Central axial slices of tumors for three murine tumor models (columns) with all *in vivo* image modalities. White arrows point to regions where hypoxia location does not match between FMISO uptake and low pO_2 from EPROI.

2.4 Histological Imaging

Hematoxylin and Eosin (H&E) staining has been used by pathologists for over a century. Hematoxylin stains cell nuclei blue, and Eosin stains the extracellular matrix, cytoplasm and other structures varying shades of pink. Under a microscope, H&E stains can give a clear picture of lesion boundaries and disease types.

For example, Figure 2.4 shows H&E stains of three tumor types studied in this dissertation. The FSa fibrosarcomas murine model has a heterogenous tumor cell density and many instances of necrosis. MCa-4 mammary adenocarcinomas consisted of large stromal and vascular structures throughout the tumors. SCC7 squamous cell carcinomas had densely packed tumor cells and microvasculature. These features would be invisible with *in vivo* imaging due to resolution limitations, but are important in interpreting potential causes of success or failure of certain regimens.

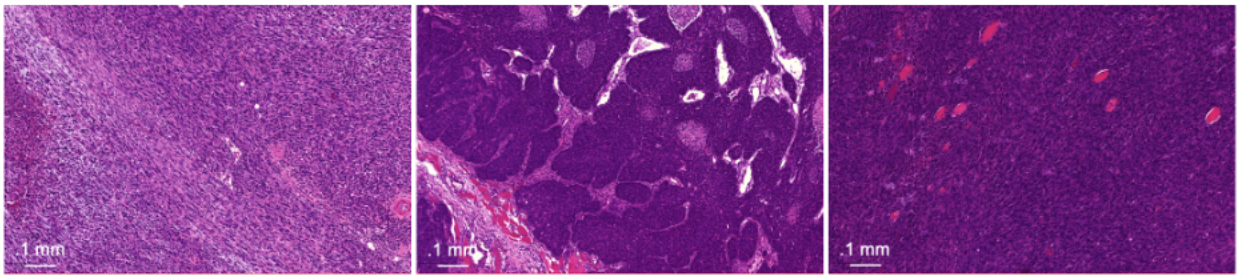

Figure 2.4: H&E stains of tumors used in these studies: from left-to-right, FSa fibrosarcomas, MCa-4 mammary adenocarcinomas, and SCC7 squamous cell carcinomas.

IHC involves the process of selecting antibodies that bind specifically to antigens, or proteins. To reduce nonspecific binding and maximize signal-to-noise ratio, antibodies should be derived from a different animal model than the one being studied. In this work, two immunostains are used to supplement H&E. Cluster of differentiation 31 (CD31) demonstrates the presence of endothelial cells. The degree of tumor angiogenesis, the chaotic formation of new blood vessels, can be determined with CD31. Hypoxia inducible factors (specifically HIF-1α) are activated by hypoxia, which promote tumor regrowth. It would be expected

that around hypoxic subregions and the edges of a growing tumor would express HIF-1α. Figure 2.5 shows examples of these IHC stains across tumor types, where dark brown shows the staining over blue cells.

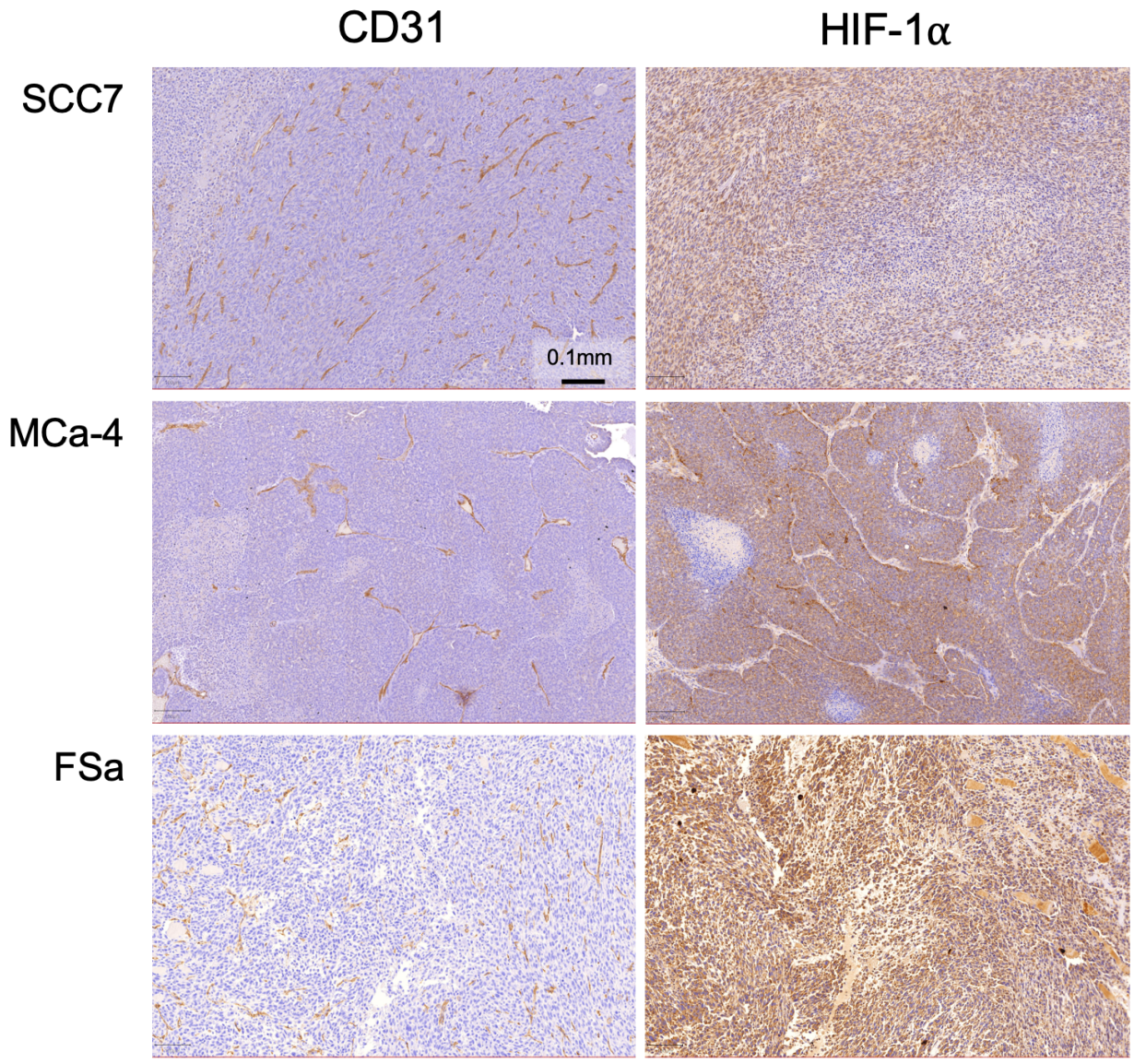

Figure 2.5: IHC stains of CD31 and HIF-1α for SCC7, MCa-4, and FSa tumor mouse models.

CHAPTER 3

OXYGEN IMAGE-GUIDED RADIATION THERAPY WITH EPROI: IMPROVING LOCO-REGIONAL CONTROL IN MURINE TUMOR MODELS

3.1 Introduction

In the infancy of understanding the effects of radiation, Schwarz observed that reduced blood flow protected living tissue (his own skin) from toxicity [16]. By the time Crabtree and Cramer [15] observed variations in sensitivity in tumor cells and Thomlinson and Gray [14] identified hypoxic rims in bronchogenic human carcinomas as the source of radiation resistance in cancer treatments, hypoxic resistance to radiation had been identified in virtually all living tissue. The factor of three oxygen enhancement ratio for X-ray radiation in cellular systems led to an enormous effort to exploit the hypoxic compartment with British Hyperbaric Oxygen Trials [62] and the development of hypoxic sensitizers [63]. Despite indications of enhanced efficacy [64], difficulties in radiation delivery with hyperbaric oxygen and the toxicity of sensitizers has diminished enthusiasm for application. A new wave of experiments in delivering oxygen-loaded microbubbles to improve radiosensitivity are promising, though presently results show delayed tumor growth rather than cure [65, 66].

A challenge in the field has been accurately imaging tumor hypoxia to improve treatment planning. EPROI is an imaging modality that accurately measures the partial pressure of oxygen (pO_2) and has shown promising results to optimize preclinical oxygen image-guided radiation therapy. The assumption that all solid tumors have clinically relevant hypoxia may not be correct [67–69]. Therefore, it is imperative to study tumor oxygen physiology across several tumor types, as well as the response of hypoxic tumors to various radiation therapy regimens.

A previously published study by Epel *et al.* [39] was the first mammalian demonstration

that selective hypoxia targeting significantly improves loco-regional tumor control. Mice were randomly assigned to a Hypoxic Boost versus a control Oxygenated Boost treatment in FSa fibrosarcoma murine tumor models. A 20% tumor control dose (TCD20%) was delivered to the whole tumor, followed by a 13 Gy boost dose at TCD95% to either hypoxic or oxygenated regions within the tumor. The study showed a significantly higher local tumor control probability (p=0.04) for tumors treated with a Hypoxic Boost (60% probability) vs Oxygenated Boost (29% probability) 90 days after treatment.

The present work repeated this study in oxygen image-guided radiation therapy with MCa-4 mammary adenocarcinomas, and SCC7 squamous cell carcinomas. Further insight is provided into the oxygen physiology across tumor types through subgroup analysis of the randomized experiments. The promising results of this work that has spanned almost a decade is the foundation and motivation for the rest of the dissertation.

3.2 Methods

3.2.1 EPR Imagers

Two EPR imagers were used for oxygen image-guided radiation therapy. The lower-frequency EPR system (LF-EPR) operates at 250-MHz (∼9mT) and allows for a higher penetration depth accessible to human imaging. The JIVA-25^{TM} (O2M Technologies, Chicago, IL) operates at 720 MHz (∼25mT), and generates images at higher SNR while using a lower volume of the costly oxygen-sensitive spin probe, at the expense of penetration depth but suitable for lesions close to the surface of the skin. The oxygen spatial resolution is ∼1.4 mmHg with the LF-EPR, and ∼1 mmHg with the JIVA-25^{TM}.

3.2.2 Tissues and cell cultures

Syngeneic FSa fibrosarcoma, MCa-4 mammary adenocarcinoma, and SCC7 squamous cell carcinoma tumor cells were obtained from the M.D. Anderson Cancer Center. The harvested cells were suspended in 0.1-4.0x10^6 cells in modified Eagle medium with 10% fetal bovine serum and injected in the gastrocnemius muscle of the left leg of the mice. Tumors were used for imaging and treatment once grown to a radiobiological relevant volume between 225–450 mm^3, as defined by T2-weighted MRI.

3.2.3 Animal model, anesthesia, and euthanasia

Animal experiments followed U.S. Public Health Service policy, NIH Guide for the Care and Use of Laboratory Animals, and were approved by the Institutional Animal Care and Use Committee. Mice were observed frequently, and were euthanized and removed from the study if they exhibited signs of infection or injury to minimize pain and suffering. Table 3.1 summarizes the number of tumors that were imaged and treated for tumor hypoxia.

At the time of imaging and treatment assignment, the mice were ∼12 weeks old. Tumor volumes were within radiobiological range at 350 ± 60 mm^3. Anesthesia was induced using 2% isoflurane mixed with air (21.5% oxygen and 78.5% nitrogen) and maintained with 1.5% isoflurane and air, administered with a mask. Respiration rate was maintained at approximately 1.5Hz, which was used to guide anesthesia depth, and core temperature was kept at 37°C. Following the completion of experiments, euthanasia was performed with isoflurane overdose or CO_2 asphyxiation, confirmed by cervical dislocation.

3.2.4 Imaging

The mouse was anesthetized to prepare for imaging, and its leg-bearing tumor was immobilized in a soft rubber half-circumferential vinyl polysiloxane dental mold cast (GC America) designed to fit into a 3D printed plastic support bed. This ensured the leg would be con-

Table 3.1: Summary of EPR imagers, radiation doses, and number of animals used for each group.

	FSa	MCa-4	SCC7	SCC7
EPR operating frequency	250-MHz	250-MHz	250-MHz	720-MHz
Whole tumor dose	22.5 Gy	49.9 Gy	48 Gy	48 Gy
Boost dose	35.5 Gy	62.9 Gy	61 Gy	61 Gy
N Hypoxic Boost	21	26	24	18
N Oxygenated Boost	16	22	21	22
N Total	38	48	45	40

sistently immobilized between imaging modalities: MRI, EPROI, and CT. Figure 3.1 shows an example of one tumor's images in all three modalities, registered to the same space.

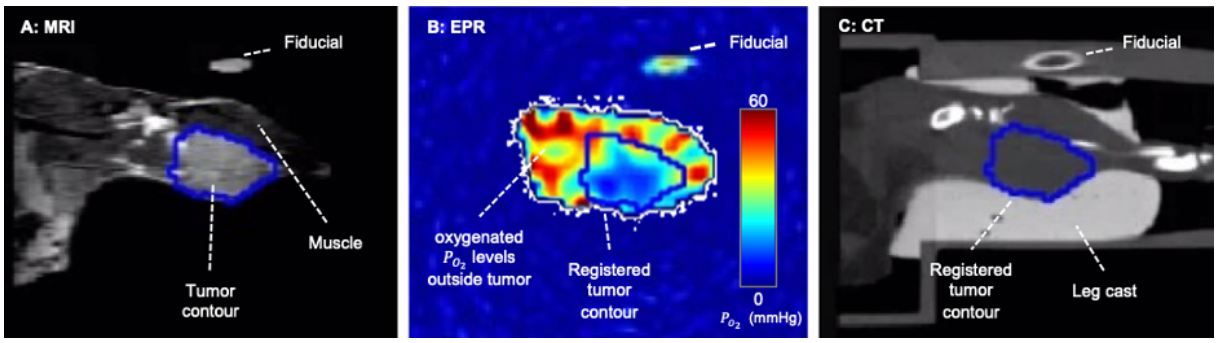

Figure 3.1: Example tumor coronal slice in three modalities: (A) T2-weighted MRI, (B) EPROI, and (C) CT. A registration fiducial filled with water and oxygen spin probe appears in all three modalities.

T2-weighted MRI provided images of tumor contrast used in localized targeting for curative radiation therapy, which were acquired using a 9.4 Tesla small animal scanner (Bruker, Billerica, MA, USA) using a multislice RARE sequence. Reconstructed images had 0.1x0.1x0.75 mm^3 voxel resolution. If the tumor was determined suitable for treatment (with a localized tumor volume between 225-425 mm^3), the mouse was recovered from anesthesia to await tail-vein cannulation for further imaging and treatment. Mice tolerated the cast well while awake.

The pO_2 image from EPROI was used to locate the hypoxic regions within the tumor, de-

fined by $pO_2 \leq 10$ mmHg. EPR pO_2 images were acquired with pulse spin-lattice relaxation oxygen imaging using a low-frequency 250-MHz pulse EPR imager and the higher-frequency 720-MHz pulse EPR imager (JIVA-25^{TM}). 135 μl of an 80mM OX63-d24 (also named OX071) oxygen measuring spin probe (0.43 mmols/Kg) was used for EPROI [70].

An image of the fiducials was first acquired for registration purposes. The OX071 probe was injected as an intravenous bolus followed by 3.5 μl/min continuous infusion. Three EPR images of tumor pO_2 were acquired while the oxygen spin probe was infusing throughout the body into the tumor. The first image confirmed the presence of the spin probe, and the second and third images confirmed its stability of the central location of hypoxia. Each pO_2 image acquisition took 11 minutes with the 250-MHz EPROI system (total 33 minutes), and 5 minutes with the JIVA-25^{TM} system (total 15 minutes). The second pO_2 image with isotropic 0.67mm voxel resolution was used to assess the location of all hypoxic voxels (pO_2 ≤ 10 mmHg) and the tumor hypoxic fraction (HF10), defined in Equation 3.1.

$$HF10 = \frac{N_{voxels} \leq 10}{N_{voxels}} \tag{3.1}$$

The HF10 between 0.02 and 0.42 defined suitability for treatment, to be able to reasonably treat hypoxic or oxygenated tumor regions with boosts of similar integral volume without boosting the entire tumor.

A computed tomography (CT) scan was obtained with an X-RAD 225Cx (Precision X-Ray, North Branford, CT, USA) which was also used to locate the radiation target volume and deliver both whole tumor and boost radiation dose registered with the T2 MRI and the EPR pO_2 image. Fiducials (filled with water and the oxygen spin probe) embedded in the imaging bed were used to register all three modalities to CT coordinate space for radiation treatment, and are visible throughout Figure 3.1.

3.2.5 Dose Plan

Prior to multi-modal imaging and treatment of hypoxic tumors, preliminary tumor control dose (TCD) studies were completed on FSa, MCa-4, and SCC7 tumors. Groups of 6-7 tumors were irradiated at different doses to calculate the fraction of tumors that recurred at each dose. Figure 3.2 shows TCD fitted curves for each tumor type. These curves were used to estimate the tumor control dose at 20% ($TCD_{20\%}$) for whole tumor doses, and 95% ($TCD_{95\%}$) for boost doses. The actual doses delivered are summarized in Table 3.1.

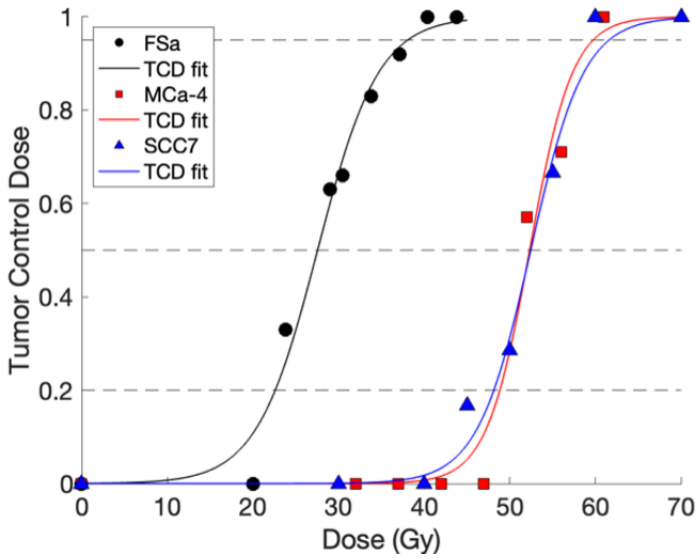

Figure 3.2: TCD curves for FSa (black), MCa-4 (red), and SCC7 (blue) tumor types.

The High-Risk planning target volume, or the hypoxic boost region (PTV_{HR}) was defined by the EPR pO_2 image within the MRI-based tumor contour, with a 1.2mm margin added to the hypoxic region (Figure 3.3A). The Low-Risk planning target volume, or the oxygenated boost region (PTV_{LR}) was planned similarly, with a 0.6mm margin around the hypoxic regions defining the inner edge of the boost region, and the outer edge was expanded to an approximately equal aperture area to that of the hypoxic boost (Figure 3.3B). A more detailed explanation of the selection of hypoxia-target regions, radiation block fabrication, and radiation boost region determination is in the supplementary materials of previously

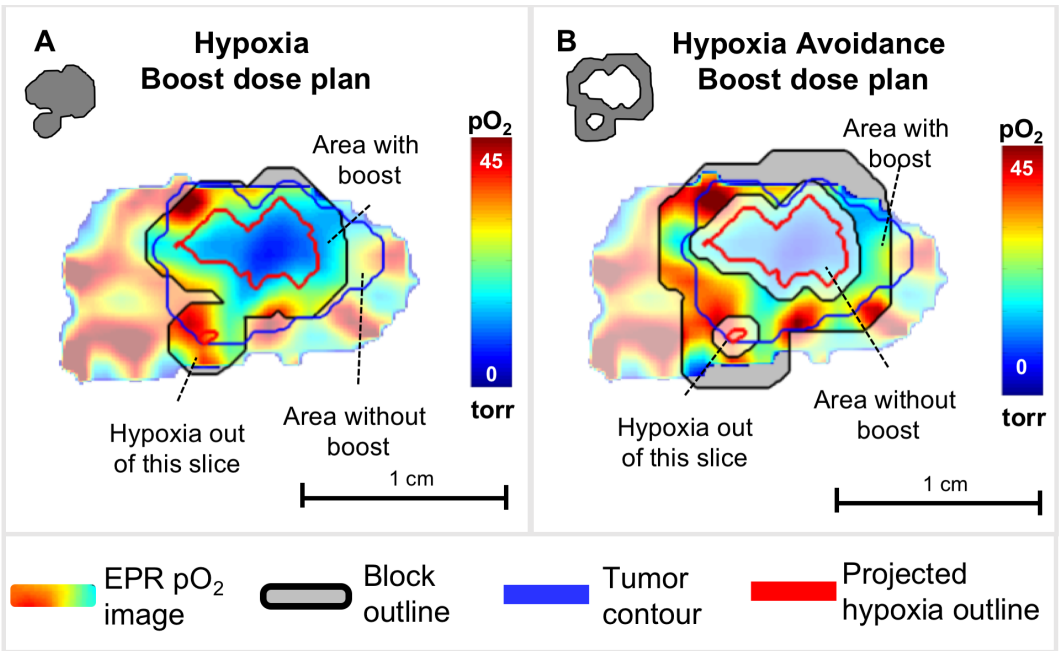

Figure 3.3: Radiation treatment plans of (A) Hypoxic Boost vs (B) Oxygenated Boost, or Hypoxia Avoidance Boost. The boost areas of both treatment plans are equal.

published work [39].

3.2.6 Statistical Analysis

Analysis of variance (ANOVA) was employed to compare group means between tumor types. SCC7 tumors were combined into one group, and analyzed separately by EPR-imager group (250-MHz vs 720-MHz). Two-sample t-tests were conducted to test for significant differences between means of risk factors of local recurrence between the two treatment (Hypoxic vs Oxygenated Boost) groups before radiotherapy. Local tumor control probability (LTCP) was assessed by recurrence free survival probability at the end of the study: 180 days for MCa-4 and SCC7 tumors and 90 days for FSa tumors. The progression free survival curves were compared between the Hypoxic Boost vs Oxygenated Boost treatments using Kaplan-Meier curves and the log-rank test.

Kaplan-Meier recurrence free survival curves were grouped by treatment, and stratified by critical biomarkers: low/high HF10, tumor volume, and experiment duration, all relative

to the median value of each tumor type.

Cox regression models were employed to estimate the hazard ratio (HR) of local recurrence boost treatments, adjusting for the potential confounding variables of HF10, experiment duration, and tumor volume. The HR shows whether the risk of tumor recurrence would decrease when treating with hypoxic boost compared to treating with oxygenated boost. HR ≥ 1 indicates that a hypoxic boost treatment would *not* be more beneficial than an oxygenated boost treatment. The proportional hazards assumption was verified using the global Schoenfeld test.

Data analysis was conducted using the statistical software R and the R package survival was used for Kaplan-Meier analysis and Cox regression models [71]. ANOVA was done in MATLAB (Mathworks, Natick, MA, USA). In comparing LTCP between tumor types, SCC7 tumors imaged in both the 250- and 720-MHz EPR imagers were grouped together. However, analysis was repeated with subgroups of SCC7 tumors imaged in the 250-MHz, and the 720-MHz imagers.

3.3 Results

With the 250-MHz EPR imager, a total of 78 mice were entered in the FSa group, 65 mice in the MCa-4 group, and 70 mice for the SCC7 group; with the 720-MHz EPR imager, 48 mice were entered for the SCC7 study. Following exclusion criteria, such as tumors out of range of pre-determined hypoxic fractions and tumor volumes, and experimental failures in the process of radiation, the following number of mice included in statistical analysis: 38 FSa, 48 MCa-4, 45 SCC7 (250-MHz), and 40 SCC7 (720-MHz) EPROI. The total of 171 tumors were included in the Kaplan-Meier and Cox regression analysis, including all animals that survived without local tumor recurrence for 90-180 days, local failures, and animals censored at the time of an event not related to local failure.

There was no linear correlation between tumor volume and HF10 (R^2=0.0), as evident in

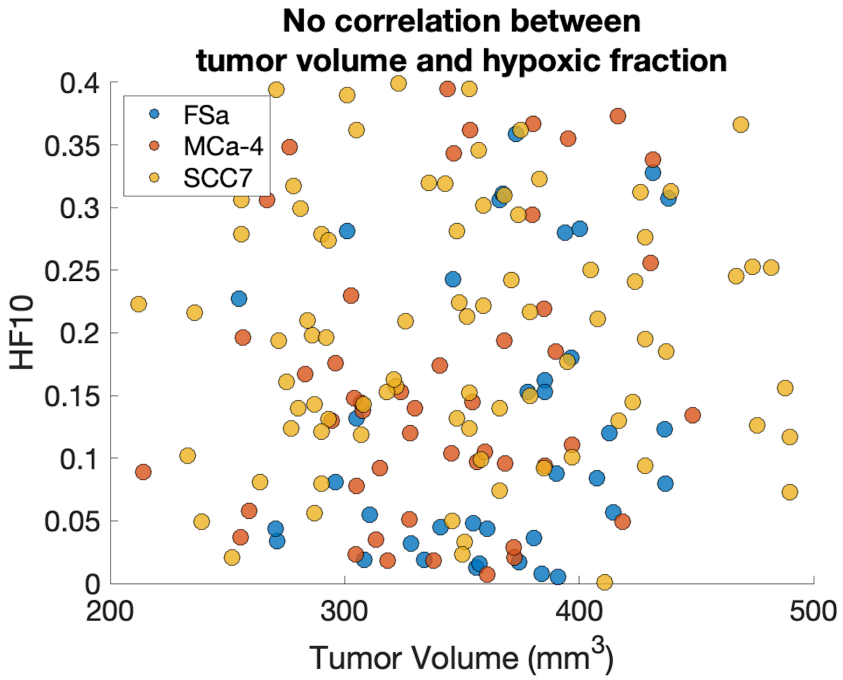

Figure 3.4: Scatter plot of all tumors' volumes vs. hypoxic fraction, showing no correlation between the two features.

Figure 3.4. Figure 3.5 shows the group mean and standard deviation of HF10, volume, and experiment duration for every tumor type. The mean HF10 for SCC7 (250-MHz EPROI) was 0.22, which was significantly higher ($p \leq 0.05$) compared to 0.13 for FSa, 0.16 for MCa-4, and 0.18 for SCC7 (720-MHz) groups. Group mean tumor volume was similar across tumor types and EPR imagers ranging from 340 to 363 mm^3. Group mean experiment duration for FSa tumors was 1.3 hours, significantly lower ($p<0.001$) compared to 3.5, 3.2, and 2.8 hours for MCa-4 and both SCC7 groups. HF10 affected LTCP with subgroup analysis, while tumor volume and experiment duration did not have a significant effect on LTCP.

Although mice were randomly assigned to boost treatment groups, there were potential confounding variables to consider. Within each group, the two-sample t-test showed no significant difference between tumor growth rate, HF10, or tumor volume between boost treatments. The MCa-4 group had a significantly higher ($p \leq 0.01$) experiment duration for the Oxygenated Boost treatment subgroup (3.9 hours) compared to the Hypoxic Boost

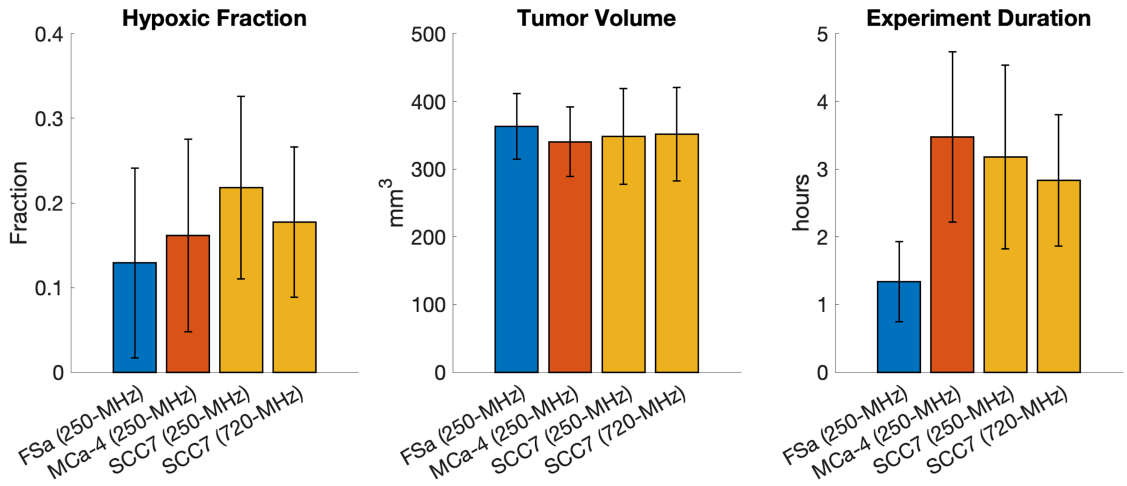

Figure 3.5: Mean and standard deviation of hypoxic fraction, tumor volume, and experiment duration for each tumor experiment group. Bars are color coded by tumor type.

treatment subgroup (3.0 hours), though this did not affect LTCP. There was no significant difference in experiment duration between treatment subgroups for FSa or SCC7 groups.

Figure 3.6 shows Kaplan-Meier plots comparing LTCP between hypoxic and oxygenated boost treatments. There was a significantly higher LTCP in all three tumor groups: FSa (p=0.049), MCa-4 (p=0.01), and SCC7 (p=0.016). However, when looking at SCC7 tumors subgrouped by the EPR imager, there was not a significant difference between hypoxic and oxygenated boost treatment groups for the 250-MHz imager group (p=0.35) and a significant difference between treatment groups for the 720-MHz imager group (p=0.007). SCC7 tumors from the 250-MHz EPROI group had the highest HF10 compared to all other groups, a confounding variable which may have consequences in treatment outcome explored further in the discussion section.

Figure 3.7 shows Kaplan-Meier curves stratified by low and high HF10, set by the median HF10 in each group. The effects of HF10 were dependent on tumor type and boost treatment. The stratified log-rank test failed to show a significant difference between boost treatments for FSa tumors (p=0.23). However, MCa-4 and SCC7 tumors still showed a significant improvement in LTCP for hypoxic boost vs oxygenated boost treatment when stratified by

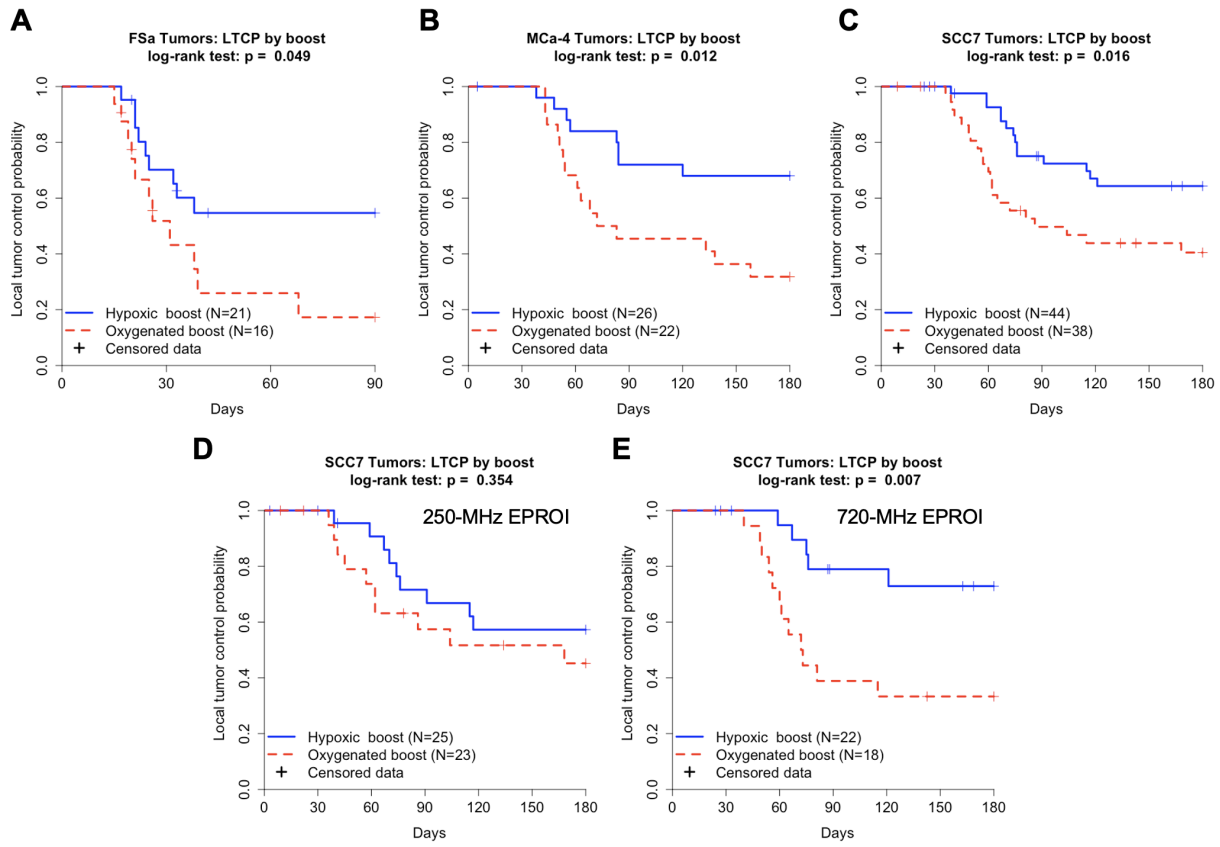

Figure 3.6: Kaplan-Meier log-rank test by Hypoxic (blue) vs Oxygenated (red) boost treatments for (A) FSa, (B) MCa-4, and (C) SCC7 tumors. Additionally, SCC7 tumors are subgrouped by EPR imagers operating at (D) 250-MHz and (E) 720-MHz.

HF10 (p=0.01 for MCa-4 and p=0.02 for SCC7). FSa and MCa-4 tumors with a high HF10 treated with a hypoxic boost had the highest LTCP, while SCC7 tumors with a low HF10 treated with a hypoxic boost had the highest LTCP.

Figure 3.8 shows Kaplan-Meier curves stratified by low and high tumor volume, set by the median tumor volume in each group. The stratified log-rank test showed a very strong trend between boost treatments for FSa (p=0.051), and a significant difference for MCa-4 and SCC7 (both p=0.01). Again, the effects of tumor volume were dependent on tumor type and boost treatment. With hypoxic boost treatment, FSa and MCa-4 tumors with a high tumor volume had the highest LTCP, while there was no significant difference between low/high tumor volume for SCC7 tumors.

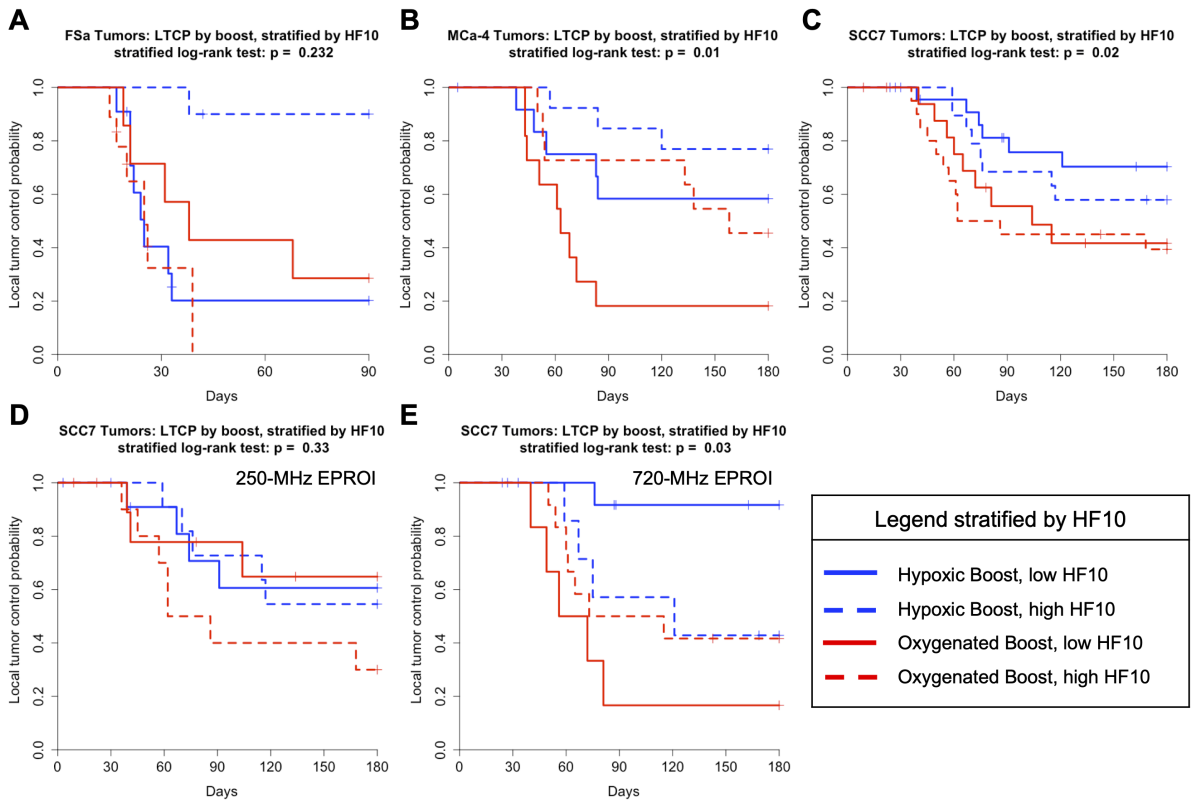

Figure 3.7: Kaplan-Meier curves stratified by low/high HF10 (measured in EPROI) for Hypoxic (blue) vs Oxygenated (red) boost treatments.

Figure 3.9 shows Kaplan-Meier curves stratified by low and high experiment duration, set by the median experiment duration in each group. The stratified log-rank test showed a very strong trend between boost treatments for FSa (p=0.052), and a significant difference for MCa-4 (p=0.03) and SCC7 (p=0.01). For all three tumor types treated with a hypoxic or oxygenated boost, there was a similar LTCP for short vs long experiment duration. An exception was for SCC7 tumors treated with oxygenated boost, which had a higher LTCP for short experiment duration.

Comparing SCC7 tumors subgrouped by EPR imager and stratified by HF10 (Figure 3.7D-E), tumor volume (Figure 3.8D-E), and experiment duration (Figure 3.9D-E), SCC7 tumors imaged with the 720-MHz EPROI consistently showed a significantly higher LTCP for hypoxic boost treatments ($p \leq 0.03$) than the 250-MHz EPROI ($p > 0.3$). Potential reasons

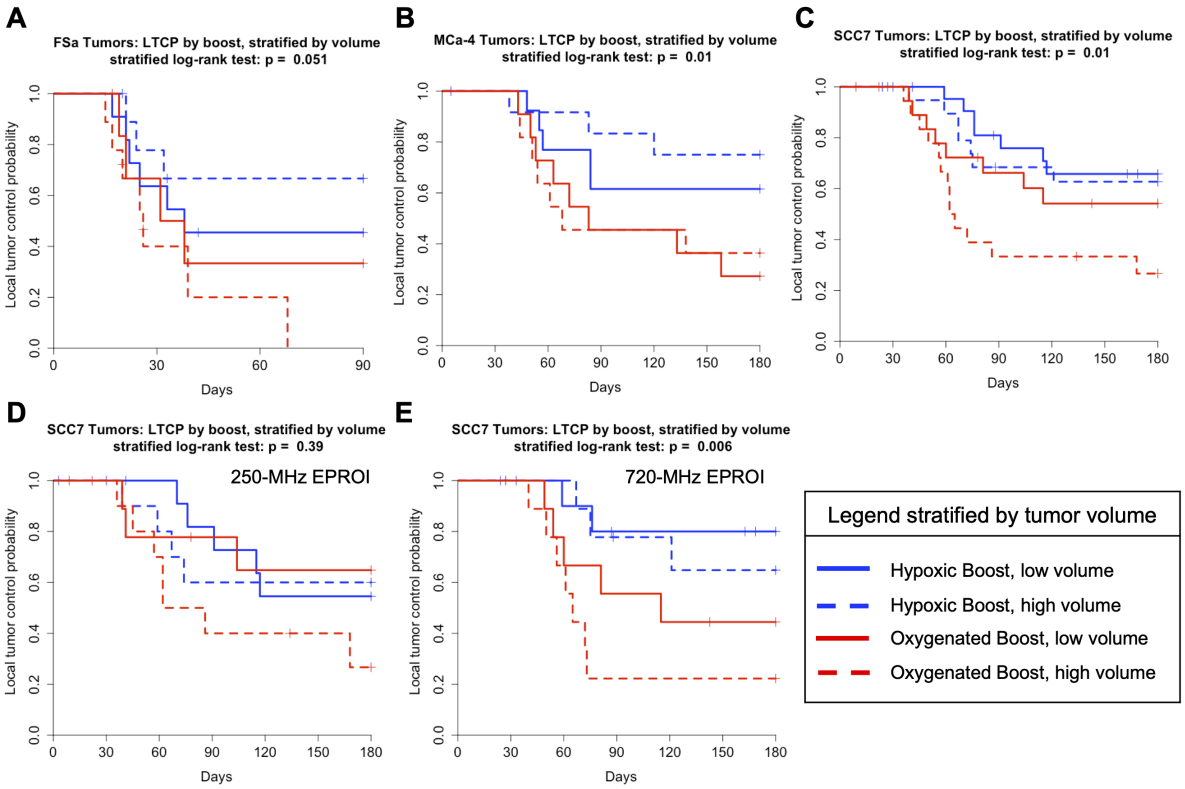

Figure 3.8: Kaplan-Meier curves stratified by low/high tumor volume (measured in T2-weighted MRI) for Hypoxic (blue) vs Oxygenated (red) boost treatments.

for these results are explored in the Discussion section.

Using Cox regression analysis, the time to tumor recurrence was controlled for the effects of HF10, tumor volume, and experiment duration. For all three tumor types, the HR was less than 0.5 (HR=0.24, p=0.03 for FSa tumors; HR=0.37, p=0.06 for MCa-4 tumors; HR=0.45, p=0.02 for SCC7 tumors). This shows that the hazard risk is lower with hypoxic boost compared to oxygenated boost treatment, even when controlling for confounding variables.

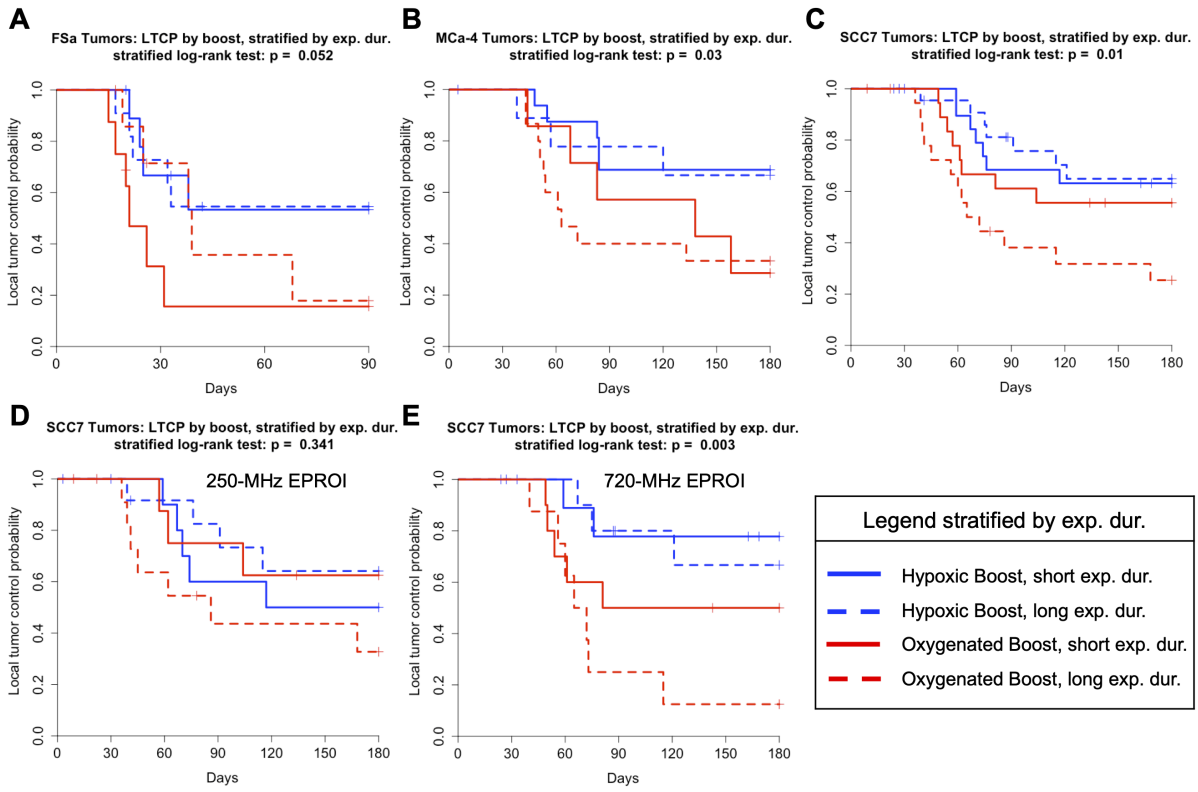

Figure 3.9: Kaplan-Meier curves stratified by short/long experiment duration (hours between EPROI and radiation therapy) for Hypoxic (blue) vs Oxygenated (red) boost treatments.

3.4 Discussion

This work presents data in three preclinical mammalian tumor types to demonstrate that targeting hypoxic tumor subregions with a boost of radiation improves LTCP relative to a boost of the same integral dose to oxygenated regions of the tumor. This is a confirmation of the first study of this kind on FSa tumor murine models [39] with two additional tumor types and statistical analysis exploring the effects of HF10, tumor volume, and experiment duration, and EPR imagers. The LTCP was improved by a factor of 3.2 for FSa, 2.1 for MCa-4, and 1.6 for all SCC7 tumors. Within each group between the two treatment plans, the distribution of HF10 and tumor volumes were comparable.

In all studies, tumors were treated with separate whole tumor doses with low probability of tumor control ($TCP_{15-20\%}$) and both randomized rough equivalent integral dose volume

boosts to either hypoxic or oxygenated tumor regions, in which over 98% of EPR pO_2 image voxels plus a margin in the PTV were targeted. In all experiments, the delivered boost dose was 13 Gy. A difference between studies was that the boost dose for SCC7 and FSa tumors was a $TCD_{95\%}$ which controlled 95% of tumors in a separate whole tumor treatment TCD study, while in the MCa-4 study, an additional 5Gy was added to the boosts to deliver a $TCD_{99\%}$ dose.

The SCC7 tumors were also separated into two groups with oxygen imaging acquired with the same low-frequency EPR machine (250-MHz) as the FSa and MCa-4 tumor groups with 48 animals, as well as a new higher-frequency imager (720-MHz) with 40 animals. Interestingly, only the SCC7 (720-MHz) group showed a significant improvement with hypoxic boost treatments. This may be due to the fact that the SCC7 (250-MHz) group had a significantly higher HF10 compared to other groups, with median HF10=0.22 compared to median HF10 ranging from 0.08 to 0.15 in other groups. This suggests a limitation in the presented method of delivering a boost dose to hypoxic tumor subregions if tumors are overly hypoxic.

Knowing that tumor hypoxia is worse for patient prognosis, an intuitive hypothesis would be that tumors with low HF10 would have high LTCP. However, we observe the opposite effect in FSa and MCa-4 tumors, where tumors with high HF10 have high LTCP. This implies a tumor type-dependent effect of HF10 on treatment outcome, where low HF10 increases tumor control probability for SCC7 squamous cell carcinomas, which is the expected result. Given that SCC7 squamous cell carcinomas are tumors in syngeneic mice with intact immune systems, as are all the tumors studied here, this may indicate that in this particular tumor type, high levels of hypoxia, well known to interfere with tumor immunogenicity [72], may require higher boost doses.

This may also be caused by the fact that a larger volume of the tumor would be boosted if it had a higher HF10. On the other hand, SCC7 tumors imaged with the 720-MHz imager with low HF10 had LTCP=0.92 at 180 days, while high HF10 had 0.43 at 180 days —

an improvement of 2.1 within a subgroup. Again, the reason for this may be the lower distribution of HF10 in these tumors. Another reason may be the higher oxygen resolution and shorter EPR imaging time in the JIVA5^{TM} led to more accurate hypoxia location for dose planning. At this time, it is not clear whether SCC7 tumors may need higher operating frequency EPR imagers with superior resolution than FSa and MCa-4 tumors, or that SCC7 tumors with an HF10 above some threshold would not benefit from a hypoxic boost treatment.

There was an effect on LTCP by high/low HF10 and tumor volume that differed across tumor types. However, experiment duration had virtually no effect on LTCP with hypoxic boost treatments across tumor types. This is an important observation for two reasons. One, experiment duration was the only potential confounding variable for MCa-4 tumors, where MCa-4 tumors treated with hypoxic boost had a significantly lower experiment duration than those treated with an oxygenated boost. Second, cyclical hypoxia has been cited as an issue for oxygen-image guided radiation therapy [73] because hypoxia distribution may change in a tumor between the time of imaging to the time of treatment. We show here that time does not affect treatment outcome even when the time between imaging and treatment ranges from 1 to 6 hours.

Experiment duration does have an effect on experimental failure, though, because the longer a mouse is under anesthesia the more likely it is to undergo respiratory failure before treatment is over. We also see that for SCC7 tumors, those treated with an oxygenated boost have a higher LTCP by a factor of 2.1 when experiment durations were short compared to long. Further work in Chapter 4 also demonstrates how hypoxia deepens and increases in volume over the course of 5 hours. It is possible that even if this happens in these experiments, the added 1.2mm boost margin accounts for that increasing hypoxic volume.

The design of the radiation treatments provided the cleanest separation between boosts to hypoxic and well oxygenated tumor, using opposed fields with margins to minimize in-

clusion of the voxels unwanted identity. This however left out voxels shadowed by those of unwanted identity and limited the extent of hypoxia allowable for randomization. The presented approach is more primitive relative to modern intensity modulated radiation treatments providing more subtle sculpting of dose distributions with capability to define 3D avoidance structures and more carefully defined "simultaneous integrated boosts". Work involving compensators to provide the doses sculpting is ongoing [74].

3.5 Conclusions

Maps of tumor pO_2 generally showed that hypoxia develops in subregions relatively deep within a tumor. This can be targeted with a boost dose which, in many clinical cases, can reduce dose to potential organs at risk that are related to quality of life, and still improve tumor control. This promises the enhancement of the therapeutic ratio. This present work confirms the relevance of EPROI in defining tumor hypoxia in three tumor types. Dose painting hypoxic tumor regions with a 13Gy boost in addition to a whole-field dose of $TCD_{20\%}$ enhances tumor control by around a factor of 2. Ongoing work involves more sophisticated dose planning for small animal IMRT to better emulate treatments more relevant to clinical treatment design [74].

Despite the promising results from oxygen image-guided radiation therapy using EPROI, the major limitation of the study is the lack of EPR imagers available in hospitals for human pO_2 imaging. For this reason, the rest of the dissertation aims to include more clinically available modalities – PET and MRI – to improve tumor hypoxia location for improved radiotherapy treatment plans and patient prognosis.

CHAPTER 4

OPTIMAL THRESHOLD TO DEFINE HYPOXIA WITH FMISO PET

4.1 Introduction

A simple imaging and analysis approach is required for hypoxia imaging to be widely implemented. While the overarching goal of this work is to use DCE MRI to improve the accuracy of FMISO PET imaging, it might only be feasible to use static FMISO PET imaging for evaluating tumor hypoxia at some hospitals and research groups. Because there is still no established threshold to define tumor hypoxia with PET imaging [75], it is useful to know the most accurate FMISO PET threshold to define hypoxia. That is the goal of this chapter, made possibly by using EPROI as the ground truth of hypoxia by *in vivo* measurements of $pO_2 \leq 10$ mmHg.

FMISO PET is the most widely accessible hypoxia radiotracer for clinical studies [23, 76]. Clinical studies that used FMISO PET to identify and treat tumor hypoxia for boost dose escalation, e.g. Vera *et al.* with non-small cell lung cancer [10] and Welz *et al.* with head-and-neck cancer [19], found no evidence of higher toxicity to organs at risk when delivering a boost to hypoxic tumor subregions, which is a promising result for dose painting. Riaz *et al.* used FMISO PET in oropharyngeal cancer to distinguish normoxic tumors for dose de-escalation from 70 to 30 Gy, with remarkable evidence of tumor control at radiation doses with very mild side effect profiles [77].

In any case, the lack of unanimous definition of tumor hypoxia across research groups leads to a variation in tumor hypoxia definition that may affect treatment outcome. These inconsistencies can potentially have negative effects on patient survival and post treatment life style by over- or under-estimating – and therefore over- or under-treating – hypoxic volumes. Cited examples of FMISO-defined tumor hypoxia thresholds from oxygen-guided

Table 4.1: Summary of FMISO-defined hypoxia thresholds across different studies on hypoxia PET-guided radiation therapy.

Study	Tumor type	Hypoxia threshold
Welz *et al.* [19]	Squamous cell carcinoma of the head and neck	Kinetic analysis from dynamic FMISO PET [78]
Vera *et al.* [10]	Non-small-cell lung cancer	SUV $\geq$ 1.4
Riaz *et al.* [77]	Oropharyngeal cancer	TMR $\geq$ 1.2
Lindblom *et al.* [79]	Non-small-cell lung cancer	SUV $\geq$ 1.4 $\times$SUV$_{mean}$
Cheng *et al.* [80]	Head and neck squamous cell carcinoma	TMR $\geq$ 1.5
De Figueiredo [81]	Head and neck cancers	Fuzzy logic based locally adaptive Bayesian method
Hendrickson *et al.* [82]	Head and neck cancers	Not specified

radiotherapy studies are summarized in Table 4.1. Several listed studies were highlighted in a review article on oxygen-guided radiotherapy outcomes by Ferini et al. [17]. A more complete table on 35 studies using FMISO PET to image hypoxia in several tumor types can be found in Fleming *et al.* [75].

The presented research addresses the high variation in defining hypoxia with FMISO PET among research groups, using *in vivo* pO_2 EPROI images as ground truth hypoxia. The confounding variable of temporal variability of hypoxia [73] was minimized by the use of a custom-built hybrid PET/EPR imager [83]. This has the advantage of imaging tumor hypoxia in two modalities while the mouse remains in the same position and physiological conditions, avoiding registration issues that are often present in multi-modal studies. Using the hybrid PET/EPR imager was motivated by our observation that tumor hypoxia deepens over the course of several hours while a mouse is anesthetized (described in 4.6).

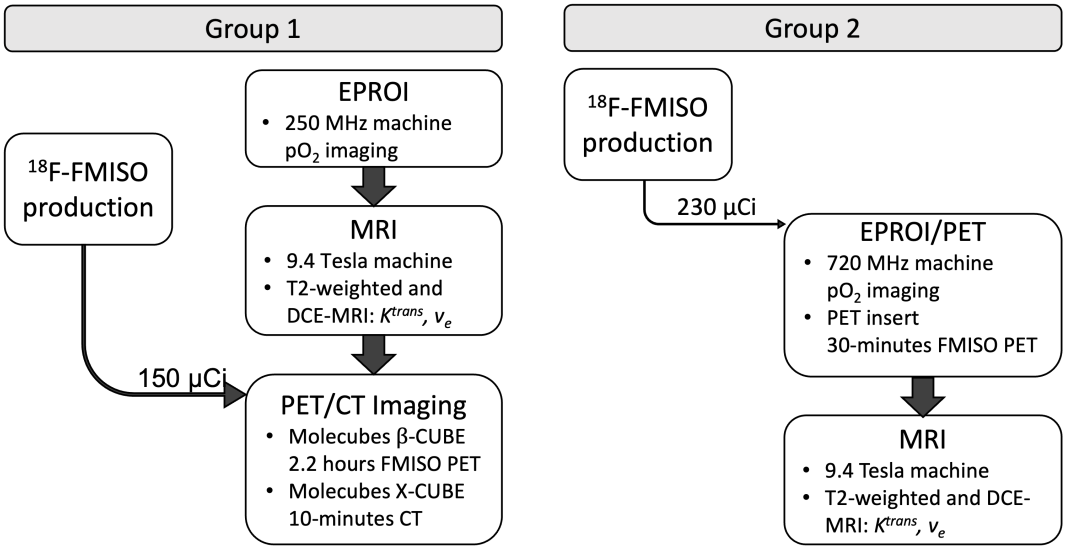

Figure 4.1: Summary of Group 1 and Group 2 imaging protocols.

4.2 Methods

Two imaging protocols were used for multi-modal imaging of tumor hypoxia, summarized in Figure 4.1 as Group 1 and Group 2. The same animal and tumor models were used as described in 3.2.3. A total of 13 MCa-4 tumor bearing mice were entered into the study for Group 1 (separate EPR and PET imagers); 15 SCC7, 10 FSa, and 6 MCa-4 tumors were used for Group 2 (hybrid EPR/PET imagers). Though DCE MRI was included in the imaging protocol, the resulting images and analysis will be discussed in Chapters 5 and 6.

The same guidelines for tissue and cell culture and animal model, anesthesia, and euthanasia were followed as described in 3.2.2 and 3.2.3.

4.2.1 Imaging Preparation

Following induction of anesthesia using 2% isoflurane mixed with air, the tumor-bearing leg was immobilized in a soft vinyl polysiloxane cast (GC America, Alsip, IL) and plastic bed using a previously published methodology [84]. A tail vein cannula was inserted to administer a bolus injection of FMISO, produced on-site as detailed in 4.2.3. An infusion of

Table 4.2: Comparison of PET imagers between Group 1 and Group 2. †SiPM: silicon photomultiplier. ‡MPPC: multi-pixel photon counter.

Feature	Group 1: Molecubes β-CUBE	Group 2: PET insert
Number of detector modules	9	14
Inner diameter	76 mm	60 mm
Axial field of view	13.3 cm	25.6 mm
Intrinsic resolution	0.76 mm	1.6 mm
Scintillators	25.4 × 25.4 × 8 mm thick monolithic LYSO scintillators coupled to an analogue †SiPM (Hamamatsu ‡MPPC)	Array of 8 × 4 LYSO scintillators (each crystal 3 × 3 × 10 mm) coupled to SiPMs (Hamamatsu MPPC)
Reconstruction algorithm	OSEM (ordered subset expectation maximization)	MLEM (maximum likelihood expectation maximization)
Compatibility for PET/MRI	Not compatible; standalone system	Compatible with 9.4-T small animal imager
FMISO PET: acquisition time 2 hours post-injection	10 minutes	20-30 minutes

oxygen-sensitive spin probe (OX071; GE Healthcare) was used for EPROI, and a bolus of gadodiamide (Omniscan; GE Healthcare) for DCE MRI.

4.2.2 PET and EPR Imagers

Tables 4.2 and 4.3 highlight key features of PET and EPR imaging systems used for Group 1 (Molecubes β-CUBE (Molecubes NV, Gent, Belgium) [85] and 250-MHz EPR [86]) and Group 2 (PET insert and 720-MHz EPR [83]).

4.2.3 Radionuclide Production

FMISO was produced on-site at the Cyclotron Facility by using an 18-MeV proton beam of the IBA Cyclone 18/9 system on an isotopically enriched oxygen 18 (^{18}O) water target. The ^{18}F was transferred to a lead-lined, shielded "hot cell," and the FMISO synthesis followed the

Table 4.3: Comparison of pulse EPR imagers between Group 1 and Group 2. †FBP: filtered back-projection.

Feature	Group 1: 250-MHz	Group 2: 720-MHz
Magnetic field strength	9 mT	25 mT
Loop-gap resonator inner diameter	19 mm	19 mm
Axial field of view	15 mm	15 mm
Intrinsic resolution	1.4 mm	1.0 mm
Reconstruction algorithm	†FBP	FBP
3D pO_2 image acquisition time	11 minutes	7 minutes

standard nucleophilic substitution reaction found in the literature [87]. After manufacturing FMISO, the drug was sterilized by filtration and sent for standard quality control testing. The product was released only after passing all tests except for the 14-day post injection sterility testing. There were no positive sterilities reported with any of the doses.

4.2.4 Imaging Protocol: Group 1

EPROI

Following preparation, each animal was inserted in the 250 MHz–pulsed EPR imager with its 9-mT magnetic field to image pO_2 in the tumor. Immediately upon insertion, the oxygen-sensitive spin probe solution was administered at 0.6 mL/h (70 mM OX071, pH of 7.3, normal osmolality). Infusion continued at 0.2 mL/h during tuning of the EPR resonator and adjustment of the EPR main magnetic-field and detection-circuit parameters. Fiducial images were obtained first, which was followed by 11-minute acquisitions of two EPR images using spin-lattice relaxation oxygen imaging [37]. The first image confirmed the presence of the oxygen spin probe throughout the entire tumor, and the second image was obtained once the probe was retained and relatively stable in the tumor. The second pO_2 image was

used for analysis.

A brief experiment with EPROI was also conducted on three mice with two pO_2 tumor images obtained approximately 1 and 5.5 hours under anesthesia to quantify long-term hypoxia development and calibrate the 10-mmHg hypoxia threshold, because the average time the mouse was under anesthesia between EPROI and FMISO PET imaging was 5.5 hours.

MRI

Following EPROI, each mouse was transported to a 9.4-T small animal scanner (Bruker, Erlangen, Germany) for T2-weighted MRI. Multisection spin-echo T2-weighted imaging for tumor localization was performed by using a rapid acquisition with relaxation enhancement (RARE) pulse sequence: repetition time, 4000 msec; echo time, 20 msec; field of view, 25.6 $\times$ 25.6 mm^2; matrix size, 256 $\times$ 256; section thickness, 0.75 mm; number of sections, 39; RARE factor, eight; and number of signals acquired, two.

FMISO PET/CT

The β-CUBE and X-CUBE were used for PET and CT imaging, respectively. Scanning started immediately after $\sim$150 μCi of FMISO was injected as a bolus into the tail-vein cannula, and a 130-minute dynamic PET scan was performed. The last 10-minute frame at 2 hours after injection was used for analysis. Finally, a CT image was obtained to enable anatomic co-registration with PET data and fiducial co-registration with images from EPROI and MRI.

4.2.5 Imaging Protocol: Group 2

EPROI and FMISO PET

Hypoxia images were acquired in the hybrid PET/EPRI machine [83], which operated at 720-730 MHz. To minimize time the mouse was anesthetized, once the tail-vein cannula was in place, a ∼230 μCi bolus of FMISO was injected. For EPROI, spin-probe infusion began 1.5 hours post-injection of FMISO. At least three pO_2 images were acquired at seven minutes each; the last image was used for analysis to be temporally near the FMISO PET image. Immediately after EPROI, a static 20–30-minute PET image was acquired 2 hours post-injection. PET/EPROI was not simultaneous due to RF-frequency interference.

MRI

After the mouse was transferred to the MRI facility, T2-weighted images were acquired on the 9.4-T small animal imager using the same protocol as for Group 1.

4.2.6 Image Preprocessing

The three-dimensional tumor contour and muscle contour were drawn manually by referencing the sharp-edge contrast between normal tissue and malignant tumor tissue (high voxel intensity) on each T2-weighted MR image and by using the ArbuzGUI MATLAB toolbox software developed at the Halpern Lab. PET data were converted to tumor-to-muscle ratio (TMR) and standardized uptake value (SUV) units. TMR was calculated in each voxel by dividing a tumor voxel value by the mean activity within the muscle ROI. SUV was calculated by first converting voxel values to units of μCi:

$$\mu Ci = CF \frac{DAQ_{1m}}{DAQ_{tumor}} \tag{4.1}$$

where CF is a predetermined conversion factor = 0.0104 from phantom studies, DAQ_{1m} = 23.7 minutes is the data acquisition time it took to obtain CF with 1 million counts, and DAQ_{tumor} is the minutes it took for data acquisition for an individual tumor. Using μCi, SUV was calculated using equation 4.2:

$$SUV_{region} = \frac{\mu Ci_{region}/volume_{region}}{Injected\,Dose_{mouse}/Weight_{mouse}} \tag{4.2}$$

where *region* is an individual voxel, and *volume* was converted to grams by estimating voxel density in the tumor to be identical to water (1 mm^3 = 0.001 gram).

For Group 1, PET/CT images were registered with VivoQuant software (Invicro, Boston, MA) guided by anatomic references. In both groups, images from all modalities were registered to the EPR image space by using the embedded fiducials and anatomic references. Images were resampled to isotropic PET voxel dimensions, which were 0.4 mm for Group 1 and 0.5 mm for Group 2.

4.2.7 Image Analysis

The optimal FMISO threshold to define hypoxia was determined by using EPROI as the reference truth for hypoxia, which is well-established as $pO_2 \leq 10$ mmHg [35] and calibrated to $pO_2 \leq 14$ mmHg for Group 1 (further detailed in 4.6).

FMISO-based hypoxia thresholds were defined by a variation of TMR and SUV thresholds commonly found in the literature [17]. Figure 4.2 shows a scatter plot from an example SCC7 tumor's pO_2 and SUV voxel values, and how true positive fractions (TPF) and false positive fractions (FPF) change based on the FMISO uptake threshold. The TPF is the fraction of voxels within a tumor that FMISO PET accurately classified as hypoxic; the FPF is the fraction of tumor voxels that FMISO PET misclassified as hypoxic but were actually normoxic. PET thresholds were defined by SUV $\geq$ X, where X ranges from 0 to 5. PET

thresholds were further evaluated by SUV $\geq$ X $\times$ SUV$_{mean}$ or SUV $\geq$ X $\times$ SUV$_{median}$, and SUV $\geq$ Y $\times$ SUV$_{max}$ where Y ranges from 0 to 1. Analysis was repeated for thresholds in TMR units.

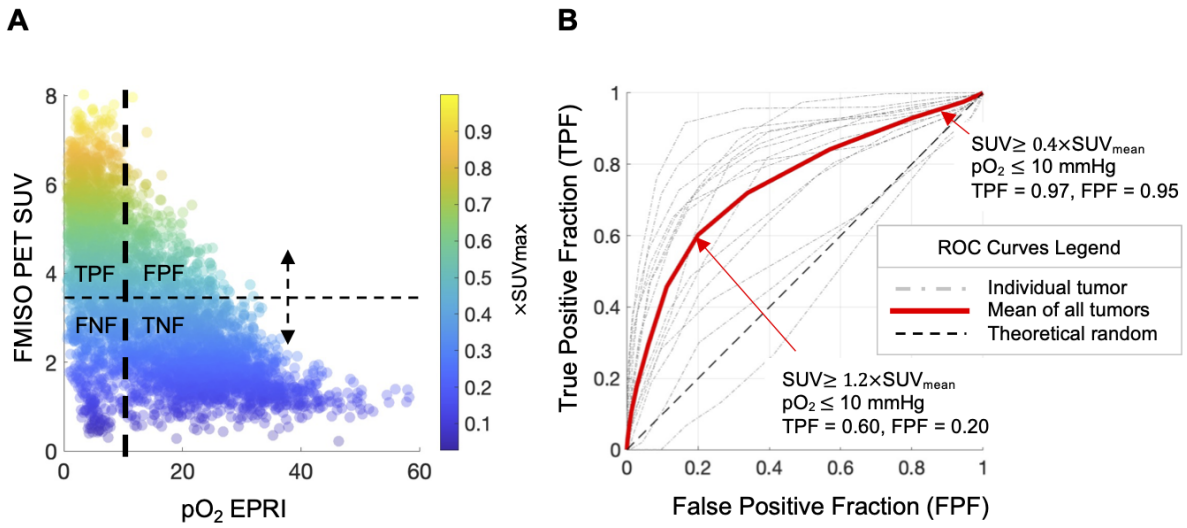

Figure 4.2: Left: Scatter plot of one tumor's voxels with corresponding pO_2 and FMISO uptake values, with the vertical dashed line showing the extablished EPROI hypoxia threshold at $pO_2 \leq 10$ mmHg. Right: ROC curves (grey) of all SCC7 tumors, and the mean ROC curve (red).

Three metrics were used to define similarity between hypoxia in EPROI and FMISO PET: Accuracy, Dice Similarity Coefficient (DSC), and the Hausdorff Distance (d_H). Visualizations of the DSC and d_H are shown in Figure 4.3. Accuracy was defined by the fraction of true positives (TP) and true negatives (TN) over the entire tumor including false positives (FP) and negatives (FN):

$$Accuracy = \frac{TP + TN}{TP + TN + FP + FN}. \tag{4.3}$$

The DSC is the ratio of the number of voxels in the overlapping region of hypoxia to the sum of the number of hypoxic voxels in each region:

$$DSC = 2|X \cap Y|/(|X| + |Y|), \tag{4.4}$$

where X and Y are hypoxic voxels defined by EPROI and PET, respectively.

The d_H is defined by:

$$h(X,Y) = \max\{(X,Y),(Y,X)\}, \tag{4.5}$$

where

$$(X,Y) = \sup_{x \in X} \inf_{y \in Y} d(x,y). \tag{4.6}$$

The $d_{H,95}$ measured the 95^{th} percentile of the greatest distance from the nearest points in the EPROI-defined hypoxic region to the FMISO PET-defined hypoxic region. The $d_{H,95}$ was normalized and subtracted from 1, denoted by $||d_{H,95}||$, so that all three metrics would range from 0 to 1 (lowest to highest similarity between the two hypoxic tumor subregions).

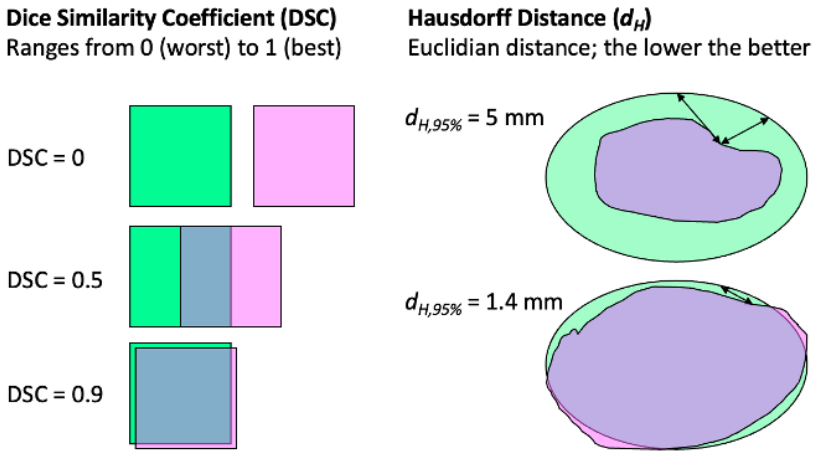

Figure 4.3: Example of DSC and d_H metrics.

4.3 Results

Table 4.4 summarizes the mean tumor volume and hypoxic fraction distributions for each group and tumor type, as well as the optimal FMISO threshold and its associated maximum overall hypoxic similarity (OHS_{max}). A potential confounding variable to consider throughout interpreting the results is the variability in hypoxic fraction across tumor types, further discussed in section 4.4.

Table 4.4: Mean ± standard deviation values of tumor volume and hypoxic fractions across imaging protocol groups and tumor types.

	Group 1: MCa-4	Group 2: MCa-4	Group 2: SCC7	Group 2: FSa
Tumor volume (mm^3)	370 ± 150	359 ± 140	307 ± 90	323 ± 140
HF10	0.21 ± 0.1	0.32 ± 0.1	0.19 ± 0.1	0.099 ± 0.1
N Subjects	9	6	15	10
Optimal FMISO Threshold	SUV≥ 1.2	SUV≥ 1.8	SUV≥ 1.4×SUV_{mean}	TMR≥ 1.4
OHS_{max}	0.67 ± 0.1	0.68 ± 0.3	0.73 ± 0.2	0.73 ± 0.3

Figure 4.4 shows the distribution of the DSC, $d_{H,95}$, Accuracy, and overall hypoxic similarity (OHS) for all potential FMISO uptake thresholds in SCC7 tumors: the mean OHS maximized at SUV≥1.4×SUVmean and SUV≥0.6×SUVmax (and the same for TMR), where OHS = 0.73 ± 0.2. Across all uptake units, the average DSC over 15 SCC7 tumors peaks within a range of 0.40 to 0.43; the $d_{H,95}$ is at a minimum between 3.1 and 3.2 mm; the accuracy plateaus between 0.81 and 0.83.

Figure 4.5 compares the OHS for all three tumor types imaged in Group 2, the hybrid PET/EPR imager. Figure 4.6 shows the distribution of OHS for MCa-4 tumors in Group 1 with and without using the calibrated pO_2 threshold to account for time under anesthesia. In general, for both pO_2 thresholds, the MCa-4 tumors imaged in Group 1 have a lower OHS than MCa-4 tumors imaged in Group 2.

Bar plots in Figure 4.7 highlight these results showing the FMISO uptake that resulted in the maximum OHS for each tumor type and unit on the left, and the respective OHS on the right. Using an unscaled value of TMR or SUV as the FMISO threshold for hypoxia resulted in the highest variability across tumor types (ranging from TMR or SUV ≥ 1.4 to 2.4). Using a scaled value of the mean TMR or SUV resulted in the lowest variability across tumor types (ranging from SUV ≥ 1.2×SUV_{mean} to 1.4×SUV_{mean}).

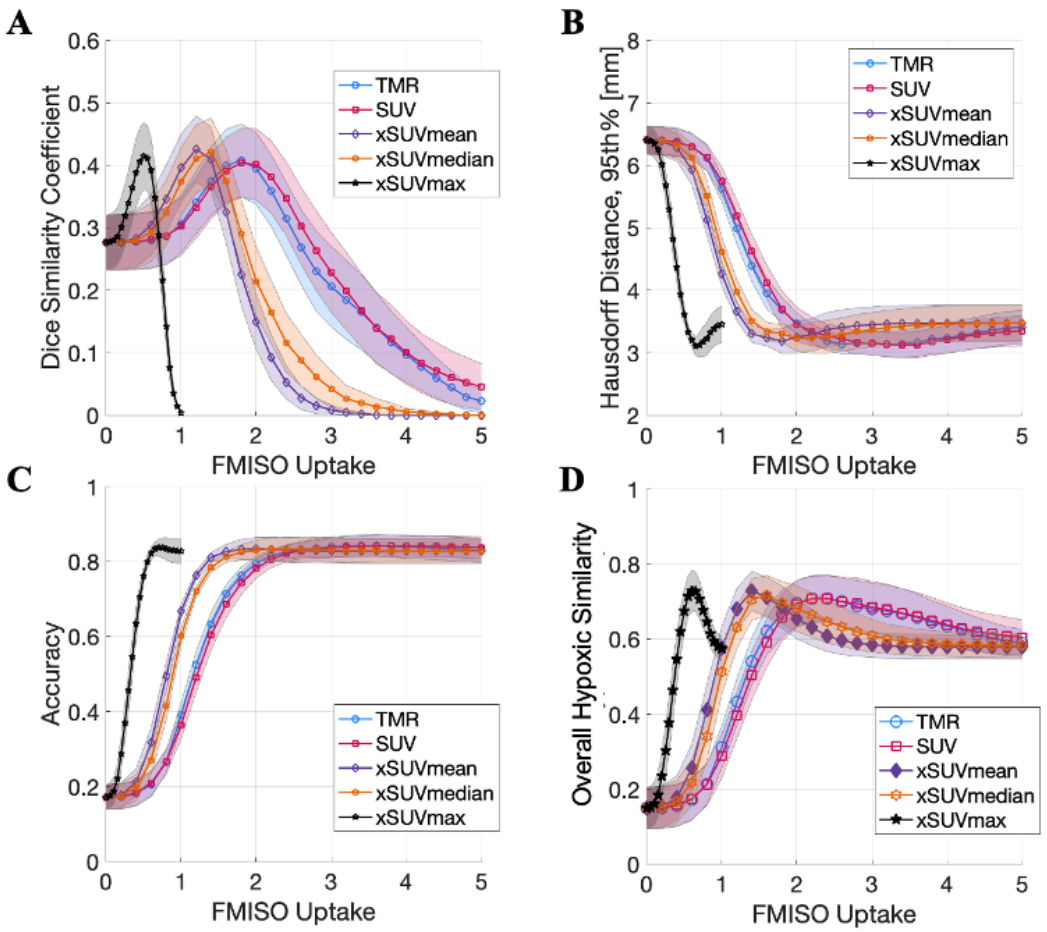

Figure 4.4: Tumor hypoxia overlap between FMISO PET/EPROI for select FMISO uptake units in SCC7 tumors. Shaded curves show mean and standard error across all tumors.

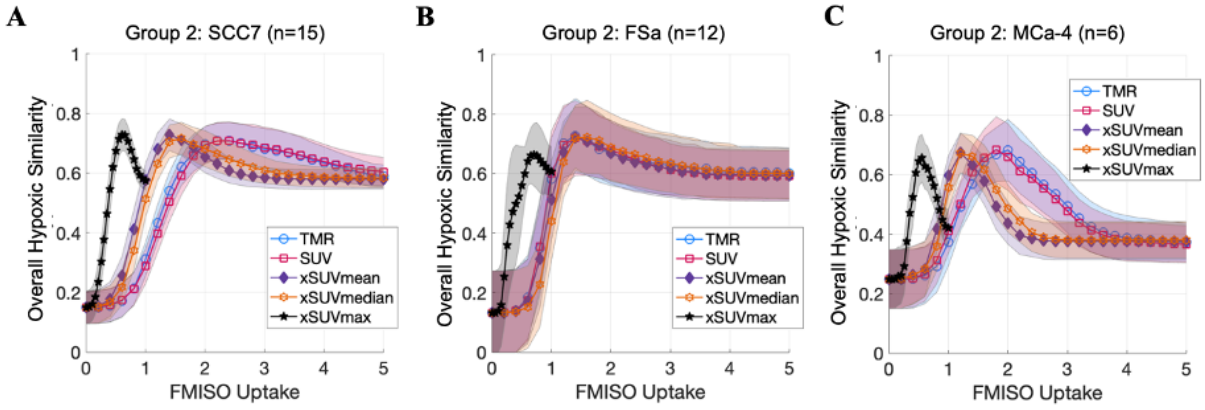

Figure 4.5: Overall Hypoxic Similarity (OHS) for all tumor types across Group 2, evaluating the optimal FMISO uptake threshold using with EPROI-defined $pO_2 \leq 10$ mmHg as ground truth of hypoxia. Markers show the mean; shaded regions show standard error.

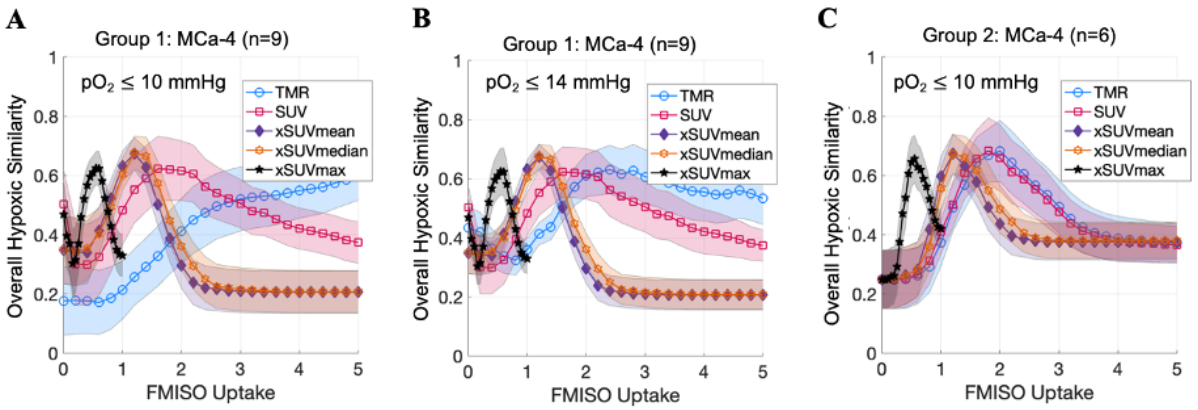

Figure 4.6: Distribution of OHS for MCa-4 tumors for different imaging protocol groups and pO_2 thresholds. Markers show mean; shaded regions show standard error.

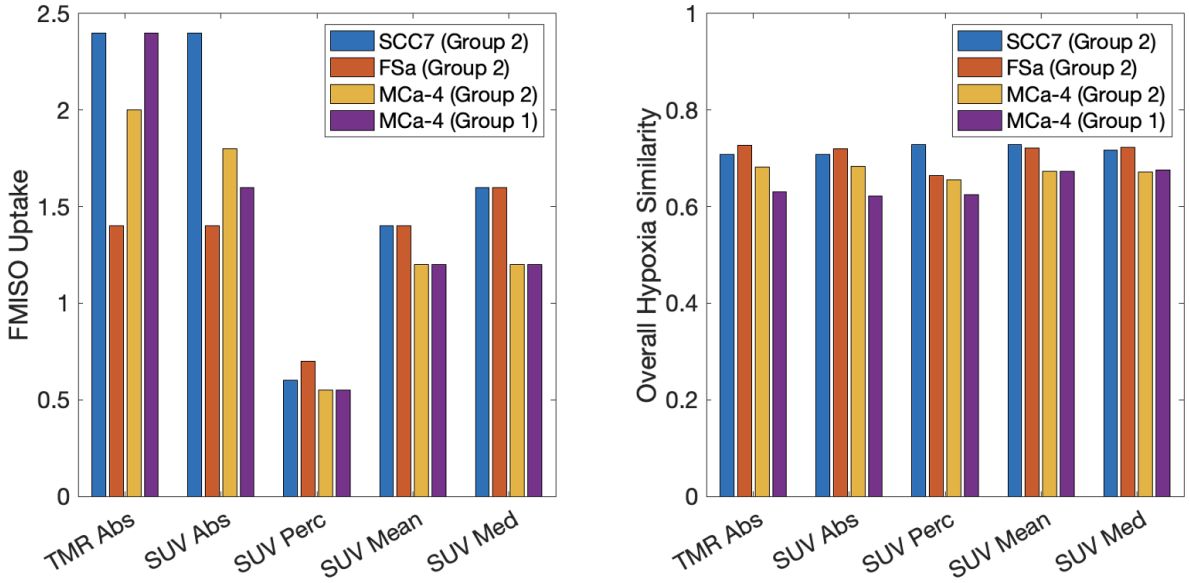

Figure 4.7: Summary of the FMISO uptake thresholds (left) with associated maximum OHS (right) for each uptake unit and tumor type.

4.4 Discussion

The importance of using the optimal FMISO threshold in locating tumor hypoxia for dose painting is in the risk of a too-high FMISO threshold, which could underestimate hypoxia with negative treatment outcomes. Small fractions of missed hypoxia in radiation treatment can still result in clonogenic hypoxic tumor cells resulting in clinical failure as discussed in Epel *et al.* [39]. This must be balanced by the risk of overestimating tumor hypoxia with an

FMISO threshold that is too low, which could result in over-treating a tumor and organs at risk.

Results from our study confirmed that the OHS between EPROI and FMISO PET images were maximized at similar *scaled* FMISO thresholds – SUV $\geq 1.4 \times \text{SUV}_{mean}$ for SCC7 and FSa tumors, and SUV $\geq 1.2 \times \text{SUV}_{mean}$ for MCa-4 tumors. However, the OHS_{max} for MCa-4 tumors was slightly higher for absolute thresholds of TMR ≥ 2.0 ($\text{OHS}_{max} = 0.68 \pm 0.2$) and SUV ≥ 1.8 ($\text{OHS}_{max} = 0.68 \pm 0.3$), and for FSa tumors TMR ≥ 1.4. Overall, the OHS for MCa-4 tumors was lower than for SCC7 and FSa tumors. This shows the importance of repeating this work across tumor types.

SUV units may be more appropriate than TMR because units of SUV do not require a subjective contour of a muscle ROI. The lower hypoxic fraction distribution of FSa tumors in our dataset showed that using a scaled value of SUV_{max} to define hypoxia is suboptimal for tumors that are predominately normoxic, as shown by the black curve in Figure 4.5.

The DSC and $\text{d}_{H,95}$ were dependent on the tumor's hypoxic fraction, where larger hypoxic fractions had higher DSC values (indicating better overlap) but also higher $\text{d}_{H,95}$ values (indicating worse overlap). This tradeoff supports the need for multiple metrics to define the quality of overlap between hypoxic tumor subregions shown in pO_2 EPROI vs FMISO PET, as done in this work.

A clinical study that was most similar to the oxygen-guided radiation therapy using EPROI described in the previous chapter is Vera's Phase II study [10], where 48% of the cohort's tumor histology were lung squamous cell carcinomas. A boost dose was delivered to hypoxic tumor regions defined by FMISO PET threshold of SUV ≥ 1.4. The study showed that FMISO uptake was strongly associated with poor patient prognosis, but delivering a boost dose to the hypoxic tumor regions did not reverse the outcome after two years. A *possibility* of why this was observed was a suboptimal choice of threshold to define hypoxia with FMISO. For example, when using the threshold SUV ≥ 1.4 in this study's squamous

cell carcinoma dataset, the mean ± standard deviation of the DSC was 0.38 ± 0.2 and $d_{H,95}$ was 9.2 ± 2 mm. The $d_{H,95}$ increased by almost 6mm compared to the use of the optimal threshold of SUV $\geq 1.4\times SUV_{mean}$. This large discrepancy between definitions of hypoxic tumor regions could result in suboptimal boost targets for treatment, which affects patient outcome.

Another recent clinical study by Welz *et al.* confirmed the prognostic value of dose escalation (DE) to hypoxic subvolumes in head and neck cancer [19]. The study found a 100% 5-year local tumor control for non-hypoxic patients compared to 74% for hypoxic patients (p=0.039). Comparing hypoxic patients, there was a 25% increase in 5-year local tumor control for hypoxic patients treated with DE compared to hypoxic patients treated with standard radiotherapy (p=0.15). However, dynamic FMISO PET imaging was required to derive the hypoxic volume with kinetic analysis [78, 88], and the high complexity of the study setup led to slow accrual and premature closure of the study. This supports the necessity of a more simple approach to imaging and analysis for locating and treating hypoxic subregions.

One limitation to the presented study is that MCa-4 tumors were imaged with different machines and protocols, where mice in Group 1 (N=9) had 3-4 hours between EPROI and FMISO PET, while mice in Group 2 (N=6) had near-simultaneous PET/EPR imaging in the hybrid machine. The pO_2 threshold was calibrated from 10 to 14 mmHg for tumors in Group 1 to address the deepening of tumor hypoxia over the time the mouse was anesthetized. However, other differences in the imaging protocol may have influenced the generally low OHS between EPROI and FMISO PET, such as MR imaging in between hypoxia imaging, or different intrinsic resolutions between machines.

The resolution differences between preclinical EPR and PET imaging modalities were <1mm (summarized in Table 4.2 and Table 4.3). All multimodal tumor images in Group 2 were resampled to isotropic 0.5mm output voxel resolution of the PET image, so pO_2 images were upsampled from their 0.67mm isotropic resolution. Tumor images in Group

1 were resampled to isotropic 0.4mm output voxel resolution of the PET image, since the Molecubes β-CUBE had higher sensitivity and spatial resolution than the prototype PET insert used in Group 2. The effect of resampling would mostly affect similarity metrics at the edges of hypoxic tumor subregions, which straddle each threshold to define hypoxia.

Another limitation to our study is the lack of radiation treatment outcome results when delivering boost doses to these optimally defined hypoxic tumor subregions imaged with FMISO PET. However, this is the only *in vivo* study to use EPROI as the ground truth for tumor hypoxia, and the validity of using EPROI to define and treat hypoxia has been previously verified and published [39, 86]. Our optimal threshold for defining hypoxia with FMISO PET falls within the range of clinical studies using FMISO to locate tumor hypoxia for radiation boosts in multiple tumor types (Table 4.1).

The generally low DSC and high $d_{H,95}$ values across all tumor types, especially for the MCa-4 mammary adenocarcinomas, show the need for a potential correction to FMISO PET images using DCE MRI. This chapter aims to identify the optimal FMISO PET threshold for clinical settings where only static FMISO PET imaging is feasible. The next chapter includes analysis with parametric images from DCE MRI, as well as H&E and immunohistochemical staining of excised tumor tissue, to identify physiological properties of these tumors and their microenvironment that may be causing discrepancies between locating tumor hypoxia with EPROI versus FMISO PET.

4.5 Conclusions

This is the first *in vivo* comparison of FMISO uptake with EPR pO_2 images in three pre-clinical tumor models using two sets of EPR/PET imaging systems. Using three metrics of similarity to quantify the maximum overall hypoxia overlap, the optimal thresholds are found to be SUV $\geq 1.4\times SUV_{mean}$ for SCC7 and FSa tumors, and SUV ≥ 1.8 for MCa-4 tumors. The hybrid PET/EPR imager was used to ensure identical physiological conditions

of the mouse during imaging upon confirmation of deepening hypoxia in the tumor while a mouse is anesthetized. Over all tumors, the relatively low mean DSC and high $d_{H,95}$ suggest the need to apply a correction to FMISO PET images.

4.6 Appendix: Calibrating the pO_2 Hypoxia Threshold with EPROI

The slope of a linear fit for pO_2 voxel values between the 1- and 5.5-hour time points the mouse was under anesthesia were calculated within tumor and muscle ROIs. Pearson correlation coefficients quantified the correlation strength between oxygenated muscle tissue vs malignant tumor tissue.

The slopes of pO_2 tumor voxel values between two EPR imaging time points were 0.48, 0.61, and 0.65; Pearson correlations were 0.197, 0.701, and 0.675. For the muscle, the slope was 0.75, 0.82, and 0.72; the correlations were 0, 0.538, and 0.249. These results for the tumor are summarized in Figure 4.8, showing how pO_2 decreases over time at a higher rate in tumor than muscle tissue when a mouse is under anesthesia. As a result, the threshold of hypoxia for EPR images was calibrated to $pO_2 \leq 14$ mmHg for Group 1 data to account for deepening hypoxia in tumor tissue when comparing to FMISO PET hypoxia images from 3-4 hours later after the mouse was under anesthesia for 5-6 hours.

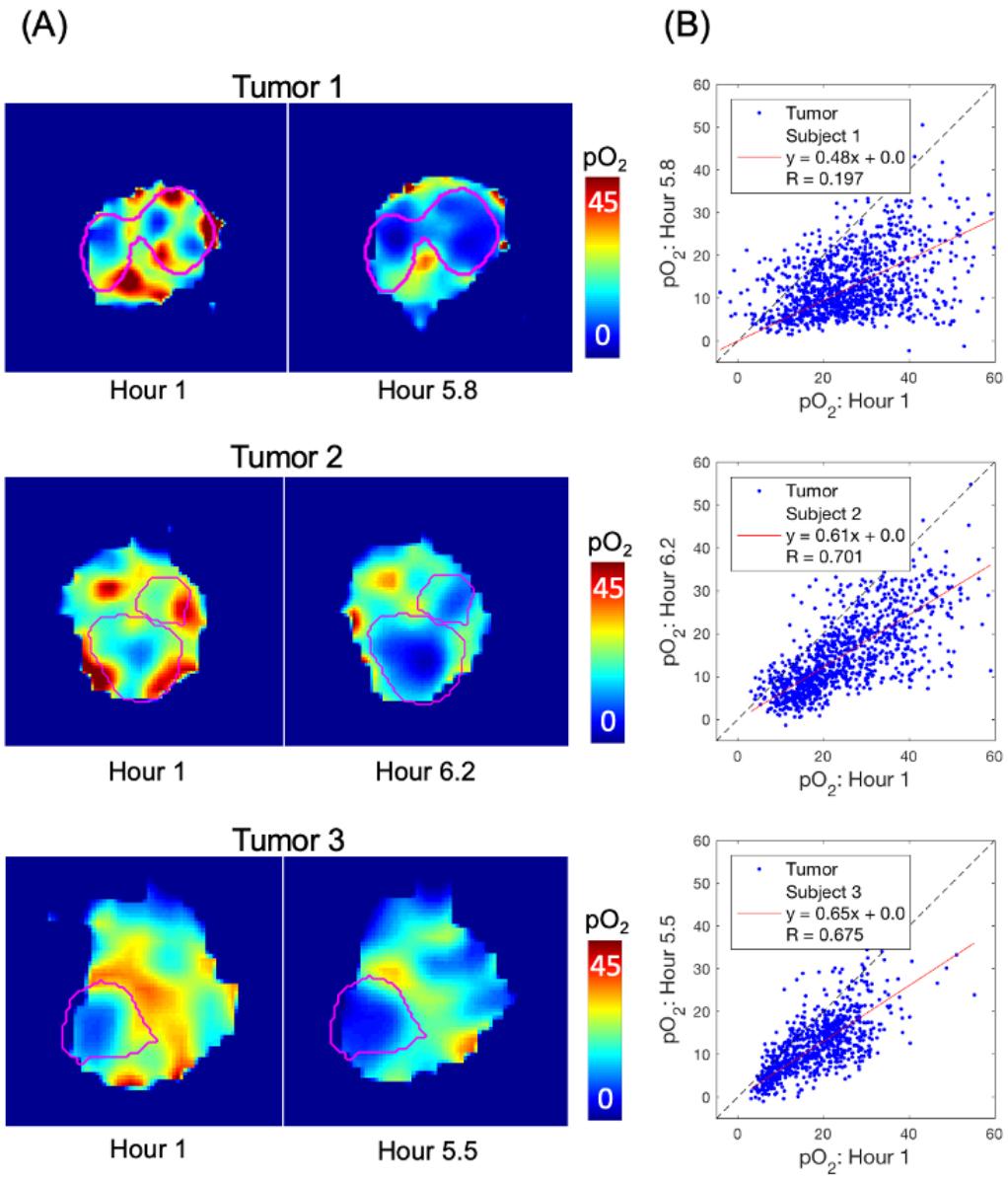

Figure 4.8: (A) EPR images of three tumors acquired approximately 1 and 5.5 hours after the mouse was anesthetized. (B) Scatter plots of the same voxels within each respective tumor between time points (Hour ∼1 on horizontal axis, Hour ∼5.5 on vertical axis).

CHAPTER 5

COMBINING *IN VIVO* AND HISTOLOGICAL IMAGING TO INVESTIGATE RELATIONSHIPS BETWEEN TUMOR VASCULATURE AND HYPOXIA

5.1 Introduction

While tumor hypoxia can be categorized as diffusion or perfusion limited, hypoxia can also induce angiogenesis, which would lead to increased diffusion and perfusion in some areas of the tumor. This could generate contradictory features imaged by DCE MRI. The heterogeneity of the tumor microenvironment, both spatially and temporally, adds another layer of complexity. The purpose of this chapter is to identify relationships between pO_2 and FMISO uptake with tumor physiology modeled by DCE MRI, and identify features where FMISO misclassifies the presence or absence of hypoxia. Additionally, histological images were obtained and registered to *in vivo* axial slices to qualitatively analyze features on a microscopic scale. This is the first study to use near-simultaneous EPR/PET imaging to assess relationships between tumor hypoxia with K^{trans}, v_e and k_{ep} (previously described in Chapter 2.3).

In the past decade with the emergence of PET/MR imaging and a focus on tumor microenvironment, there have been studies comparing FMISO PET uptake with DCE MRI parametric images in several tumor types. Simoncic *et al.* studied head and neck cancer patients to provide some of the missing knowledge for FMISO PET/DCE MRI protocol optimization [89]. Carmona-Bozo *et al.* compared hypoxia and perfusion in breast cancer using simultaneous PET/MRI to support the hypothesis of perfusion-driven hypoxia in breast cancer [90]. Pinker *et al.* compared multiparametric FDG/FMISO PET and MRI in cervical cancer to investigate non-invasive detection of tumor heterogeneity for an improved planning of chemo-radiation therapy [91]. Gerstner *et al.* performed a prospective,

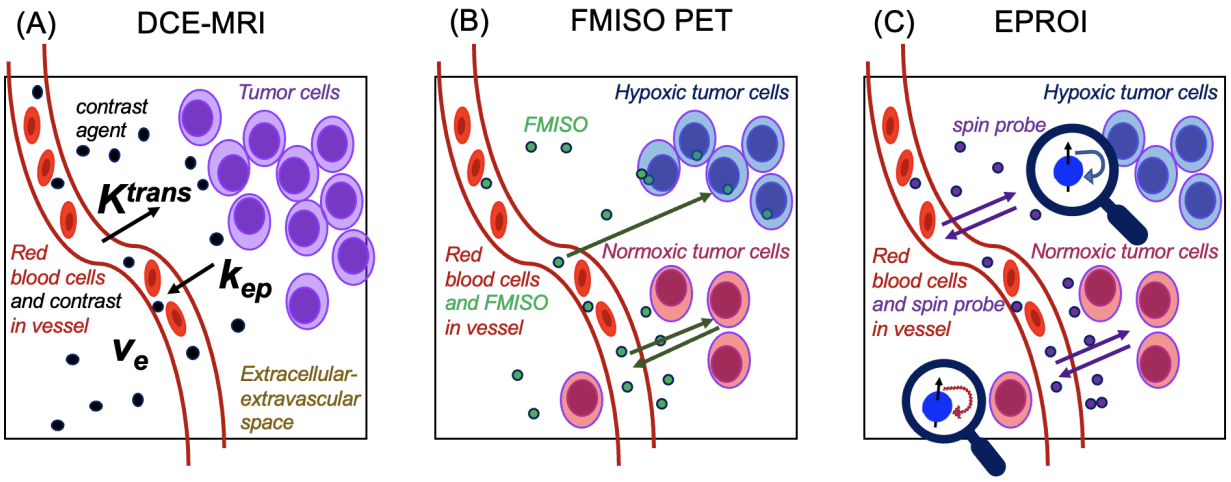

Figure 5.1: Models of tracer behavior in (A) DCE MRI with gadolinium contrast agent, (B) FMISO PET, and (C) EPROI with the oxygen-sensitive spin probe.

multicenter study to test the hypothesis that abnormal tumor vasculature and hypoxia, as measured with DCE MRI and FMISO PET, will negatively impact survival in patients with newly diagnosed glioblastoma [92]. Jansen *et al.* assessed neck nodal metastases and found that hypoxic nodes are poorly perfused compared to non-hypoxic nodes [93]. Hillestad *et al.* related oxygen supply and consumption to K^{trans} and v_e, respectively, and combined them to generate hypoxia images in both xenograft and patient tumors [58].

The diversity of these studies utilizing both FMISO PET and DCE MRI shows the wide net that can be cast in terms of potential analysis with PET/MR imaging. However, relationships between vascular permeability/perfusion and hypoxia identified in one tumor type may not apply to another. Additionally, researchers must be careful to avoid misinterpreting what images from each modality are showing, and their limitations.

Figure 5.1 shows models of each modality and its tracers for A) DCE MRI, B) FMISO PET, and C) EPROI. In Figure 5.1A, K^{trans} is the measure of the contrast agent's influx rate out of the blood compartment, k_{ep} is the measure of the contrast agent's reflux rate back into the blood compartment, and v_e is the fractional extracellular-extravascular space. There is no distinction between hypoxic or normoxic tumor cells using DCE MRI. It is

imaging and modeling the concentration of a contrast agent over time, and the models can be imperfect. Figure 5.1B shows how FMISO is retained intracellularly in hypoxic tumor cells, and is not retained in normoxic tumor cells but instead diffuses away. Figure 5.1C is supposed to show how an unpaired electron (in the magnifying glass) has a low relaxation rate near hypoxic tumor cells in the absence of oxygen, and a high relaxation rate near oxygenated cells. The behavior of all these tracers can be related to tumor hypoxia and impact patient outcome, but we must recognize that the clinical utility of indirect methods to measure oxygen/hypoxia are not necessarily based on rigorous measurements of oxygen [94], and so relating oxygen supply and consumption to K^{trans} and v_e like in Hillestad *et al.* may not be appropriate.

Ex vivo imaging with IHC staining is also advantageous in resected human tumors if *in vivo* imaging is not feasible. Pimonidazole is often used as the gold standard marker for hypoxia, but unlike HIF-1α, pimonidazole needs to be injected into humans or animal models before the tumor can be excised. Janssen *et al.* conducted IHC staining on squamous cell carcinomas of the head and neck using HIF-1α, pimonidazole, and combined CD31 staining with the proliferation markers IdUrd and Ki-67 [95]. They observed a low colocalization of pimonidazole and HIF-1α (0.02%-25%), a more homogenous distribution for HIF-1α than pimonidazole, and no significant correlation between pimonidazole and HIF-1α fractions in the ten tumors studied. Here we can determine whether these results are reproducible across our three tumor types, which include an oral squamous cell carcinoma murine model, but using *in vivo* EPROI and FMISO PET to locate tumor hypoxia.

This chapter explores several relationships between tumor hypoxia images with vasculature in three parts. First, Spearman (monotonic) correlations were calculated in each tumor to assess correlation strength between EPR pO_2 and FMISO uptake with DCE MRI parametric images. Second, 1st order features (e.g. mean, skewness, entropy, etc.) were compared across tumors in regions classified as true positive (TP), true negative (TN), false

positive (FP), and false negative (FN) by FMISO PET, using EPROI as the ground truth to define hypoxia. Third, histological images of IHC staining of HIF-1α and CD31 were used to identify nuclear expression of HIF-1α and endothelial cells, respectively. Hematoxylin and Eosin (H&E) staining was used to identify necrosis and tumor boundaries. Similar regions between *in vivo* and histological images were compared across tumor types in regions of hypoxia/normoxia, poor/good perfusion, and necrosis. Repeating analysis in SCC7, MCa-4, and FSa tumors allows us to investigate tumor-type dependence on the effects of FMISO uptake and pO_2 with physiological properties imaged by DCE MRI and IHC.

5.2 Methods

Tumor images from Group 2's imaging protocol with the near-simultaneous FMISO PET/EPROI and DCE MRI were used for analysis. The same animal and tumor models were used as described in 3.2.3. A total of 15 SCC7, 9 FSa, and 5 MCa-4 tumors were included in this study. A total of n=6 tumors (two for each type) were excised for H&E and IHC staining.

5.2.1 In Vivo Imaging Protocols

A 9.4-T small animal scanner (Bruker) was used for T2-weighted and DCE MRI. The details of the PET and EPR imagers were summarized in section 4.2.2, and of T2-weighted imaging protocol in section 4.2.4. The imaging protocol is summarized in Figure 4.1.

T1-weighted DCE-MR images were obtained by using a temporal resolution of 5 seconds and the following parameters: repetition time, 78.125 msec; echo time, 1.2 msec; field of view, 25.6 $\times$ 25.6 mm^2; matrix size, 128 $\times$ 64; flip angle, 30°; section thickness, 0.75 mm; and number of sections, 21. The DCE MRI data were continually acquired before (for 1 minute), during, and after a bolus injection of 0.2 mmol/kg of gadodiamide (Omniscan; GE Healthcare) for a total duration of 10.67 minutes (128 frames).

Parametric images were generated with DCE MRI data analyzed by using MATLAB and

an in-house software package. DCE MRI signal intensity curves were converted to contrast agent concentration curves, C(t), as a function of time, t, using a previously published method [96]. A precontrast (before the administration of a contrast agent) T1 value of 2.2 seconds for muscle and a relaxivity value of 3.34 $mM^{-1}sec^{-1}$ for gadodiamide were used in the calculations [97]. The standard Tofts model and previously published methods were used to obtain maps of the physiologic parameters K^{trans} and v_e [98–100]. The reflux rate, k_{ep}, was calculated by dividing K^{trans} by v_e.

5.2.2 Histological Imaging Protocols

To prepare tumors for histological staining, the tumor-bearing mouse leg was skinned and cut in half axially at the tumor center. The length of the tumor was typically 10-12 mm, and needed to be cut to allow the formalin to penetrate through the center. The leg was then separated from the corpse and dropped into a jar containing formalin for 36-48 hours. The leg was then transferred into decalcification solution for two hours, after which the tumor (including surrounding muscle and decalcified bone to aid in registration with MRI images) was cut into two 5-mm axial sections at the center and set in labeled cassettes (Figure 5.2A). The solution was rinsed with dewater and transferred into 70% ethanol for 24-36 hours.

Four serial paraffin sections were prepared with 5 μm thickness every 500 μm (Figure 5.2B) for multiparametric immunohistochemistry stained for H&E, CD31 (1:200 dilution; ab28364, Abcam), and HIF-1α (1:1000 dilution; NB100-479SS, Novus Biologicals). The fourth serial section provided a back-up in case of staining mishaps and/or future work. This resulted in sixteen potential slices in each tumor for multiparametric IHC analysis.

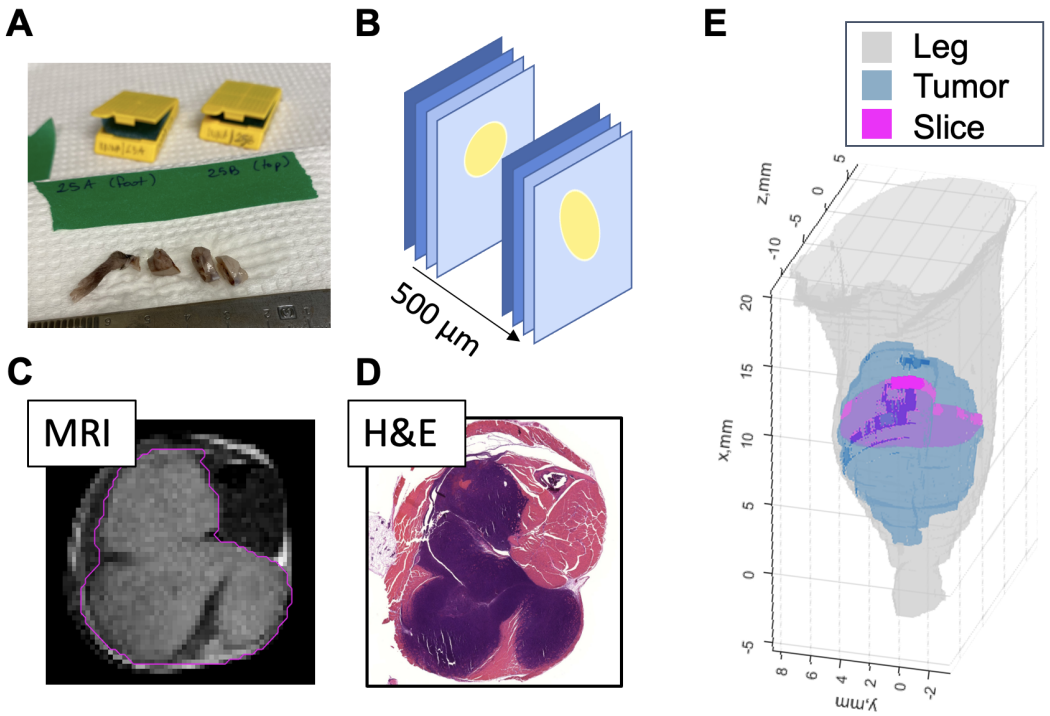

Figure 5.2: Examples of (A) excised tumor cut in two 5mm sections, (B) the sectioning protocol, (C) MRI and (D) H&E slices registered to each other, and (E) the associated slice location in the tumor.

5.2.3 Image Analysis: In Vivo

Preprocessing

The same registered and resampled images as described in 4.2.6 were used for analysis. To remove outliers, maximum voxel values of pO_2 to were capped at 50, FMISO SUV and TMR at 5, and K^{trans} and v_e and k_{ep} at 1. The minimum value of all images was zero. Each image, X, was normalized from -1 to 1 as shown in Equation 5.1:

$$X_{norm} = \frac{(2X - X_{max})}{X_{max}}. \tag{5.1}$$

Spearman Correlations

Spearman correlation coefficients (ρ) were calculated for each tumor between EPR pO_2, FMISO PET uptake, K^{trans}, v_e, and k_{ep}. Absolute ρ values <0.3 were considered weak, 0.3-0.5 were considered moderate, and 0.5-1.0 were considered strong. These thresholds for correlation strength had been previously used by Jansen *et al.* [93].

Feature Analysis

Using $pO_2 \leq 10$ mmHg and tumor-type specific FMISO thresholds found in Chapter 4 (SUV $\geq 1.4 \times \text{SUV}_{mean}$ for SCC7, SUV ≥ 1.8 for MCa-4, and TMR ≥ 1.4 for FSa) to define hypoxia, masks were generated to define the four classifications of tumor hypoxia: TP, FP, FN, and TN. TP indicates both FMISO- and EPROI-defined hypoxia, FP indicates when FMISO misclassified a voxel as hypoxic when it is actually normoxic, FN indicates when FMISO misclassified a voxel as normoxic when it is actually hypoxic, and TN indicates both FMISO- and EPR- defined normoxia. Table 5.1 lists and describes the 1st-order texture features that were used.

Features were grouped by the entire tumor set (N=29), then subgrouped by tumor type. Figure 5.3 shows an example of an axial slice from an SCC7 tumor's *in vivo* images. The bar plot in (Figure 5.3F) shows mean values of K^{trans}, v_e, and k_{ep} in those classified regions for the whole tumors, quantifying how v_e is lowest and k_{ep} is highest in TN regions, while K^{trans} is similar across all classification regions. One-way analysis of variance (ANOVA) was used to identify whether the group mean of a feature was significantly different ($p<0.05$) between FMISO hypoxia classification.

5.2.4 Image Analysis: Ex Vivo

Sectioned and stained slides were scanned with 40x-resolution digital light field microscope, and imported into CaseViewer and QuPath software for viewing. The H&E slide was manu-

Table 5.1: Description of first-order features.

Feature	**Measure**
Minimum	The lowest voxel value.
Maximum	The highest voxel value.
Mean	The average voxel value.
Median	The median voxel value.
Variance	The measure of the spread of the distribution about the mean.
Skewness	The measure of asymmetry of the distribution about the mean. A positive skewness implies the tail on the right side of the distribution is longer; a negative skewness implies the tail on the left side of the distribution is longer.
Kurtosis	The measure of how peaked the distribution of values are. A higher kurtosis implies the mass of the distribution is concentrated towards the tail(s); a lower kurtosis implies that the mass of the distribution is concentrated towards a spike near the mean.
Entropy	The measure of randomness or uncertainty.

ally registered to the T2-weighted axial MRI image that most closely resembled its anatomical features (example slices in Figure 5.2C and 5.2D). Boundaries between tumor and muscle cells were distinguished by the dark purple stains of tumor cell nuclei and large pink muscle tissue.

With guidance from a pathologist, regions of necrosis were identified by H&E. HIF-1α expression in the tumor cell nucleus vs cytoplasm was discerned. CD31 stains of endothelial cells were dark brown with high contrast against blue cells.

Using anatomic landmarks such as tumor orientation and bone location, image regions were then compared to *in vivo* axial slices. Hypotheses included (a) necrotic regions corresponded to areas of low K^{trans} and high v_e, (b) areas without CD31 stains corresponded to hypoxia, (c) areas with CD31 stains correspond to higher K^{trans} values, and (d) nuclear HIF-1α expression corresponded to hypoxic regions.

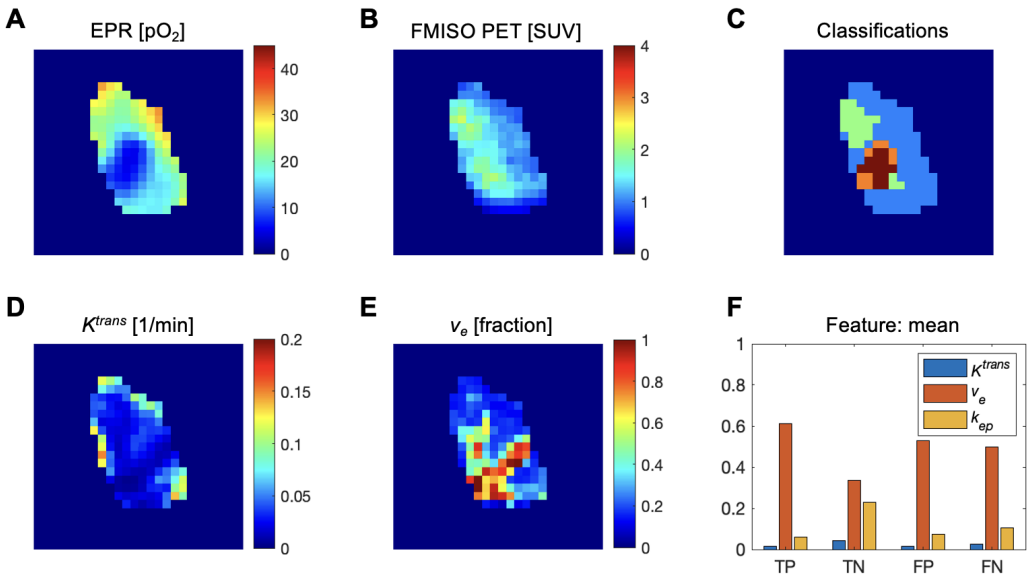

Figure 5.3: (A) EPROI and (B) FMISO PET images were used to visualize the (C) hypoxia classification of TP (red), TN (blue), FP (green), and FN (orange). Classification regions were applied to DCE MRI images (D) K^{trans} and (E) v_e for feature analysis. An example of mean DCE MRI values across regions is shown in (F).

5.3 Results

5.3.1 Spearman Correlations

Correlation strengths are plotted against the hypoxic fraction in Figure 5.4. All tumors with HF10>0.05 had negative ρ values between FMISO SUV vs K^{trans} (Figure 5.4A), and positive correlations between EPR pO_2 vs K^{trans} (Figure 5.4D). This supports that in a hypoxic tumor with lower perfusion/vascular permeability (low K^{trans}), FMISO uptake would increase, and pO_2 would decrease. FSa tumors with HF10<0.05 had positive correlations between FMISO SUV vs K^{trans}.

Comparing ρ between FMISO uptake with EPR pO_2, 47% (7/15) of SCC7 tumors and 11% (1/9) of FSa tumors had strong correlations. No strong correlations were observed for MCa-4 tumors.

Comparing ρ between FMISO PET with K^{trans}, 60% (9/15) of SCC7 tumors had

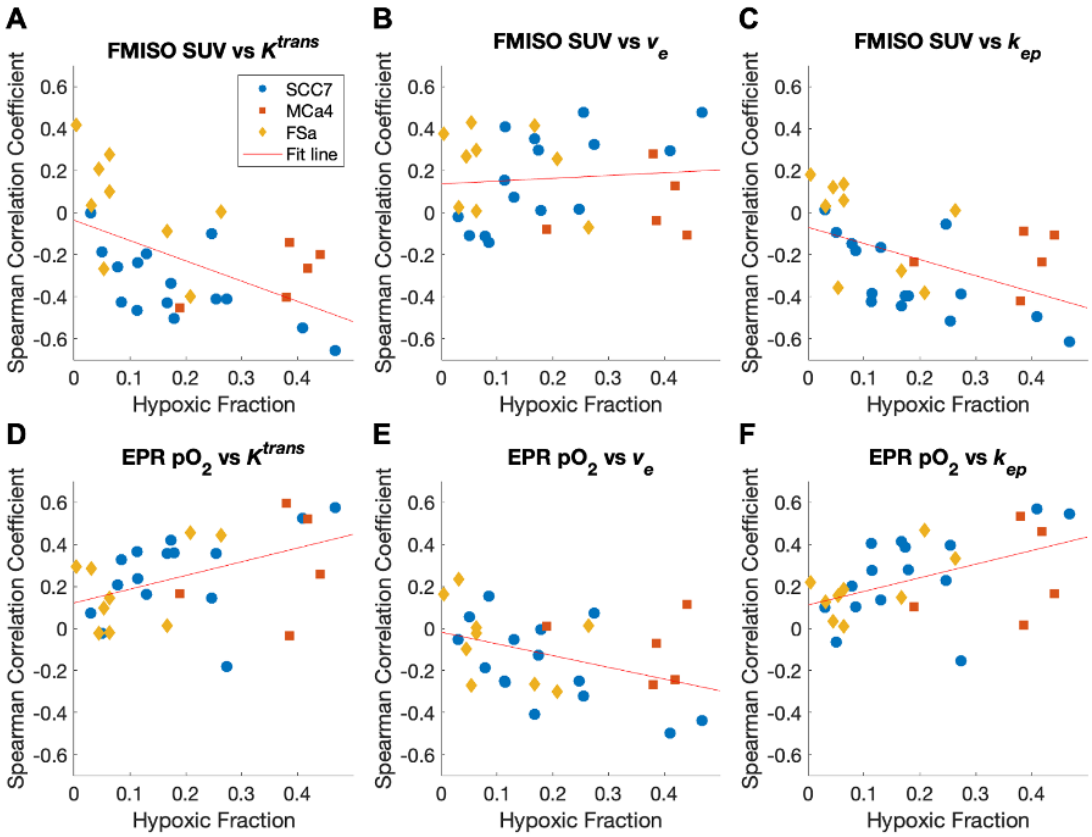

Figure 5.4: Spearman correlation coefficients against the hypoxic fraction of each tumor for FMISO uptake vs DCE MRI (top) and EPR pO_2 vs DCE MRI (bottom).

moderate-to-strong positive correlations. For EPR pO_2 with K^{trans}, 53% (8/15) of SCC7 tumors had moderate-to-strong negative correlations ; 40% (2/5) of MCa-4 tumors had strong negative correlations and 60% had weak correlations. This suggests that in MCa-4 tumors, FMISO uptake may be inhibited by areas of low perfusion, but in actuality, those regions are correlated with low pO_2 (as validated by EPROI). Similar observations were made with FMISO PET with k_{ep} and EPR pO_2 with k_{ep}. No strong correlations were observed between PET/EPR with v_e.

5.3.2 Feature Analysis

Over all tumor types (n=29), mean and median v_e were significantly higher for TP regions than TN regions (both p<0.03), shown in Figure 5.5A. This suggests that a high fraction of extracellular-extravascular space might distinguish hypoxic from normoxic tumor regions. The kurtosis of v_e was significantly higher for TN regions than TP (p=0.001) and FN (p=0.03) regions, shown in Figure 5.5D. This indicates that in normoxic regions there is a wide distribution of v_e voxel values, contributing to lower mean values, while in hypoxic regions the distribution of v_e voxels is concentrated around the high mean value.

Mean k_{ep} was significantly higher for TN than TP (p=0.01) and FP (p=0.04) regions, meaning the reflux rate is higher in normoxic areas, which is expected. Mean k_{ep} was also significantly higher in FN than TP regions (p=0.03), meaning the reflux of FMISO caused a false negative classification of hypoxic voxels. This is shown in Figure 5.5A.

The skewness of k_{ep} was significantly higher in TP regions than FN or TN regions (both p<0.01), where skewness of $k_{ep} = 1.3$ in TP regions and skewness of $k_{ep} = 0.23$ and 0.07 in FN and TN regions, respectively (see Figure 5.5B). Entropy of k_{ep} was significantly higher in TN regions compared to TP, FN, and FP regions (all p≤0.03), shown in Figure 5.5C. This suggests a more heterogeneous/chaotic distribution of k_{ep} values in normoxic regions compared to hypoxic regions.

When comparing features across all tumors, there was no significant difference between hypoxia classification in K^{trans}. However, when repeating feature analysis for each tumor type, the maximum of K^{trans} was significantly lower (p=0.02) in TP vs TN regions only for FSa tumors. This suggests that correlation between hypoxia and low vascular permeability/perfusion is tumor-type dependent, and the relationship cannot be generalized. In all other instances, there were only significant differences between certain features and hypoxia classifications for SCC7 tumors, not FSa or MCa-4 tumors.

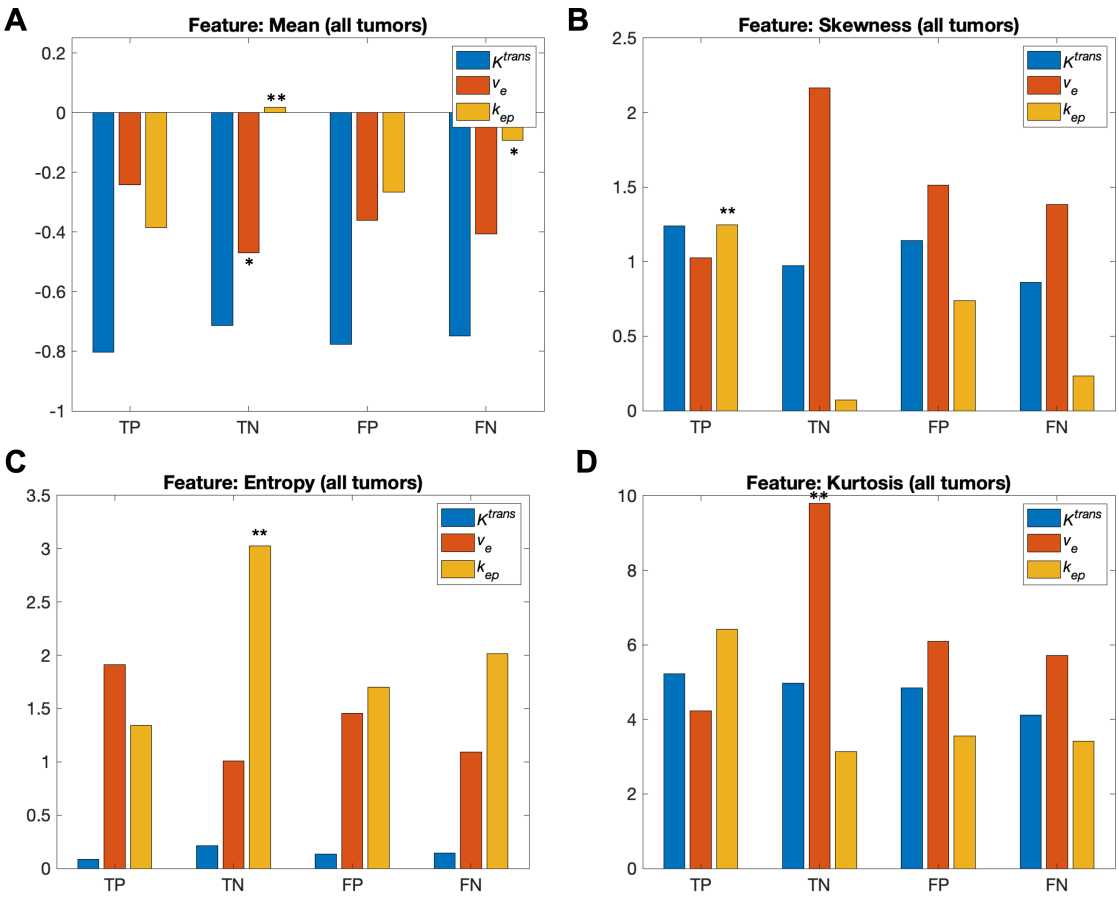

Figure 5.5: Select features of DCE MRI parametric images in hypoxia classification regions. Asterisks indicate regions significantly different from others, where * = p≤0.05 and ** = p≤0.01.

5.3.3 Comparison In Vivo With Histological Images

Figures 5.6-5.8 show (A) *in vivo* axial slices to compare to (B) registered histological slices. H&E, HIF-1α, and CD31 images were magnified by ∼20 times to show different regions marked by red and black arrows. The tumor is contoured in magenta in (A).

The center of the SCC7 tumor (Figure 5.6), marked by the red arrow and magnified in (C), showed necrosis in the H&E stain and hypoxia in the EPR pO_2 image. There was also higher K^{trans} and low v_e in that region. While this may be paradoxical, there is vascular growth surrounding the hypoxic region shown by CD31 staining. In the well-oxygenated region (black arrow) magnified in (D), there were more densely-packed tumor cells with

HIF-1α expression in the nuclei, with microvasculature spread throughout.

In the MCa-4 tumor (Figure 5.7), the red arrow points to a region of hypoxia, high FMISO uptake, low K^{trans} and high v_e. There are large stromal structures shown throughout the tumor slice (C), with stronger HIF-1α expression immediately surrounding large vasculature structures. In the well-oxygenated region (black arrow) there is stronger HIF-1α expression throughout the region surrounding stromal and vascular structures.

In the FSa tumor (Figure 5.8), there is virtually no hypoxia in the whole tumor despite very low K^{trans} and high v_e shown on the right side of the tumor (red arrow), magnified in (C). There are heterogeneously-sized tumor cells infiltrating large pink muscle cells, and higher HIF-1α expression in cell cytoplasm rather than the nucleus. There is also very little CD31 staining, which validates the low K^{trans} shown *in vivo*. In the region that straddles the edge of high/low K^{trans} (black arrow) magnified in (D), H&E images show a collagenous region with sparsely spread tumor cells, no nucleic HIF-1α expression, and some vasculature.

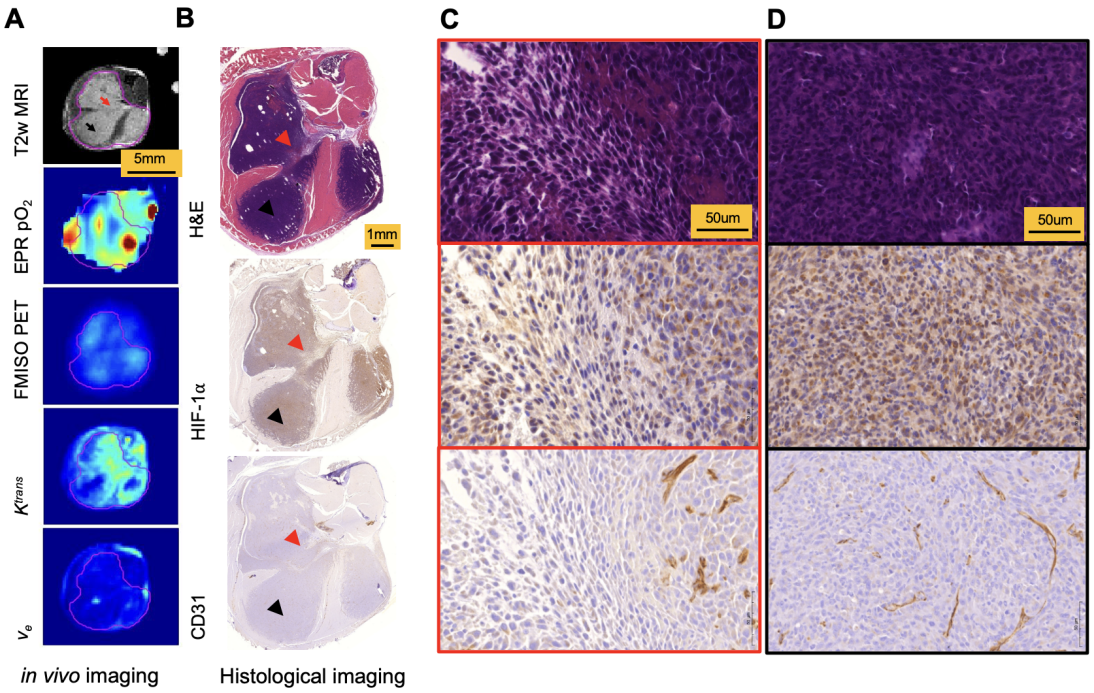

Figure 5.6: SCC7 tumor axial slices (A) *in vivo* and (B-D) histological imaging.

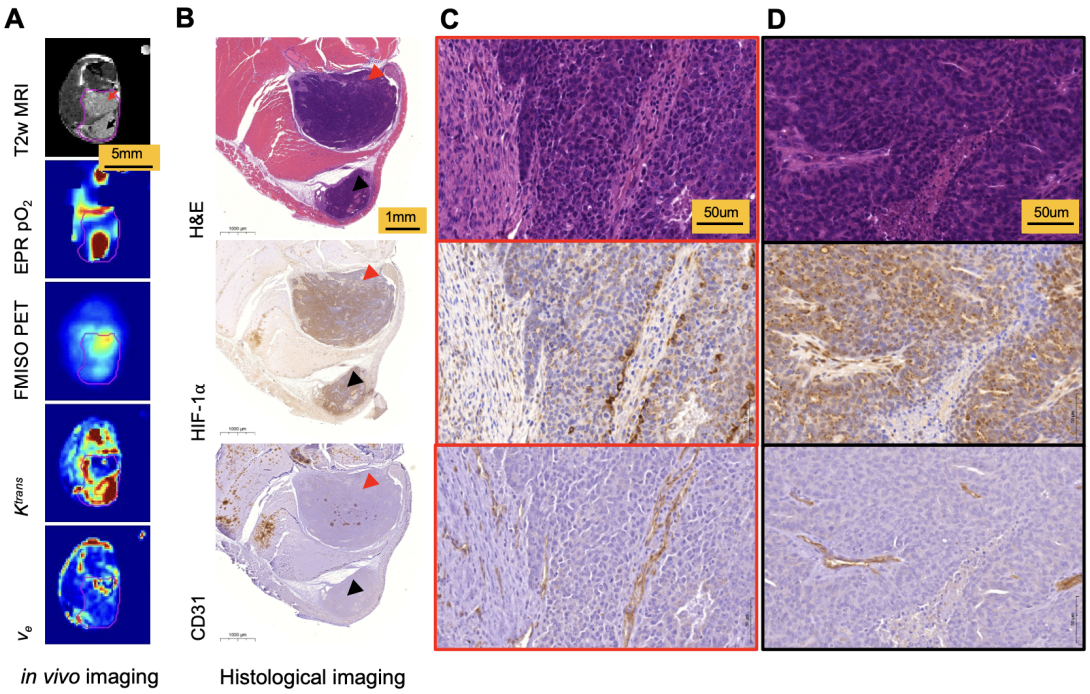

Figure 5.7: MCa-4 tumor axial slices (A) *in vivo* and (B-D) histological imaging.

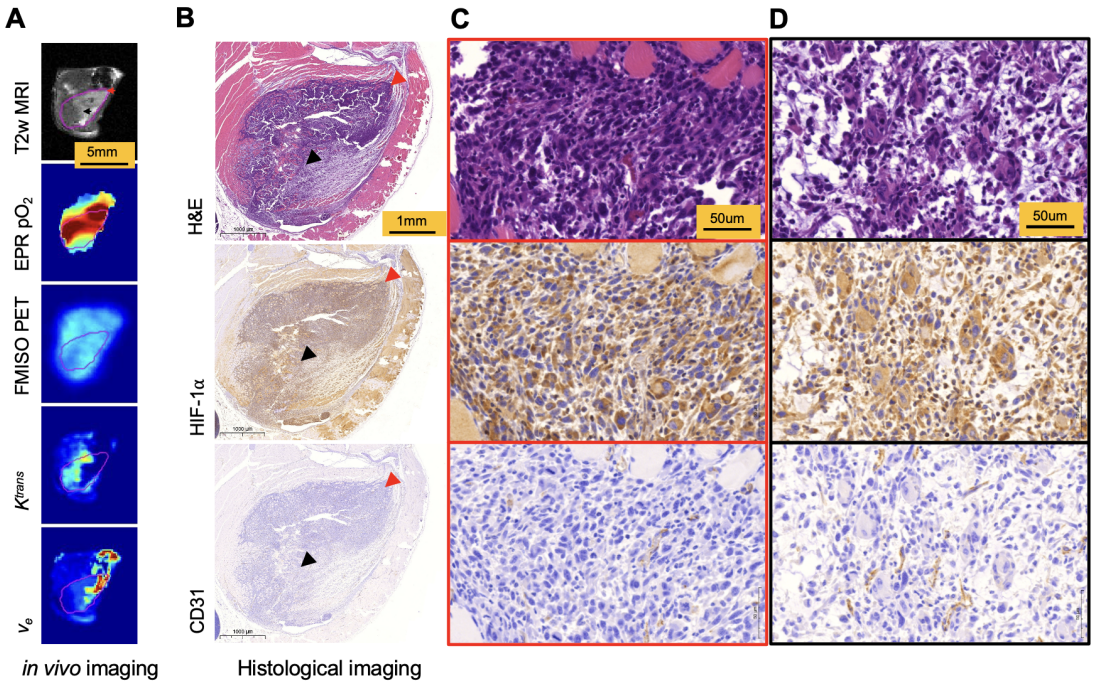

Figure 5.8: FSa tumor axial slices (A) *in vivo* and (B-D) histological imaging.

5.4 Discussion

In literature comparing DCE MRI with FMISO PET, there have been contradictory correlations between FMISO PET uptake with K^{trans} in head and neck cancer patients. Simoncic *et al.* observed positive correlations between FMISO uptake and K^{trans} [89], while Jansen *et al.* observed negative correlations [93]. Another study by Donaldson *et al.* observed negative correlations between perfusion measured by DCE MRI with pimonidazole and vascular endothelial growth factor (VEGF) expression [101]. Common results across studies, including ours, were the generally weak correlations between FMISO uptake with v_e.

In this chapter we showed consistently negative correlations between K^{trans} and FMISO uptake in SCC7 tumors —an oral squamous cell carcinoma model. This is in concordance with the theory that low perfusion is associated with low pO_2 and hypoxia, a positive correlation would be expected between EPR pO_2 with K^{trans}. Using EPROI we showed a positive correlation between pO_2 and K^{trans}, observed in 14/15 SCC7 tumors.

Looking at all tumor types, there were strong negative correlations observed between FMISO uptake with K^{trans} for some SCC7 tumors, but not MCa-4 or FSa tumors. There were strong positive correlations observed between EPR pO_2 with K^{trans} for SCC7 and MCa-4 tumors, but no FSa tumors. However, the low hypoxic fraction of FSa tumors included in this study make it difficult to draw solid conclusions for fibrosarcomas.

The discrepancies in correlations in MCa-4 tumors suggests that FMISO uptake may be inhibited by areas of low perfusion, while in actuality those regions are correlated with low pO_2 (as validated by EPROI). That, combined with the lack of strong correlations between FMISO with pO_2 for MCa-4 tumors, implies that MCa-4 mammary adenocarcinomas may not be an appropriate tumor type to use FMISO PET alone for imaging hypoxia.

A major limitation is that only five MCa-4 tumors were included in analysis. This was due to a series of experiment failures, including temporarily broken MRI and PET machines, scheduling conflicts caused by inconsistent tumor growth rates of MCa-4 tumors,

and premature anesthetic death of the animal before all images could be acquired. Therefore, it is possible that the lack of statistically significant observations with MCa-4 tumors was due to a low N, rather than the tumor type itself.

The purpose of identifying features that showed significantly different values across hypoxia classification regions was to find some feature(s) that could differentiate FN regions from TP, FP, and TN. This is because missing a region that is hypoxic could be more detrimental to patient outcome if it resulted in an inaccurate dose plan. With DCE MRI, only k_{ep} features showed significant differences between FN and FP regions compared to TN and TP regions. However, feature values of FN or FP regions were often in the middle of TP and TN values, which would make them difficult to identify on their own.

In looking at IHC stains across tumor types, tumor regions without CD31 staining – i.e. regions without blood-delivering vasculature – were more strongly associated with necrosis than low K^{trans}. Additionally, HIF-1α expression was not localized only to hypoxic tumor regions, but throughout the whole tumor, with darker nucleic stains around blood vessels stained with CD31. This supports that in the presence of hypoxia, and surrounding necrosis, HIF-1α induces angiogenesis [102, 103]. However, it also means that HIF-1α is not an appropriate marker for locating hypoxic subregions since it is present throughout the entire tumor. We initially considered there was overstaining, but there was no HIF-1α expression in healthy muscle cells.

The study by Janssen *et al.* [95] observed that HIF-1α staining was localized mainly in the nucleus, similar to our observation in SCC7 and MCa-4 tumors, but not FSa tumors. However, those FSa tumors had a low hypoxic fraction. Janssen *et al.* also noticed HIF-1α staining closer to blood vessels than pimonidazole. However, if oxygen concentration decreases with distance from blood vessels, and if HIF-1α expression is oxygen dependent, it would be expected that HIF-1α would be upregulated farther from blood vessels. This expected relationship was not observed in neither our study nor in Janssen *et al.*, and is

another indication that HIF-1α might not be suitable as a marker for chronic hypoxia when using IHC.

A limitation to this study is that only two tumors were used for histological imaging. However, those tumors are representative of the whole group. For example, one SCC7 tumor had a hypoxic core with high similarity between FMISO PET/EPROI-defined hypoxia and high FMISO uptake, while the other had a heterogeneous spread of hypoxia with low similarity between FMISO PET/EPROI-defined hypoxia and low FMISO uptake.

Further analysis should be conducted to explore second-order feature analysis or machine learning techniques to distinguish FN from TN regions of hypoxia by combining FMISO PET with DCE-MRI. Imaging experiments are still ongoing to include more tumors in analysis to be able to make more concrete conclusions.

5.5 Conclusions

This is the first instance of comparing DCE MRI parametric images — K^{trans}, v_e, and k_{ep} — with hypoxia images from both FMISO PET and EPROI. Here we showed that the strength of monotonic correlations between FMISO PET/EPROI with K^{trans} and k_{ep} have a moderate correlation with the tumor's hypoxic fraction, and that there are generally moderate correlations with low K^{trans} and hypoxia (low pO_2 and high FMISO uptake). We also showed that features in k_{ep} could be used to distinguish between FMISO PET's hypoxia classification of false positive or false negative. However, differences between true positive and true negative hypoxia classifications were more statistically significant. This sets the stage for the next chapter, which involves modeling and correcting FMISO PET with EPROI and DCE MRI.

CHAPTER 6

MODELING AND CORRECTING FMISO PET WITH PO_2 AND DCE MRI

6.1 Introduction

FMISO PET is an indirect method of measuring oxygen in tissue, or rather, the absence of oxygen in tissue [94]. However, there is utility in modeling pO_2 with FMISO uptake to use the clearly-defined *in vivo* hypoxia threshold: $pO_2 \leq 10$ mmHg. A study by Toma-Dasu *et al.* described a sigmoidal function to model the inhibition of chemical reactions [79, 104]. Their fitted data was then used to generate radiosensitivity maps to offer the possibility of improved treatment results, taking heterogeneity and dynamics of hypoxic regions into account. Parameters from their sigmoidal equation were applied to our data, and compared to a newly developed logistic function for a more accurate model of pO_2 to FMISO uptake.

Some of the first experiments to show the efficacy of FMISO accumulating in hypoxic tumor cells were done by Rasey as *in vitro* studies and showed logistic relationship between pO_2 and FMISO uptake [105, 106]. This was the inspiration to develop a logistic function to model FMISO uptake with EPROI, using image data acquired with the hybrid PET/EPR imager [83].

This chapter looks at various methods of modeling pO_2 with FMISO PET and DCE MRI. Part A compares a newly developed logistic model to a previously published model, using pO_2 to estimate FMISO uptake. Part B shows a proof-of-concept correction algorithm, showing the potential of combining FMISO PET with DCE MRI parametric images to improve the accuracy of FMISO PET.

6.2 Methods

The same animal and tumor models were used as described in 3.2.3, and the same methods for PET/EPR/MRI acquisitions were used as previously described in sections 4.2.2 and 5.2.1. For image analysis, all images were registered and resampled to isotropic 0.5 mm voxels in PET/EPR space and PET images were converted to units of SUV. Further detailes were previously described in 4.2.6.

6.2.1 Image Analysis Part A: Modeling FMISO uptake with pO_2

Tumor images from Group 2 imaging protocol of EPROI, FMISO PET, and DCE MRI were used for analysis in modeling FMISO uptake with pO_2. A total of 15 SCC7, 9 FSa, and 5 MCa-4 tumors were included in analysis.

Three models were evaluated in their ability to predict FMISO uptake, denoted as PET^M where ^{M} stands for "modeled". Model 1 is the novel logistic function (Equation 6.2). Model 2 is a sigmoidal function with previously published parameters by Toma-Dasu *et al.* (Equation 6.3) [104]. Model 3 uses the same sigmoidal function as Model 2, but with new parameter values fitted to our data. Figure 6.1 shows an example of models over true FMISO PET/EPROI voxel values, where Model 1 is red, Model 2 is yellow, and Model 3 is purple.

The minimum root mean square difference (RMSD) between true PET and modeled PET (PET^M) was used to identify optimal parameters for each tumor with N voxels:

$$RMSD = \sqrt{\frac{\sum_{i=1}^{N} (Uptake_i - Uptake_{Model}i)^2}{N}} \tag{6.1}$$

One-way analysis of variance (ANOVA) was used to evaluate significant differences between group mean RMSD values for each model.

Model 1 is described by a logistic function as a model of FMISO retention in hypoxic cells with the point of inflection occurring at the *in vivo* threshold of hypoxia (10 mmHg).

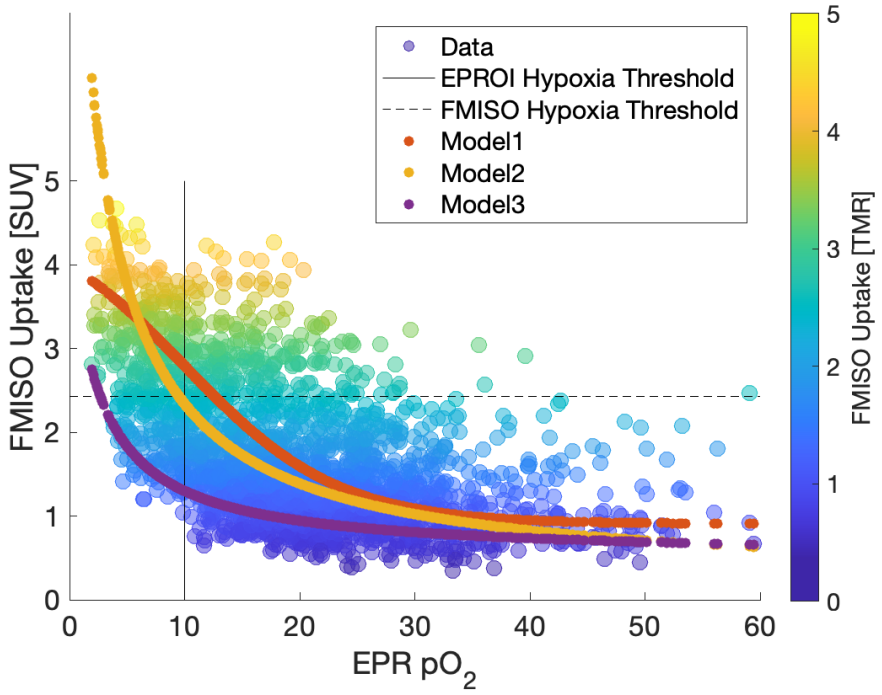

Figure 6.1: Scatter plot FMISO uptake and pO_2 from EPROI for one SCC7 tumor, with the three FMISO uptake models superimposed over the raw data.

Equation 6.2 describes the model,

$$PET_1^M = \alpha + \frac{\beta}{1 + e^{\gamma(pO_2 - 10)}} \tag{6.2}$$

where α is the 15^{th} percentile of FMISO uptake ($\text{SUV}_{15\%}$), $\beta = SUV_{max} - SUV_{15\%}$, and $\gamma = 0.15$. Mean and standard deviation parameter values are $\alpha = 0.87 \pm 0.23$, $\beta = 3.0 \pm 1.5$. The variable pO_2 is a vectorized EPR image, where each element is a voxel value of pO_2.

Model 2 is shown in Equation 6.3,

$$PET_2^M = A - \frac{B \times pO_2}{C + pO_2} \tag{6.3}$$

where A related to the reaction speed in the absence of the inhibitor of the enzymatic reduction of the FMISO in the presence of oxygen, and the second term (with B and C)

described the inhibition effect [107]. They found that the best fit resulted from parameter values $A = 10.9, B = 10.7$, and $C = 2.5$ mmHg.

Model 3 uses Equation 6.3, but new parameter values of A, B, and C were fit to our data. The best fit (lowest RMSD) resulted from parameter values $A = 4.5, B = 4.0$, and $C = 2.5$ mmHg.

6.2.2 Image Analysis Part B: Correcting FMISO Uptake with DCE MRI

Tumor images from both Group 1 and Group 2 imaging protocols were used for analysis, though only tumors with a HF10 ≥ 0.05 were used. This eliminated one SCC7 tumor and three FSa tumors. In total, 14 SCC7, 6 FSa, and 13 MCa-4 tumors were included in analysis. Images were normalized between -1 and 1 as described in 5.2.3.

A correction algorithm using least squares fitting was evaluated in its ability to make FMISO PET more accurate in locating hypoxia for each tumor voxel by looping across 27-element cubes throughout the tumor volume. This method was implemented to take the heterogeneity of the tumor into account.

To start off simply, if we have two real-valued variables $x \in \mathbb{R}$ and $y \in \mathbb{R}$ with some unknown mapping function, we can write this as

$$y = f(x). \tag{6.4}$$

In this case, we are mapping some function of FMISO PET and DCE MRI images, $f(x)$, to a known map of pO_2, y.

If we make N observations of the mapping, we'd have a list of y_n and x_n for $n = 1, 2, ..., N$ observations in vectors $\vec{y}$ and $\vec{x}$. In this case, N observations would be up to 27 elements in a cube in the tumor (fewer at the tumor's edge).

If we expand the mapping f into a linear combination of M functions $\phi_m(x)$ with weight-

ing coefficients w_m for $m = 1, 2, ...M$, we can write this as

$$f(x; w_1, w_2, ..., w_M) = \sum_{m=1}^{M} w_m \phi_m(x), \tag{6.5}$$

or more succinctly as vectors,

$$f(x; \vec{w}) = \vec{w} \cdot \vec{\phi}(x). \tag{6.6}$$

We want to choose weights $\vec{w}$ to minimize the sum of squared differences between $\vec{y}$ and $\vec{w} \cdot \vec{\phi}(x)$, which we write as

$$\hat{\vec{w}} = \underset{\vec{w}}{\operatorname{argmin}} \|\vec{y} - \vec{w} \cdot \vec{\phi}(x)\|_2^2 \tag{6.7}$$

To simplify notation, we can define a matrix $\mathbf{X}$ where $X_{nm} = \phi_m x_n$ and rewrite Equation 6.7 as

$$\hat{\vec{w}} = \underset{\vec{w}}{\operatorname{argmin}} \|\vec{y} - \mathbf{X}\vec{w}\|_2^2. \tag{6.8}$$

The closed-form solution to this is given by

$$\hat{\vec{w}} = \mathbf{X}^+ \vec{y} = (\mathbf{X}^T \mathbf{X})^{-1} \mathbf{X}^T \vec{y} \tag{6.9}$$

where $\mathbf{X}^+$ is the Moore-Penrose pseudoinverse of $\mathbf{X}$. Now we can perform a linear least squares fit to map some combination of FMISO PET uptake with DCE MRI parametric images and find the optimal weighting coefficients to do so.

To do this, normalized PET/EPR/MRI images were vectorized and Model 1 described in Equation 6.2 was used to predict FMISO retention in hypoxic cells. However, another set of parameters was used to give the logistic model a steeper slope and binarize FMISO uptake to minimum and maximum values. Parameters used in Equation 6.2 were $\alpha = SUV_{min}$, $\beta = SUV_{max} - SUV_{min}$, and $\gamma = 0.85$. Figure 6.2 shows the logistic function with both sets of parameters, where the black curve shows Model 1B used in analysis.

The residual vectorized difference $\vec{R}$ is defined in Equation 6.10, where positive values of

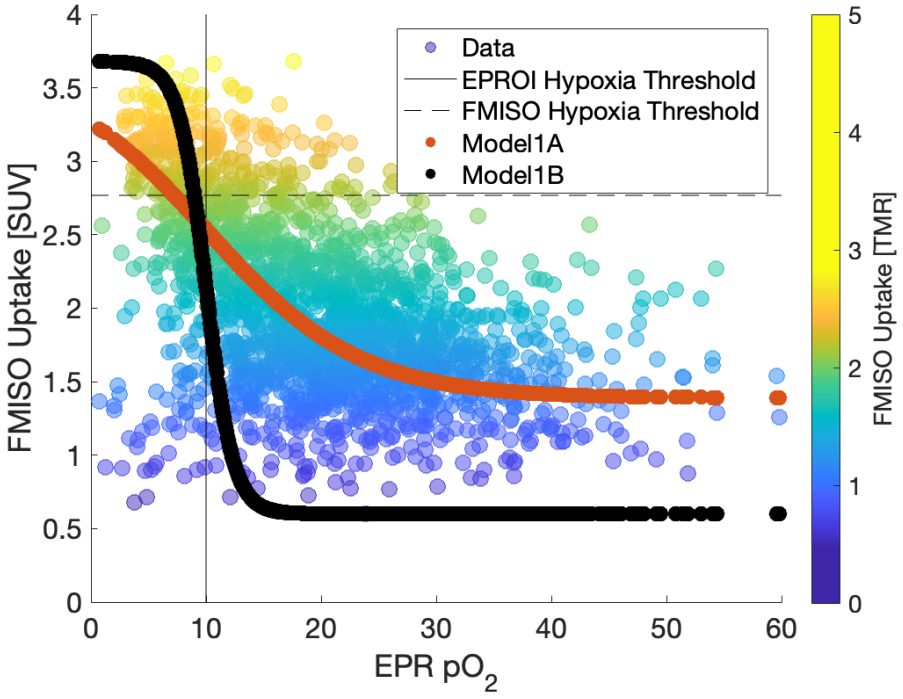

Figure 6.2: Comparison of different logistic function parameters from Model 1.

R would indicate where FMISO uptake was overestimated and negative values of R would indicate where FMISO uptake was underestimated.

$$\vec{R} = \overrightarrow{PET}^M - \overrightarrow{PET} \tag{6.10}$$

In the next step, optimal weighting coefficients $\vec{w}$ for DCE MRI parametric images were estimated using a least squares minimization of R in each cube around a central voxel throughout the tumor. Using Equation 6.9 to calculate $\hat{\vec{w}}$, $\mathbf{X}$ was a matrix of vectorized k_{ep} and v_e, and $\vec{y} = \vec{R}$:

$$\vec{R} = w_1 \cdot \vec{k}_{ep} + w_2 \cdot \vec{v}_e = \vec{w} \cdot \mathbf{X} \tag{6.11}$$

In MATLAB, $\hat{\vec{w}}$ was calculated for the central voxel in each 27-element cube. This created an image of optimal weighting coefficients throughout the entire tumor. Only k_{ep} and v_e were

used because features of K^{trans} were not significantly different between FMISO classifications of true positives or false negatives, as described in 5.3.2. Also, K^{trans} and k_{ep} are strongly correlated, so the use of both would be redundant.

Finally, the estimated optimal weighting coefficients were used to correct FMISO PET uptake, $\widehat{PET^M}$, by solving for $\widehat{PET^M}$ from Equation 6.11:

$$\widehat{PET^M} = PET + \hat{w_1}\vec{k}_{ep} + \hat{w_2}\vec{v}_e \tag{6.12}$$

The Dice Similarity Coefficient (DSC) and 95^{th} percentile of the Hausdorff Distance ($d_{H,95}$) were used to evaluate the similarity between PET and $EPROI$ (before correction) and $\widehat{PET^M}$ and $EPROI$ (after correction) using the optimal FMISO PET thresholds found in Chapter 4, and $pO_2 \leq 10$ mmHg for EPROI.

The mean weighting coefficients $\hat{w_1}$ and $\hat{w_2}$ were calculated for regions of FMISO uptake classifying TP, FP, TN, or FN regions of hypoxia, previously described in 5.2.3. Mean weights were calculated for each tumor type in each imaging group, where Group 1 had 8 MCa-4 tumors; Group 2 had 5 MCa-4 tumors, 14 SCC7 tumors, and 6 FSa tumors. ANOVA was used to assess whether weighting coefficients were similar or significantly different across tumor types and groups.

The estimated optimal weighting coefficients $\hat{w_1}$ and $\hat{w_2}$ were trained separately for tumors in Group 1 and Group 2. The mean $\hat{w_1}$ and $\hat{w_2}$ for each group was calculated and applied to each group data set as a test. Weighting coefficients from each group were validated by applying the mean $\hat{w_1}$ and $\hat{w_2}$ from Group 1 to Group 2, and also from Group 2 to Group 1.

Results of the DSC and $d_{H,95}$ before and after correcting FMISO uptake by weighted DCE MRI parametric images from training, test, and validation sets are shown in Figure 6.5. The two-sample t-test was used to identify significant improvement in similarity between hypoxic region overlap in FMISO PET vs EPROI before and after correction.

6.3 Results

6.3.1 Part A: Modeling FMISO Uptake with pO_2

Figure 6.3A shows violin plot distributions of the RMSD between all three models. The RMSD from Model 2 was significantly higher than for Models 1 and 3 (p=0.03). When grouping these results by tumor type, all models performed the worst (had the highest RMSD) for MCa-4 tumors, as shown in Figure 6.3B. The newly proposed logistic model (Model 1) consistently had the lowest RMSD.

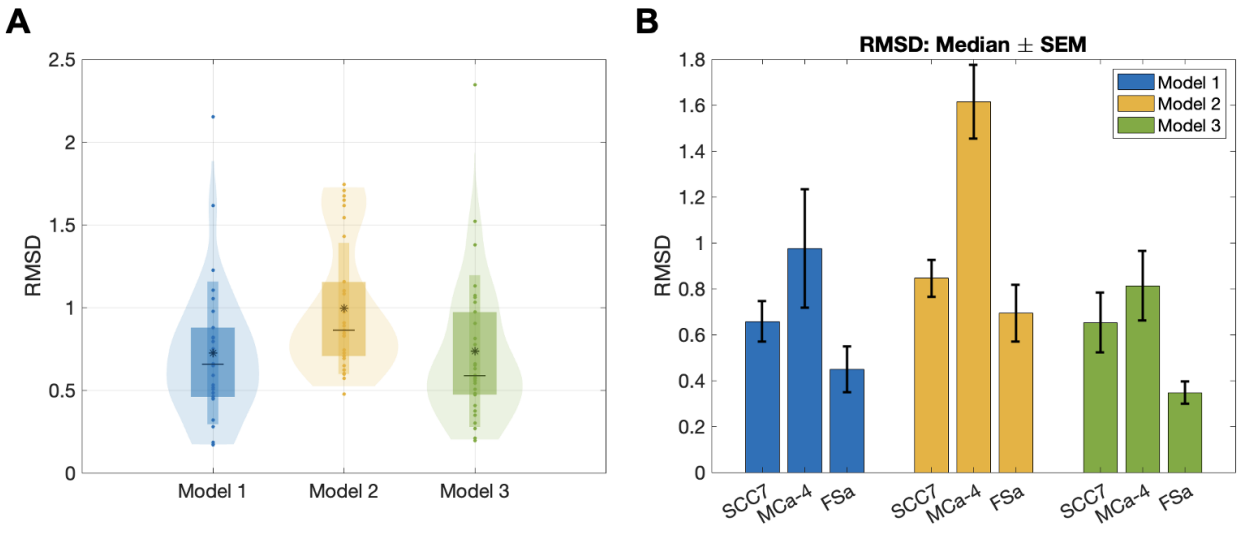

Figure 6.3: (A) Violin plots of RMSD grouped by model. (B) Bar plots of median and standard error RMSD grouped by model and sub-grouped by tumor type.

6.3.2 Part B: Correcting FMISO Uptake with DCE MRI

Table 6.1 summarizes the mean weighting coefficients for each tumor type in each group, which is visualized in Figure 6.4. In Group 2, there was no statistically significant difference (p>0.05) of weighting coefficients for k_{ep} or v_e across tumor type. Therefore, the same mean weights were used for all tumor types in Group 2 to test the effectiveness of using a single weighting coefficient per classification region.

In Group 2 for TN, FP, FN, and TN classification regions, the mean $\hat{w_1}$ was 0.123, 0.378, -0.279, and -0.129; the mean $\hat{w_2}$ was 0.350, 0.576, -0.303, and -0.061. Between Group 1 and Group 2, the only significant difference between mean weighting coefficients was in the false positive (FP) classification region for $\hat{w_1}$, which was significantly lower ($p<0.01$) in Group 1 (0.049) than Group 2 (0.378).

Before the correction algorithm was applied to all tumors, the mean ± standard deviation of the DSC and $d_{H,95}$ were used as a baseline for similarity between hypoxic tumor regions defined by EPROI vs FMISO PET without correction. In Group 1 the DSC was 0.42 ± 0.21 and $d_{H,95}$ was 5.5 ± 1.6 mm. For Group 2 the DSC was 0.44 ± 0.15 and the $d_{H,95}$ was 3.4 ± 1.0 mm. Table 6.2 summarizes the DSC and $d_{H,95}$ after correction for training, test, and validation data sets from Group 1 and Group 2.

Interestingly, applying the mean weighting coefficients from Group 1 to Group 2 as validation resulted in a significant improvement in similarity ($p<0.001$), but applying the mean weighting coefficients from Group 2 to Group 1 did not, even though only one weighting coefficient was significantly different between the two groups. Figure 6.5 shows a scatter plot distribution of the DSC and $d_{H,95}$ before (blue circles) and after (red diamonds) correction for training, testing, and validation. Figure 6.6 shows an example slice of a tumor's EPROI with ground truth hypoxia, the uncorrected PET, and corrected $\widehat{PET^M}$ images from a validation set.

Table 6.1: Mean weighting coefficients for regions classified as True Negative (TN), False Negative (FN), False Positive (FP), and True Positive (TP) hypoxic regions by FMISO uptake. Asterisk identifies a significant difference ($p<0.05$) in $\hat{w}$ compared to other tumor types within classification groups.

		TN	FP	FN	TN
$\hat{w_1}$ (k_{ep})	MCa-4 (G1)	0.036	0.049*	-0.338	-0.282
	MCa-4 (G2)	0.081	0.446	-0.542	-0.219
	SCC7 (G2)	0.163	0.405	-0.138	-0.046
	FSa (G2)	0.065	0.259	-0.390	-0.247
$\hat{w_2}$ (v_e)	MCa-4 (G1)	0.219	0.792	-0.479	-0.142
	MCa-4 (G2)	0.325	0.575	-0.485	-0.087
	SCC7 (G2)	0.393	0.614	-0.245	-0.015
	FSa (G2)	0.272	0.488	-0.287	-0.145

Table 6.2: Dice Similarity Coefficient (DSC) and Hausdorff Distance ($d_{H,95}$) before and after correcting FMISO PET images with weighted DCE MRI parametric images for training, test, and validation datasets from Group 1 and Group 2. Bold text indicates that after correction, the DSC or $d_{H,95}$ were significantly improved ($p<0.01$).

		DSC		$d_{H,95}$	
		Before	After	Before	After
Group 1	Train	0.42 ± 0.21	0.57 ± 0.27	5.5 ± 1.6	4.0 ± 2.2
	Test		0.53 ± 0.15		4.5 ± 1.7
	Validate	0.44 ± 0.15	**0.71 ± 0.15**	3.4 ± 1.0	**2.5 ± 0.74**
Group 2	Train	0.44 ± 0.15	**0.78 ± 0.12**	3.4 ± 1.0	**2.1 ± 0.54**
	Test		**0.67 ± 0.16**		**2.7 ± 0.81**
	Validate	0.42 ± 0.21	0.48 ± 0.21	5.5 ± 1.6	4.9 ± 1.7

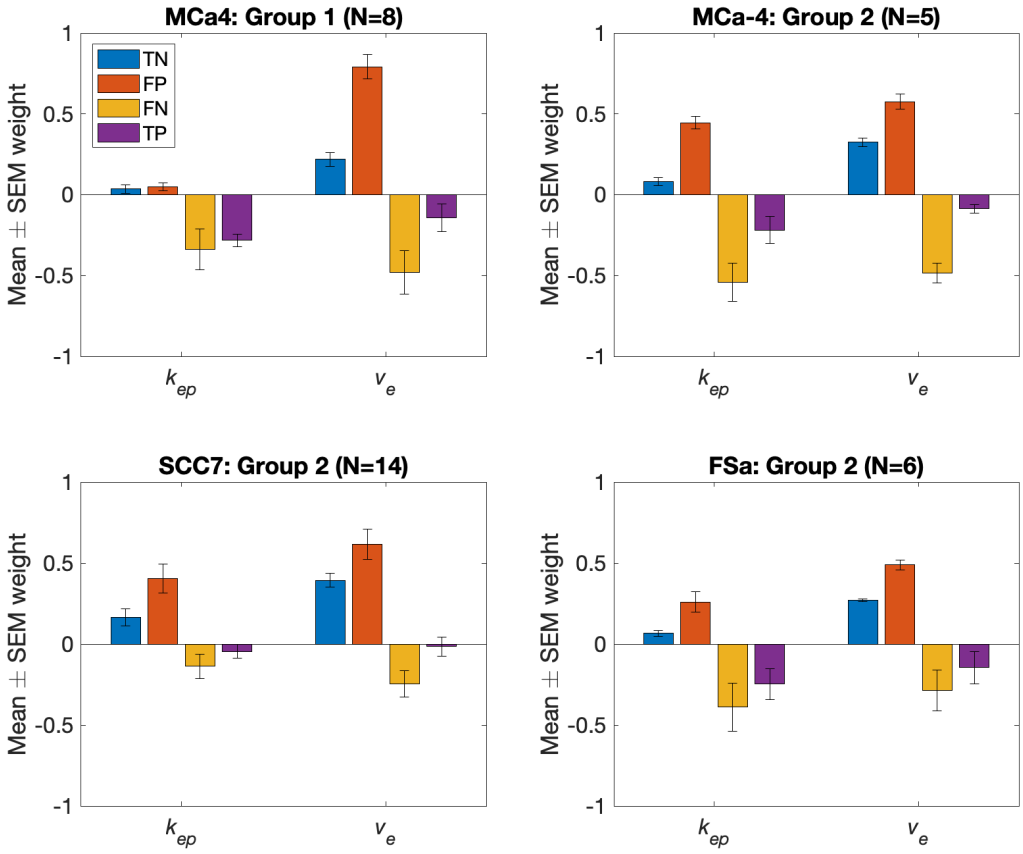

Figure 6.4: Mean and standard deviation of weighting coefficients of k_{ep} and v_e across tumor type and group.

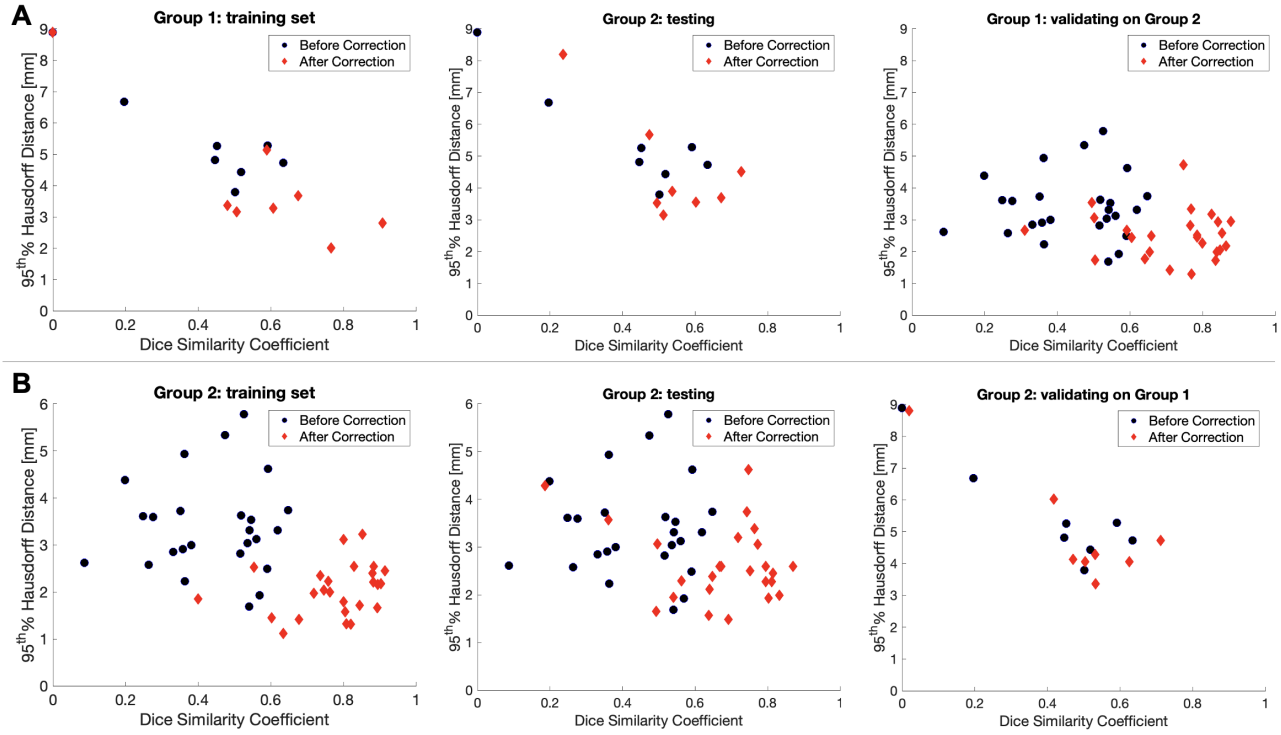

Figure 6.5: DSC and $\mathrm{d}_{H,95}$ before and after correcting FMISO PET with optimally weighted DCE MRI parametric images from (A) Group 1 and (B) Group 2 on training, test, and validation sets.

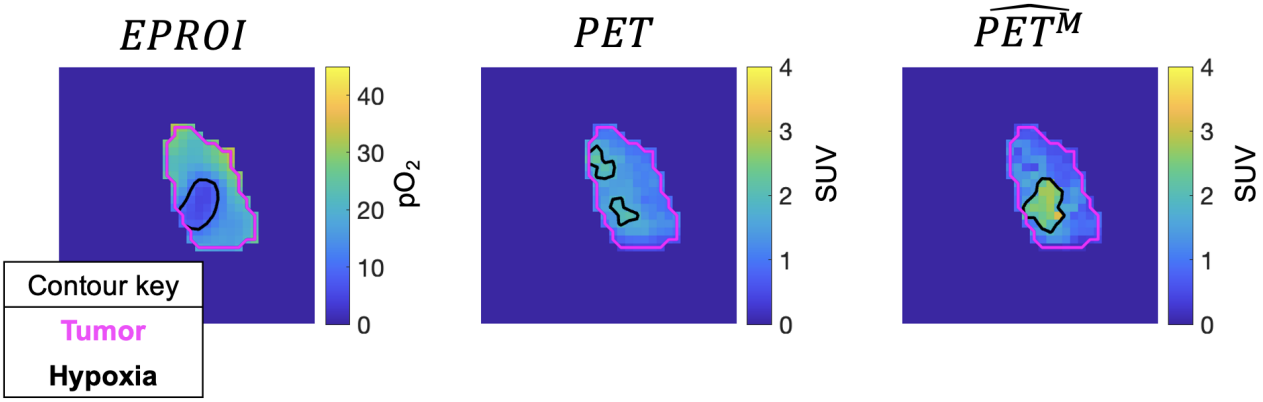

Figure 6.6: Axial slice of an SCC7 tumor's images in EPROI, PET, and $\widehat{PET^M}$ images. The tumor outline is in magenta, and hypoxia outline is in black.

6.4 Discussion

This preclinical study used EPROI as the reference standard for measuring pO_2 and hypoxia in comparison with their measurements of FMISO uptake. EPROI serves as a reference standard of true hypoxia in relation to clinically applicable FMISO PET and DCE MRI. Published studies that developed a model of FMISO uptake with pO_2 did not have the use of a hybrid PET/EPROI machine, which avoids issues of moving the mouse between modalities and cyclical hypoxia. Therefore, we can validate FMISO uptake to absolute pO_2 voxel-by-voxel by using two modalities with similar intrinsic resolutions.

Using our data in three tumor types from Group 2, the FMISO uptake model by Lindblom *et al.* shown in Equation 6.3 [79] overestimated FMISO uptake for low pO_2, especially in tumors with low hypoxic fractions. A study by Rasey *et al.* demonstrated that FMISO can have lower uptake in deeply hypoxic cells [105], and using logistic function in Model 1 attempts to make the corresponding correction without over-correcting like in Models 2 and 3. Therefore, it may be more appropriate to use Model 1 than Model 3 even though they both have similar RMSD distributions.

While Model 1 had a lower RMSD for predicting FMISO uptake with pO_2 from EPROI, the original parameters with a gentler slope were not appropriate for the least squares correction algorithm, which required a more binary representation of truly hypoxic versus normoxic voxels. Using the parameters with $\gamma = 0.15$ resulted in a lower similarity than using parameters with $\gamma = 0.85$ (see Figure 6.2).

Linear least squares is a method to map FMISO PET and DCE MRI images (k_{ep} and v_e) to corrected FMISO PET images, validated by pO_2 EPROI. This was achieved by calculating optimal weighting coefficients applied to k_{ep} and v_e in 27-element cubes around every voxel in the whole tumor, which provided three-dimensional information of surrounding voxels. This method was used because one weighting coefficient for the entire tumor, rather than tumor subregions, did not result in improved similarity in testing sets. This is expected due

to the heterogeneity of the tumor microenvironment.

The average weighting coefficients in regions classified as TN, FP, FN, and TP hypoxia by FMISO uptake were similar across all three tumor types — FSa, MCa-4, and SCC7 — in Group 2. The average of weighting coefficients in MCa-4 tumors from Group 1 was also similar to those in Group 1, except the mean $\hat{w_1}$ in was significantly lower in FP regions. For this reason, the mean weights obtained from training in Group 1 were applied to Group 2 as validation, and vice versa, to understand how these different weighting coefficients affected similarity between hypoxic tumor subregions defined by EPROI vs corrected FMISO PET ($\widehat{PET^M}$).

Applying the mean $\hat{w_1}$ and $\hat{w_2}$ weighting coefficients from Group 1 (N=8) to Group 2 (N=25) resulted in significantly improved DSC and $d_{H,95}$ in Group 2 ($p<0.001$). Only one tumor did not have both an increased DSC and decreased $d_{H,95}$ after correction. However, weighting coefficients from Group 2 applied to Group 1 did not result in *significant* improvement ($p>0.5$) even though all tumors had improved DSC and/or $d_{H,95}$.

Based on these results, it seems like over-correcting for FP regions by increasing the weight of k_{ep} in those regions has a worse outcome on similarity than under-correcting for FP regions by k_{ep}. In the context of this study, it is more important to correct for FN regions, and the mean weighting coefficients for FN regions were similar between the two groups.

For treatment planning, missing a hypoxic tumor region (FN) for a boost dose delivery would likely result in worse treatment outcome than delivering a boost dose delivery to a FP region. Therefore it is important to prioritize correcting FN regions than FP regions.

While the significant improvement of hypoxic region overlap between EPROI and $\widehat{PET^M}$ is promising, there is still the need to develop a classification algorithm that accurately identifies TN, FP, FN, and TP hypoxia regions based on only FMISO PET and DCE MRI. However, in the presented work, we show that by identifying those regions, the same weight-

ing coefficients can be applied across tumor types to make these corrections.

6.5 Conclusions

In this chapter, we have shown the utility of a hybrid PET/EPR machine to test and improve models of pO_2 from hypoxia radiotracers, such as FMISO, in several tumor types. We have also developed a correction algorithm that can more accurately locate hypoxia in FMISO PET images by using pO_2 from EPROI as the reference standard in combination with weighted DCE MRI parametric images. The end goal, however, would be to treat tumors with hypoxic boost treatments as described in Chapter 3 with EPROI, to see if there is an improvement in local tumor control with the corrected FMISO images. This would bring the field one step closer in improving tumor hypoxia location with PET/MRI.

CHAPTER 7

CONCLUSIONS AND FUTURE DIRECTIONS

7.1 Summary of Presented Work

The presented work had four specific objectives reproduced in three tumor murine models: SCC7 squamous cell carcinomas, FSa fibrosarcomas, and MCa-4 mammary adenocarcinoams. The first objective was to demonstrate improved local tumor control using oxygen image-guided radiation therapy with EPROI. The second was to identify the optimal threshold to define hypoxia with FMISO PET. The third was to compare relationships between tumor vasculature and hypoxia across tumor types with DCE MRI, FMISO PET/EPROI, and histological imaging. The fourth was to develop a model and correction algorithm to improve the accuracy of tumor hypoxia location by combining FMISO PET with DCE MRI.

At a high level, the focus of this dissertation was comparing modalities of directly and indirectly imaging tumor hypoxia, both *in vivo* and *ex vivo*. EPROI directly measures absolute pO_2, and there is a clearly-established threshold in defining hypoxia as $pO_2 \leq 10$ mmHg. Across three tumor types, EPROI was shown to be a useful tool for dose escalation with oxygen image-guided radiation therapy. FMISO PET measures the intracellular accumulation of the hypoxia radiotracer, for which we identified the optimal threshold (which is dependent on tumor type). DCE MRI parametric images include K^{trans}, the influx rate of a contrast agent and a measure of vascular perfusion and permeability; v_e, the fractional extracellular-extravascular space; and k_{ep}, the reflux rate of the contrast agent. Relationships between DCE MRI parametric images with oxygen were dependent on tumor type and hypoxic fraction.

In comparing features of DCE MRI parametric images to FMISO uptake correctly classifying hypoxia as true positive (TP) or misclassifying hypoxia as a false negative (FN) when it was hypoxic, we observed that the mean k_{ep} was significantly higher in FN regions than

TP regions (p=0.03), though not as high as in true negative (TN) regions. This implies that the reflux of the tracer from tumor back into the blood stream leads to missed hypoxia identification, not necessarily that the tracer cannot reach poorly-perfused regions. This also implies that it is difficult with only first-order features to distinguish between TP and FN hypoxic regions, and further work is required to apply more sophisticated methods to identify features in FN regions only with FMISO PET and DCE MRI, and to correct those regions.

The hope for this dissertation is to set the stage for experiments that deliver a boost dose to hypoxic tumor subregions as defined by a combination of FMISO PET and DCE MRI — both clinically available modalities. This will emulate the oxygen image-guided radiation therapy experiments outlined in Chapter 3 with EPROI, which is not a widely-available or FDA-approved modality.

7.2 Conclusions

The end goal of this work is to test any and all approaches in radiotherapy boost dose studies as those described in Chapter 3 on oxygen image-guided radiation therapy with EPROI. EPROI is capable of accurately measuring and imaging absolute pO_2 *in vivo* and defining hypoxic tumor volumes with a clear 10 mmHg threshold. In three tumor models, EPROI was used for oxygen image-guided radiation therapy, showing a significantly improved local tumor control when delivering a boost dose to hypoxic tumor subregions compared to normoxic tumor subregions.

A notable difference in the study design of this preclinical work compared to clinical dose escalation studies is the low dose delivered to oxygenated tumor regions. In our preclinical study, a low dose at 15-20% the tumor control dose was delivered to the whole tumor (22.5, 48, and 49.9 Gy for FSa, SCC7, and MCa-4 tumors) followed by a 95-99% tumor control dose boost. In clinical studies, a high dose was delivered to a whole tumor followed by a

boost dose. For example, in Vera *et al.* 66 Gy was delivered to the whole tumor for non-small cell lung carcinomas, followed by a 4-13 Gy boost dose (depending on the tumor site and organs at risk) [10]. In Welz *et al.* 70 Gy was delivered to the whole tumor for head and neck cancers, followed by a 7 Gy boost [19]. Other notable differences in the preclinical study design was the single-fraction delivery regimen compared to multi-fraction regimens in the clinic, and the fact that most clinical treatments involve a combination of radiation and chemotherapy while our preclinical studies only involved radiation.

The promising results we showed in Chapter 3 even when delivering such a low dose to the oxygenated tumor in one fraction implies two things in three tumor types. The first implication is that patients likely do not need such a high radiation dose if their tumors are not hypoxic. This has been confirmed in a study by Riaz *et al.*, using FMISO PET to identify patients without hypoxic tumors, de-escalating the dose from 70 Gy to 30 Gy, and observing ∼94% loco-regional control and overall survival over two years [77]. The second implication is that if tumors are hypoxic, but we have the ability to accurately image tumor hypoxia, it is reasonable to still deliver a low dose to the whole tumor with a high boost dose to just the hypoxic regions, thereby sparing the surrounding organs at risk.

One caveat is that groups of tumors with a median hypoxic fraction above 0.22 may not be suitable for hypoxic boost doses, as observed in SCC7 tumors. This may be caused by biological processes outside of radiation-resistant hypoxic tumor cells induced by HIF-1α, which leads to higher probabilities of angiogenesis and metastasis. However, it is promising to observe enhanced local tumor control by at least a factor of two in three tumor types when delivering a low 20% tumor control dose to the whole tumor and an added 13 Gy boost dose to hypoxic tumor subregions.

Despite these promising results, the major limitation of the study is the lack of EPR imagers available in hospitals for human pO_2 imaging. Therefore, the accuracy of FMISO PET imaging in locating tumor hypoxia *in vivo* is imperative. A major challenge with

implementing FMISO PET in the clinic is the lack of an established threshold to define hypoxia. In this work, using EPROI to define ground truth hypoxia, the optimal thresholds were found to be SUV $\geq 1.4\times$SUV$_{mean}$ for SCC7 tumors, TMR ≥ 1.4 for FSa tumors, and SUV ≥ 1.8 for MCa-4 tumors.

An incredible advantage we had in comparing FMISO PET uptake to pO_2 from EPROI was the development of a hybrid PET/EPR imager used in Group 2 imaging protocol (4.2.5). It ensured identical physiological conditions of the mouse during imaging in both modalities, and allowed us to overcome logistical challenges like transporting the mouse between machines on opposite sides of the building. It also gave the confirmation that poor similarity between hypoxic volumes defined by FMISO and EPROI in MCa-4 tumors was not only caused by a time difference between PET/EPR imaging as we saw in Group 1 imaging protocol (4.2.4).

For MCa-4 tumors, on average there was a 68% similarity between PET- and EPR-defined hypoxic volumes. For SCC7 and FSa tumors, there was a 73% similarity —an improvement, but with room for even more improvement. The benefits of accurately locating hypoxia for dose escalation protocols would be immeasurable for a patient. If a hypoxic volume were defined larger than necessary in a tumor surrounded by sensitive organs (such as a head and neck cancer), the patient would be burdened with a higher dose exposure than necessary. On the other hand, if part of a hypoxic volume were missed, there would be a higher chance of tumor recurrence.

For this reason, the utility of DCE MRI parametric images were explored to see if the accuracy of FMISO PET could be improved. One observation was that MCa-4 tumors had the weakest correlation strengths between FMISO PET with EPR pO_2, compared to SCC7 and FSa tumors. We also observed that features in k_{ep} could be used to distinguish between FMISO PET's hypoxia classification of false positive or false negative. However, differences between true positive and true negative hypoxia classifications were more statistically signif-

icant. Ongoing work includes chemical exchange saturation transfer (CEST) MRI to image pH and see whether acidity in the tumor affects FMISO uptake in hypoxic tumor cells.

We developed a correction algorithm to use least-squares to find optimal weighting coefficients to correct FMISO PET with k_{ep} and v_e. With the initial correction-learning method, we have shown the potential for developing an algorithm that can more accurately locate hypoxia in FMISO PET images by using pO_2 from EPROI as the reference standard in combination with DCE MRI. However, at this time we are still in the process of collecting data for MCa-4 tumors, for which FMISO PET is the least accurate. Work for this is ongoing and discussed in the next section.

7.3 Proposed Future Directions

There are several directions one could take with this research, especially to better emulate clinical study design with these preclinical models. Using EPROI for oxygen image-guided radiation therapy, this work can be repeated with a fractionated dose regimen rather than in a single dose, more similar to clinical treatments. This could determine whether local tumor control with fractionated treatments would increase compared to a single fraction with hypoxic boosts. However, it would be challenging to put mice under anesthesia several times a week to do MRI/EPROI/CT to plan each treatment, both for their well-being and logistically.

Another way to better emulate modern treatment regimens is to do intensity-modulated radiation therapy (IMRT) in three or five angles with 3D-printed compensators, rather than two opposing beams [74]. Future study designs could also combine radiation therapy with chemotherapy to determine whether their combination with hypoxic boost treatments would significantly improve local tumor control.

With FMISO PET, future work could include pixel-wise pharmacokinetic modeling of the MCa-4 dynamic PET data from the Group 1 imaging protocol. It would be interesting

to see if any transfer constants from the two-tissue compartment model would correlate with EPROI and/or DCE MRI parametric images K^{trans}, v_e, or k_{ep}. Dynamic data was not acquired with the current prototype of the hybrid PET/EPR machine because the axial field of view of the PET machine was too short. However, a newer iteration of the PET insert is nearly complete and should have a long enough axial field of view to be able to image the heart and tumor-bearing leg simultaneously. This would allow us to use the left ventricle of the ROI as the model for the blood/plasma compartment.

Another exciting project is developing an *in vivo* reconstruction method of the time decay of positronium, which correlates with pO_2 and can theoretically be done with any radiotracer [108]. The hybrid PET/EPR machine can be used for PET imaging while simultaneously validating its estimation of pO_2. This novel and exciting work has yet to be accomplished *in vivo*.

Of course, the entire project can be repeated with a different radiolabeled hypoxia marker, such as ^{18}F-EF5, ^{18}F-FAZA, ^{64}Cu-ATSM, or any of the twelve PET radiopharmaceuticals with the potential to target hypoxia discussed in Lopci *et al.* [23]. It is possible that another tracer is better correlated with EPROI pO_2 than FMISO.

The original study design included chemical exchange saturation transfer (CEST) MRI, which can be used to image pH. Few studies have imaged both CEST MRI with FMISO PET, though it has been done [109]. In the context of this work, it would be useful to see if features of pH imaged by CEST MRI had any relationship with FMISO's false positive or false negative classifications of hypoxia. This would allow us to better understand the effects of pH on intracellular FMISO uptake.

Finally, unstained histological slices have been left intentionally for future work in all three tumor types. Additional IHC staining could be done with the vascular endothelial growth factor (VEGF), a signalling protein that promotes the growth of new blood vessels. Carbonic anhydrase IX (CAIX) is a transmembrane protein that is upregulated in hypoxic

environments, and could be compared to HIF-1α expression and *in vivo* hypoxia shown in EPROI and/or FMISO [110]. This would be useful to compare whether HIF-1α or CAIX are better markers of regional hypoxia in comparison to *in vivo* EPROI.

Of course, further work is required to develop a more robust machine learning algorithm with a testing, training, and validation set of data across all tumor types. At this time, image data is continuously being acquired to increase the number of tumors to improve the training set across all tumor types, and in future studies, a new PET insert with higher sensitivity and a longer axial field of view will be used for PET/EPROI imaging.

Ideally, this work will be an important stepping stone towards improving radiation therapy outcome by more accurately targeting hypoxic tumor regions for dose escalation.

BIBLIOGRAPHY

1. Vaupel, P. & Höckel, M. Tumor hypoxia: Definitions and current clinical, biologic, and molecular aspects. *J Natl Cancer Inst.* **93,** 266–276 (2001).

2. Walsh, P. *et al.* The clinical importance of assessing tumor hypoxia: relationship of tumor hypoxia to prognosis and therapeutic opportunities. *Antioxid Redox Signal.* **21,** 1516–1556 (2014).

3. Höckel, M. *et al.* Intratumoral pO_2 predicts survival in advanced cancer of the uterine cervix. *Radiother Oncol.* **26,** 45–50 (1993).

4. Fyles, A. *et al.* Tumor hypoxia has independent predictor impact only in patients with node-negative cervix cancer. *J Clin Oncol.* **20,** 680–687 (2002).

5. Knocke, T. H., Weitmann, H. D., Feldmann, H. J., Selzer, E. & Pötter, R. Intratumoral pO_2-measurements as predictive assay in the treatment of carcinoma of the uterine cervix. *Radiother Oncol.* **53,** 99–104 (1999).

6. Lyng, H., Sundfør, K., Tropé, C. & Rofstad, E. K. Disease control of uterine cervical cancer: relationships to tumor oxygen tension, vascular density, cell density, and frequency of mitosis and apoptosis measured before treatment and during radiotherapy. *Clin Cancer Res.* **6,** 1104–1112 (2000).

7. Evans, S. M. & Koch, C. J. Prognostic significance of tumor oxygenation in humans. *Cancer Lett.* **195,** 1–16 (2003).

8. Nordsmark, M. *et al.* Prognostic value of tumor oxygenation in 397 head and neck tumors after primary radiation therapy. An international multi-center study. *Radiother Oncol.* **77,** 18–24 (2005).

9. Terris, D. J. Head and neck cancer: the importance of oxygen. *Laryngoscope.* **110,** 697–707 (2000).

10. Vera, P. *et al.* Phase II Study of a Radiotherapy Total Dose Increase in Hypoxic Lesions Identified by 18F-Misonidazole PET/CT in Patients with Non-Small Cell Lung Carcinoma (RTEP5 Study). *J Nucl Med.* **58,** 1045–1053 (2017).

11. Le, Q. T. *et al.* An evaluation of tumor oxygenation and gene expression in patients with early stage non-small cell lung cancers. *Clin Cancer Res.* **12,** 1507–1514 (2006).

12. Nordsmark, M. *et al.* Hypoxia in human soft tissue sarcomas: adverse impact on survival and no association with p53 mutations. *Br J Cancer.* **84,** 1070–1075 (2001).

13. Brizel, D. M. *et al.* Tumor oxygenation predicts for the likelihood of distant metastases in human soft tissue sarcoma. *Cancer Res.* **56,** 941–943 (1996).

14. Thomlinson, R. H. & Gray, L. H. The histological structure of some human lung cancers and the possible implications for radiotherapy. *Br J Radiol.* **9,** 539–563 (1955).

15. Crabtree, H. G. & Cramer, W. The action of radium on cancer cells II - Some factors determining the susceptibility of cancer cells to radium. *Proceedings of the Royal Society of London Series B-Containing Papers of a Biological Character.* **113,** 238–250 (1933).

16. Schwarz, G. Uber Desensibilisierung gegen Rontgen- und Radiumstrahlen. *Munchner Medizinische Wochenschrift.* **56,** 1217–1218 (1909).

17. Ferini, G. *et al.* Lattice or Oxygen-Guided Radiotherapy: What If They Converge? Possible Future Directions in the Era of Immunotherapy. *Cancers.* **13,** 3290 (2021).

18. Even, A. J. *et al.* PET-based dose painting in non-small cell lung cancer: Comparing uniform dose escalation with boosting hypoxic and metabolically active sub-volumes. *Radiother Oncol.* **116,** 281–286 (2015).

19. Welz, S. *et al.* Dose escalation to hypoxic subvolumes in head and neck cancer: A randomized phase II study using dynamic [^{18}F]FMISO PET/CT. *Radiother Oncol.* **171,** 30–36 (2022).

20. Wilson, D. F., Vinogradov, S., Lo, L. W. & Huang, L. Oxygen dependent quenching of phosphorescence: a status report. *Adv Exp Med Biol.* **388,** 101–107 (1996).

21. Vaupel, P., Höckel, M. & Mayer, A. Detection and characterization of tumor hypoxia using pO_2 histography. *Antioxid Redox Signal.* **9,** 1221–1235 (2007).

22. Vaupel, P. & Mayer, A. The clinical importance of assessing tumor hypoxia: relationship of tumor hypoxia to prognosis and therapeutic opportunities. *Antioxid Redox Signal.* **22,** 878–880 (2015).

23. Lopci, E. *et al.* PET radiopharmaceuticals for imaging of tumor hypoxia: a review of the evidence. *Am J Nucl Med Mol Imaging.* **4,** 365–384 (2014).

24. Kallinowski, F., Zander, R., Hoeckel, M. & Vaupel, P. Tumor tissue oxygenation as evaluated by computerized-pO_2-histography. *Int J Radiat Oncol Biol Phys.* **19,** 953–961 (1990).

25. Brizel, D. M., Sibley, G. S., Prosnitz, L. R., Scher, R. L. & Dewhirst, M. W. Tumor hypoxia adversely affects the prognosis of carcinoma of the head and neck. *Int J Radiat Oncol Biol Phys.* **38,** 285–289 (1997).

26. Nordsmark, M., Overgaard, M. & Overgaard, J. Pretreatment oxygenation predicts radiation response in advanced squamous cell carcinoma of the head and neck. *Radiother Oncol.* **41,** 31–39 (1996).

27. Panych, L. P. & Madore, B. The physics of MRI safety. *J Magn Reson Imaging.* **47,** 28–43 (2018).

28. Pooley, R. Fundamental physics of MR imaging. *Radiographics.* **25,** 1087–1099 (2005).

29. Currie, S., Hoggard, N., Craven, I. J., Hadjivassiliou, M. & Wilkinson, I. D. Understanding MRI: basic MR physics for physicians. *Postgrad Med J.* **89,** 209–223 (2013).

30. Bottomley, P. A. & Andrew, E. R. RF magnetic field penetration, phase shift and power dissipation in biological tissue: implications for NMR imaging. *Phys Med Biol.* **23,** 630–643 (1978).

31. Lauterbur, P. C. Image Formation by Induced Local Interactions - Examples Employing Nuclear Magnetic-Resonance. *Nature.* **242,** 190–191 (1973).

32. Gallez, B., Baudelet, C. & Jordan, B. F. Assessment of tumor oxygenation by electron paramagnetic resonance: principles and applications. *NMR Biomed* **17,** 240–262 (2004).

33. Epel, B. & Halpern, H. Electron paramagnetic resonance oxygen imaging in vivo. *Electron Paramagn Reson.* **23,** 180–208 (2013).

34. Biller, J. R. *et al.* Relaxation times and line widths of isotopically-substituted nitroxides in aqueous solution at X-band. *J Magn Reson.* **212,** 370–377 (2011).

35. Gertsenshteyn, I., Giurcanu, M., Vaupel, P. & Halpern, H. Biological validation of electron paramagnetic resonance (EPR) image oxygen thresholds in tissue. *J Physiol.* **599,** 1759–1767 (2021).

36. Matsumoto, K. *et al.* Pharmacokinetics of a triarylmethyl-type paramagnetic spin probe used in EPR oximetry. *Magn Reson Med.* **52,** 885–892 (2004).

37. Epel, B., Bowman, M. K., Mailer, C. & Halpern, H. J. Absolute oxygen R1 imaging in vivo with pulse electron paramagnetic resonance. *Magn Reson Med.* **72,** 362–368 (2014).

38. Bobko, A. A. *et al.* In vivo Extracellular pH Monitoring in Tumor Tissues of PyMT mice: Effect of GM-CSF Treatment. *Free Radic Biol Med.* **47,** 1827–1836 (2009).

39. Epel, B. *et al.* Oxygen-guided radiation therapy. *Int J Radiat Oncol Biol Phys.,* 977–984 (2019).

40. Kuzhelev, A. A. *et al.* Room-Temperature Electron Spin Relaxation of Triarylmethyl Radicals at the X- and Q-Bands. *J Phys Chem B.* **119,** 13630–13640 (2015).

41. Epel, B. *et al.* Electron paramagnetic resonance oxygen imaging of a rabbit tumor using localized spin probe delivery. *Med Phys.* **37,** 2553–2559 (2010).

42. Maeda, H., Wu, J., Sawa, T., Matsumura, Y. & Hori, K. Tumor vascular permeability and the EPR effect in macromolecular therapeutics: a review. *J Control Release.* **65,** 271–84 (2000).

43. Bourg, J. *et al.* Radiofrequency FT EPR Spectroscopy and Imaging. *J Magn Reson B.* **102,** 112–125 (1993).

44. Williams, B. B. *et al.* Imaging spin probe distribution in the tumor of a living mouse with 250 MHz EPR: Correlation with BOLD MRI. *Magn Reson Med.* **47,** 634–638 (2002).

45. Roschmann, P. Radiofrequency penetration and absorption in the human body: limitations to high-field whole-body nuclear magnetic resonance imaging. *Med Phys.* **14,** 922–931 (1987).

46. Halpern, H. J. *et al.* Oxymetry Deep in Tissues with Low-Frequency Electron-Paramagnetic-Resonance. *Proceedings of the National Academy of Sciences of the United States of America* **91,** 13047–13051 (1994).

47. Rinard, G. A., Quine, R. W., Eaton, S. S. & Eaton, G. R. Frequency dependence of EPR signal intensity, 248 MHz to 1.4 GHz. *J Magn Reson.* **154,** 80–84 (2002).

48. Cherry, S. R., Sorenson, J. A. & Phelps, M. E. in *Phys Nucl Med.* (ed Saunders) 4th ed., 341 (2012).

49. Moses, W. W. Fundamental limits of spatial resolution in PET. *Nuclear Inst and Methods in Physics Research.* **648,** S236–S240 (2011).

50. Patridge, M., Spinelli, A., Ryder, W. & Hindorf, C. The effect of + energy on performance of a small animal PET camera. *Nucl Instrum Methods Phys Res A.* **568,** 933–936 (2006).

51. Grierson, J. R., Link, J. M., Mathis, C. A., Rasey, J. S. & Krohn, K. A. A radiosynthesis of fluorine-18 fluoromisonidazole. *J Nucl Med.* **30,** 343–50 (1989).

52. Franko, A. J. Misonidazole and other hypoxia markers: Metabolism and applications. *Int J Radiat Oncol Biol Phys.* **12,** 1195–1202 (1986).

53. Xu, Z., Li, X.-F., Zou, H., Sun, X. & SHen, B. 18F-Fluoromisonidazole in tumor hypoxia imaging. *Oncotarget.* **8,** 94969–94979 (2017).

54. Masaki, Y. *et al.* FMISO accumulation in tumor is dependent on glutathione conjugation capacity in addition to hypoxic state. *Annals of Nucl Med.* **31,** 596–604 (2017).

55. Segard, T. *et al.* Detection of hypoxia with 18F-fluoromisonidazole (18F-FMISO) PET/CT in suspected or proven pancreatic cancer. *Clin Nucl Med.* **38,** 1–6 (2013).

56. Roels, S. *et al.* Biological image-guided radiotherapy in rectal cancer: is there a role for FMISO or FLT, next to FDG? *Acta Oncol.* **47,** 1237–1248 (2008).

57. O'Connor, J. P. B., Jackson, A., Parker, G. J. M., Roberts, C. & Jayson, G. C. Dynamic contrast-enhanced MRI in clinical trials of antivascular therapies. *Nat Rev Clin Oncol.* **9,** 167–177. ISSN: 1759-4782 (2012).

58. Hillestad, T. *et al.* MRI Distinguishes Tumor Hypoxia Levels of Different Prognostic and Biological Significance in Cervical Cancer. *Cancer Res.* **80,** 3993–4003 (2020).

59. Ellingsen, C. *et al.* Assessment of hypoxia in human cervical carcinoma xenografts by dynamic contrast-enhanced magnetic resonance imaging. *Int J Radiat Oncol Biol Phys.* **73,** 838–845 (2009).

60. Tofts, P. *et al.* Estimating kinetic parameters from dynamic contrast-enhanced T1-weighted MRI of a diffusable tracer: Standardized quantities and symbols. *J Magn Reson Imaging.* **10,** 223–232 (1999).

61. Leach, M. O. *et al.* The assessment of antiangiogenic and antivascular therapies in early-stage clinical trials using magnetic resonance imaging: issues and recommendations. *Br J Cancer.* **92,** 1599–1610 (2005).

62. Henk, J. M., Kunkler, P. B. & Smith, C. W. Radiotherapy and hyperbaric oxygen in head and neck cancer. Final report of first controlled clinical trial. *Lancet.* **2,** 101–103 (1977).

63. Adams, G. E. Hypoxic cell sensitizers for radiotherapy. *Int J Radiat Oncol Biol Phys.* **4,** 135–141 (1978).

64. Overgaard, J. Hypoxic modification of radiotherapy in squamous cell carcinoma of the head and neck–a systematic review and meta-analysis. *Radiother Oncol.* **100,** 22–32 (2011).

65. Eisenbrey, J. R. *et al.* Sensitization of Hypoxic Tumors to Radiation Therapy Using Ultrasound-Sensitive Oxygen Microbubbles. *Int J Radiat Oncol Biol Phys.* **101,** 88–96 (2018).

66. McEwan, C. *et al.* Oxygen carrying microbubbles for enhanced sonodynamic therapy of hypoxic tumours. *J of Control Release.* **203,** 51–53 (2015).

67. Swartz, H. M. *et al.* Direct and Repeated Clinical Measurements of pO_2 for Enhancing Cancer Therapy and Other Applications. *Adv Exp Med Biol.* **923,** 95–104 (2016).

68. Lee, N. *et al.* Strategy of Using Intratreatment Hypoxia Imaging to Selectively and Safely Guide Radiation Dose De-escalation Concurrent With Chemotherapy for Locoregionally Advanced Human Papillomavirus–Related Oropharyngeal Carcinoma. *Int J Radiat Oncol Biol Phys.* **96,** 9–17 (2016).

69. Koch, C. J. & Evans, S. M. Optimizing hypoxia detection and treatment strategies. *Semin Nucl Med.* **45,** 163–176 (2015).

70. Serda, M., Wu, Y. K., Barth, E. D., Halpern, H. J. & Rawal, V. H. EPR Imaging Spin Probe Trityl Radical OX063: A Method for Its Isolation from Animal Effluent, Redox Chemistry of Its Quinone Methide Oxidation Product, and in Vivo Application in a Mouse. *Chem Res Toxicol.* **29,** 2153–2156 (2016).

71. Therneau, T. Survival: A Package for Survival Analysis in R. (2020).

72. Semenza, G. L. Intratumoral Hypoxia and Mechanisms of Immune Evasion Mediated by Hypoxia-Inducible Factors. *Physiology (Bethesda).* **36,** 73–83 (2021).

73. Dewhirst, M. W., Cao, Y. & Moeller, B. Cycling hypoxia and free radicals regulate angiogenesis and radiotherapy response. *Nat Rev Cancer.* **8,** 425–437 (2008).

74. Redler, G. *et al.* Small Animal IMRT Using 3D-Printed Compensators. *Int J Radiat Oncol Biol Phys.* **110,** 551–565 (2021).

75. Fleming, I. N. *et al.* Imaging tumour hypoxia with positron emission tomography. *Br J Cancer.* **112,** 238–250 (2015).

76. Krohn, K. A., Link, J. M. & Mason, R. P. Molecular imaging of hypoxia. *J Nucl Med.* **49 Suppl 2,** 129S–48S (2008).

77. Riaz, N. *et al.* Precision Radiotherapy: Reduction in Radiation for Oropharyngeal Cancer in the 30 ROC Trial. *J Natl Cancer Inst.* **113,** 742–751 (2021).

78. Thorwarth, D. *et al.* Prospective Evaluation of a Tumor Control Probability Model Based on Dynamic (18)F-FMISO PET for Head and Neck Cancer Radiotherapy. *J Nucl Med.* **60,** 1698–1704 (2019).

79. Lindblom, E. *et al.* Defining the hypoxic target volume based on positron emission tomography for image guided radiotherapy - the influence of the choice of the reference region and conversion function. *Acta Oncol.* **56,** 819–825 (2017).

80. Chang, J. H. *et al.* Hypoxia-targeted radiotherapy dose painting for head and neck cancer using (18)F-FMISO PET: a biological modeling study. *Acta Oncol.* **52,** 1723–1729 (2013).

81. Henriques de Figueiredo, B. *et al.* Hypoxia imaging with [18F]-FMISO-PET for guided dose escalation with intensity-modulated radiotherapy in head-and-neck cancers. *Strahlenther Onkol.* **191,** 217–224 (2015).

82. Hendrickson, K. *et al.* Hypoxia imaging with [F-18] FMISO-PET in head and neck cancer: potential for guiding intensity modulated radiation therapy in overcoming hypoxia-induced treatment resistance. *Radiother Oncol.* **101,** 369–375 (2011).

83. Kim, H. *et al.* Development of a PET/EPRI combined imaging system for assessing tumor hypoxia. *J Inst.* (2021).

84. Elas, M. *et al.* Electron paramagnetic resonance oxygen image hypoxic fraction plus radiation dose strongly correlates with tumor cure in FSa fibrosarcomas. *Int J Radiat Oncol Biol Phys.* **71,** 542–549 (2008).

85. Mollet, P. *et al.* The β-CUBE, a high-end compact preclinical benchtop PET for total body imaging. *J Nucl Med.* **58(1),** 393 (2017).

86. Epel, B., Sundramoorthy, S. V., Mailer, C. & Halpern, H. J. A versatile high speed 250-MHz pulse imager for biomedical applications. *Concepts Magn Reson Part B Magn Reson Eng.* **33B,** 163–176 (2008).

87. Lim, J.-L. & Berridge, M. An efficient radiosynthesis of [18F]fluoromisonidazole. *Appl Radiat Isot.* **44,** 1085–1091 (1993).

88. Thorwarth, D., Eschmann, S. M., Paulsen, F. & Alber, M. Hypoxia dose painting by numbers: a planning study. *Int J Radiat Oncol Biol Phys.* **68,** 291–300 (2007).

89. Simoncic, U. *et al.* Comparison of DCE-MRI kinetic parameters and FMISO-PET uptake parameters in head and neck cancer patients. *Med Phys.* **44,** 2358–2368 (2017).

90. Carmona-Bozo, J. C. *et al.* Hypoxia and perfusion in breast cancer: simultaneous assessment using PET/MR imaging. *Eur Radiol.* **31,** 333–344 (2021).

91. Pinker, K. *et al.* Multiparametric [18F]Fluorodeoxyglucose/ [18F]Fluoromisonidazole Positron Emission Tomography/ Magnetic Resonance Imaging of Locally Advanced Cervical Cancer for the Non-Invasive Detection of Tumor Heterogeneity: A Pilot Study. *PLOS ONE.* **11,** e0155333 (2016).

92. Gerstner, E. R. *et al.* ACRIN 6684: Assessment of Tumor Hypoxia in Newly Diagnosed Glioblastoma Using 18F-FMISO PET and MRI. *Clin Cancer Res.* **22,** 5079–5086 (2016).

93. Jansen, J. F. *et al.* Noninvasive assessment of tumor microenvironment using dynamic contrast-enhanced magnetic resonance imaging and 18F-fluoromisonidazole positron emission tomography imaging in neck nodal metastases. *Int J Radiat Oncol Biol Phys.* **77,** 1403–1410 (2010).

94. Swartz, H. M. *et al.* How best to interpret measures of levels of oxygen in tissues to make them effective clinical tools for care of patients with cancer and other oxygen-dependent pathologies. *Physiol Rep.* **8** (2020).

95. Janssen, H. *et al.* HIF-1, pimonidazole, and iododeoxyuridine to estimate hypoxia and perfusion in human head-and-neck tumors. *Int J Radiat Oncol Biol Phys.* **54,** 1537–1549 (2002).

96. Medved, M. *et al.* Semiquantitative analysis of dynamic contrast enhanced MRI in cancer patients: Variability and changes in tumor tissue over time. *J Magn Reson Imaging.* **20,** 122–128 (2004).

97. Mustafi, D. *et al.* High-resolution magnetic resonance colonography and dynamic contrast-enhanced magnetic resonance imaging in a murine model of colitis. *Magn Reson Med.,* 922–929 (2010).

98. Kovar, D., Lewis, M. & Karczmar, G. A new method for imaging perfusion and contrast extraction fraction: Input functions derived from reference tissues. *J Magn Reson Imaging.* **8,** 1126–1134 (1998).

99. Fan, X. *et al.* New model for analysis of dynamic contrast enhanced MRI data distinguishes metastatic from nonmetastatic transplanted rodent prostate tumors. *Magn Reson Med.* **51,** 487–494 (2004).

100. Haney, C. R. *et al.* Monitoring anti-angiogenic therapy in colorectal cancer murine model using dynamic contrast-enhanced MRI: comparing pixel-by-pixel with region of interest analysis. *Technol Cancer Res Treat.* **12,** 71–78 (2013).

101. Donaldson, S. B. *et al.* Perfusion estimated with rapid dynamic contrast-enhanced magnetic resonance imaging correlates inversely with vascular endothelial growth factor expression and pimonidazole staining in head-and-neck cancer: a pilot study. *Int J Radiat Oncol Biol Phys.* **81,** 1176–1183 (2011).

102. Krock, B. L., Skuli, N. & Simon, M. C. Hypoxia-Induced Angiogenesis:Good and Evil. *Genes & Cancer.* **2,** 1117–1133 (2011).

103. Karth, J. *et al.* Coexpression of hypoxia-inducible factor 1-alpha and vascular endothelial growth factor in Wilms' tumor. *J Pediatr Surg.* **35,** 1749–1753 (2000).

104. Toma-Dasu, I. *et al.* Dose prescription and treatment planning based on FMISO-PET hypoxia. *Acta Oncologica.* **51,** 222–230 (2012).

105. Rasey, J. S. *et al.* Determining hypoxic fraction in a rat glioma by uptake of radiolabeled fluoromisonidazole. *Radiat Res.* **153,** 84–92 (2000).

106. Rasey, J. S., Koh, W.-J., Grierson, J. R., Grunbaum, Z. & Krohn, K. A. Radiolabeled fluoromisonidazole as an imaging agent for tumor hypoxia. *Int J Radiat Oncol Biol Phys.* **17,** 985–991 (1989).

107. Chapman, J. The detection and measurement of hypoxic cells in solid tumors. *Cancer.* **54** (1984).

108. Shibuya, K., Saito, H., Nishikido, F., Takahashi, M. & Yamaya, T. Oxygen sensing ability of positronium atom for tumor hypoxia imaging. *Comm Physics.* **3,** 173 (2020).

109. Autissier, R. *et al.* Simultaneous proteoglycans and hypoxia mapping of chondrosarcoma environment by frequency selective CEST MRI. *Magn Reson Med.* **86,** 1008–1018 (2021).

110. Wykoff, C. C. *et al.* Hypoxia-inducible expression of tumor-associated carbonic anhydrases. *Cancer Res.* **60,** 7075–7083 (2000).

111. Rasey, J. *et al.* Characterization of radiolabeled fluoromisonidazole as a probe for hypoxic cells. *Radiat Res.* **111,** 292–304 (1987).

112. Chen, N. T. *et al.* Highly sensitive electron paramagnetic resonance nanoradicals for quantitative intracellular tumor oxymetric images. *Int J Nanomedicine.* **14,** 2963–2971 (2019).

113. Krishna, M. C. *et al.* Tailored sinc pulses for uniform excitation and artifact-free radio frequency time-domain EPR imaging. *J Magn Reson.* **168,** 110–117 (2004).

114. Panych, L. P., Oesterle, C., Zientara, G. P. & Hennig, J. Implementation of a fast gradient-echo SVD encoding technique for dynamic imaging. *Magn Reson Med.* **35,** 554–562 (1996).

115. Sørensen, M., Horsman, M. R., Cumming, P., Munk, O. L. & Keiding, S. Effect of intratumoral heterogeneity in oxygenation status on FMISO PET, autoradiography, and electrode pO_2 measurements in murine tumors. *Int J Radiat Oncol Biol Phys.* **62,** 854–861 (2005).

LIST OF PUBLICATIONS AND PRESENTATIONS

Peer-Reviewed Publications

1. **Gertsenshteyn I**, Epel B, Ahluwalia A, Kim H, Fan X, Barth E, Zamora M, Markiewicz E, Tsai H-M, Sundramoorthy S, Leoni L, Lukens J, Bhuiyan M, Freifelder R, Kucharski A, Giurcanu M, Roman B, Karczmar G, Kao C-M, Halpern H, Chen C-T. The optimal ^{18}F-Fluoromisonidazole PET threshold to define tumor hypoxia in preclinical squamous cell carcinomas using pO_2 electron paramagnetic resonance imaging as reference truth. *European Journal of Nuclear Medicine and Molecular Imaging*, (2022).

2. **Gertsenshteyn I**, Epel B, Barth E, Leoni L, Markiewicz E, Fan X, Giurcanu M, Tsai H-M, Zamora M, Bodero D, Sundramoorthy S, Kim HJ, Freifelder R, Bhuiyan M, Kucharski A, Karczmar G, Kao C-M, Halpern H, Chen C-T. Improving Tumor Hypoxia Location in ^{18}F-Misonidazole PET with DCE-MRI Using Quantitative EPR pO_2 Images. *Radiology: Imaging Cancer*, 3:2 (2021).

3. **Gertsenshteyn I**, Giurcanu M, Vaupel P, Halpern HJ: Biologic Validation of EPR Image Oxygen Thresholds in Tissue. *Journal of Physiology*, 599(6), 1759-1767, (2021).

4. Kim H, Epel B, Sundramoorthy S, Tsai H-M, Barth E, **Gertsenshteyn I**, Halpern H, Hua Y, Xie Q, Chen C-T, Kao C-M. Development of a PET/EPRI combined imaging system for assessing tumor hypoxia. *Journal of Instrumentation* 16 P03031 (2021).

5. Redler G, Pearson E, Liu X, **Gertsenshteyn I**, Epel B, Pelizzari C, Aydogan B, Weichselbaum R, Halpern HJ, Wiersma RD: Small animal IMRT using 3D printed compensators. *International Journal of Radiation Oncology, Biology, Physics* (2020).

Proceedings Papers

1. Foy J, **Gertsenshteyn I**, Al-Hallaq H, Armato SG III, Sensakovic WF: Dependence of radiomics features on CT image acquisition and reconstruction parameters using a cadaveric liver. Proceedings of International Society for Optical Engineering (SPIE) 11314, Medical Imaging 2020: Computer-Aided Diagnosis, 113140U (16 March 2020).

Oral and Poster Presentations

Oral Presentations

1. **Gertsenshteyn I**: Multi-modal imaging of tumor hypoxia. Young Investigator Symposium for the American Association of Physicists in Medicine (AAPM) Midwest Chapter Spring Meeting, 2022.

2. **Gertsenshteyn I**, Ahluwalia AS, Epel B, Kim H, Barth E, Tsai H-M, Leoni L, Lukens J, Hall K, Sundramoorthy SV, Zhang H, Giurcanu M, Fan X, Markiewicz E, Zamora M, Bhuiyan M, Kucharski A, Freifelder R, Roman B, Karczmar G, Kao C-M, Halpern H, Chen C-T: Validation of Multimodal Hypoxia imaging Using P_{O_2} EPR, FMISO PET, and DCE-MRI with H&E and CD31 Staining on SCC7 Squamous Cell Carcinomas. Radiological Society of North America (RSNA), 2021.

3. **Gertsenshteyn I**, Epel B, Kim H, Leoni L, Tsai H-M, Barth E, Lukens J, Hall K, Sundramoorthy S, Giurcanu M, Ahluwalia A, Fan X, Markiewicz E, Zamora M, Bhuiyan M, Freifelder R, Kucharski A, Kao C-M, Chen C-T, Halpern H: Validation and correction of ^{18}F-misonidazole PET with pO_2 EPR and DCE-MRI. International Society on Oxygen Transport to Tissue (ISOTT), Virtual, 2021.

4. **Gertsenshteyn I**, Epel B, Barth E, Kim H, Leoni L, Tsai H-M, Lukens J, Sundramoorthy S, Giurcanu M, Ahluwalia AS, Fan X, Markiewicz E, Zamora M, Bhuiyan

M, Friefelder R, Kucharski A, Kao C-M, Halpern H, Chen C-T: Optimal ^{18}F-misonidazole PET threshold to locate SCC7 tumor hypoxia using EPR pO_2 as ground truth. Society of Nuclear Medicine and Medical Imaging (SNMMI), Virtual, 2021. (First Place Winner at CMIIT Young Investigator Award Session.)

5. **Gertsenshteyn I**, Epel B, Giurcanu M, Leoni L, Barth E, Fan X, Markiewicz E, Zamora M, Tsai H-M, Friefelder R, Kucharski A, Bhuiyan M, Bodero D, Karczmar G, Kao C-M, Halpern H, Chen C-T: Improving ^{18}F-FMISO Hypoxia Target Map with EPRI and DCE-MRI. RSNA, 2019.

6. **Gertsenshteyn I**, Maggio MC, Krzykawska-Serda M, Barth E, Miller RC, Pelizzari CA, Sundramoorthy SV, Aydogan B, Weichselbaum RR, Tormyshev VM, Kim H-J, Kao C-M, Freifelder BE, Chen C-T, Halpern HJ: Two mammalian tumor models show improved clonogenic control with electron paramagnetic resonance (EPR) pO_2 image-based hypoxic boosts and with DCE-MRI corrected ^{18}F-Misonidazole PET. ASTRO, 2019, Halpern H.

7. **Gertsenshteyn I**, Epel B, Giurcanu M, Leoni L, Barth E, Fan X, Markiewicz E, Zamora M, Tsai H-M, Friefelder R, Kucharski A, Bhuiyan M, Bodero D, McVea A, Holderman N, Karrison T, Karczmar G, Kao C-M, Halpern H, Chen C-T: Preliminary Investigation of Hypoxia within Tumor Using EPRI, DCE-MRI, and PET-CT with ^{18}F-FMISO to Improve Radiotherapy. SNMMI, 2019.

Poster Presentations

1. **Gertsenshteyn I**, Epel B, Kim H, Fan X, Barth E, Zamora M, Markiewicz E, Hsiu-Ming Tsai H-M, Sundramoorthy S, Leoni L, Lukens J, Hall K, Florez-Martinez J, Bhuiyan M, Freifelder R, Kucharski A, Giurcanu M, Roman B, Karczmar G, Kao C-M, Chen C-T, Halpern H: Using EPR to calculate the optimal threshold to locate

hypoxia in ^{18}F-Fluoromisonidazole (FMISO) PET in three preclinical tumor types. Rocky Mountain Conference on Magnetic Resonance, 2022, Epel B.

2. Kotecha M, Epel B, Halpern H, **Gertsenshteyn I**, Rickard A,Palmer G, Mowery Y: A 25 mT Preclinical Electron Paramagnetic Resonance Oxygen Imager, JIVA-25TM, And Its Applications to Small Animal Image-Guided Radiotherapy. Small Animal Precision Image-Guided Radiotherapy, 2022, Kotecha M

3. **Gertsenshteyn I**, Epel B, Miller RC, Sundramoorthy S, Giurcanu M, Lukens J, Hall K, Tormyshev V, Aydogan B, Weichselbaum R, Kotecha M, Halpern H: Directing local hypoxia radiation boosts in three tumor models with EPR pO_2 imaging. ISOTT, Virtual, 2021, Howard H.

4. Smith HA, **Gertsenshteyn I**, Epel B, Barth E, Maggio MC, Sundramoorthy S, Halpern HJ: Predicting tumor control using geometric features of hypoxia measured with EPRI. AAPM, Virtual, 2020, Smith H.

5. Kim H, Epel B, Sundramoorthy S, Tsai H-M, Barth E, **Gertsenshteyn I**, Hua Y, Xie Q, Halpern HJ, Chen C-T, Kao K-M: Rejection of RF noise effects on PET in a PET/EPR combined imaging system. Institute of Electrical and Electronics Engineers (IEEE) Nuclear Science Symposium and Medical Imaging Conference, Virtual, 2020, Kim H.

6. Halpern H, Maggio M, Barth E, Bodero D, Miller RC, Pelizzari CA, Krzykawska-Serda M, Sundramoorthy SV, Aydogan B, Weichselbaum RR, Tormyshev VM, **Gertsenshteyn I**, Epel B: Increased tumor control boosting hypoxic regions identified with EPR pO_2 imaging in 2 tumor types. American Association for Cancer Research (AACR), Virtual, 2020, Halpern H.

7. **Gertsenshteyn I**, Epel B, Giurcanu M, Leoni L, Barth E, Fan X, Markiewicz E,

Zamora M, Tsai H-M, Friefelder R, Kucharski A, Bhuiyan M, Bodero D, Karczmar G, Kao C-M, Halpern H, Chen C-T: Multimodal imaging of tumor hypoxia with ^{18}F-misonidazole PET, EPR, and MRI. AACR, Virtual, 2020.

8. **Gertsenshteyn I**, Epel B, Giurcanu M, Maggio M, Krzykawska-Serda M, Barth E, Miller RC, Pelizzari CA, Sundramoorthy SV, Aydogan B, Weichselbaum RR, Tormyshev VM, Halpern H: EPR molecular oxygen images identify biologically relevant tumor hypoxia in two mammalian models to increase tumor control. World Molecular Imaging Congress (WMIC), 2019, Halpern H.

9. **Gertsenshteyn I**, Epel B, Giurcanu M, Leoni L, Barth E, Fan X, Markiewicz E, Zamora M, Tsai H-M, Friefelder R, Kucharski A, Bhuiyan M, Bodero D, Karczmar G, Kao C-M, Halpern H, Chen C-T: In-vivo preclinical imaging of tumor hypoxia using EPR, DCE-MRI, and PET-CT with ^{18}F-Miso to improve radiotherapy. WMIC, 2019, Halpern H.

10. **Gertsenshteyn I**, Foy J, Crofton A, Grekoski V, Tran T, Guruvadoo K, Al-Hallaq H, Armato SG III, Sensakovic W: Dependence of radiomics features on CT image acquisition and reconstruction parameters using a cadaveric human liver. AAPM, 2019, Foy J.